bias

Bremer Institut für
angewandte Strahltechnik

STRAHLTECHNIK

BAND 66

Vijay V. Parsi Sreenivas

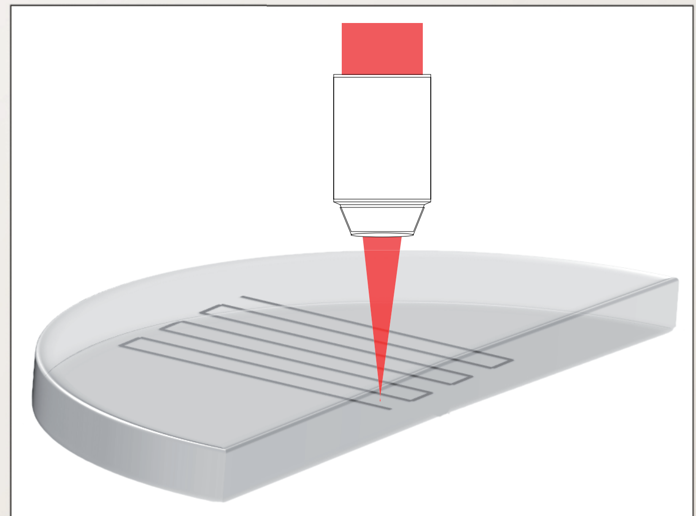

Material Modification due to Nonlinear Effects Created by Multiphoton Absorption in Single Crystalline Silicon

Wissen schafft Wirtschaft

Material Modification due to Nonlinear Effects Created by Multiphoton Absorption in Single Crystalline Silicon

vom Fachbereich für Physik und Elektrotechnik
der Universität Bremen

zur Erlangung des akademischen Grades eines
Doktors der Naturwissenschaften
(Dr. rer. nat.)

von
M.Sc. -Phys. Vijay Vittal Parsi Sreenivas
aus Bangalore, Indien

1. Gutachter:	Prof. Dr. Ralf B. Bergmann
2. Gutachter:	Prof. Dr. Walter Lang

Datum des Kolloquiums: 07.07.2017

Parsi Sreenivas, Vijay Vittal - Material Modification due to Nonlinear Effects Created by Multiphoton Absorption in Single Crystalline Silicon

Strahltechnik Band 66, BIAS Verlag, 2017.
Herausgeber der Reihe: F. Vollertsen, R. Bergmann

Dieses Werk ist urheberrechtlich geschützt.

Alle Rechte, auch die der Übersetzung, des Nachdrucks und der Vervielfältigung des Buches oder Teilen daraus, bleiben vorbehalten.

Kein Teil des Werks darf ohne schriftliche Genehmigung des Verlags in irgendeiner Form (Fotokopie, Mikrofilm oder andere Verfahren), auch nicht für Zwecke der Unterrichtsgestaltung – mit Ausnahme der in den §§ 53, 54 URG ausdrücklich genannten Sonderfällen – reproduziert oder unter Verwendung elektronischer Systeme verarbeitet, vervielfältigt oder verbreitet werden.

BIAS Verlag, Bremen, 2017

The work for this dissertation was done in the Micro and Nano Optics group at BIAS GmbH, in strong cooperation with the Department of Physics and Electrical Engineering at the University of Bremen.

Klagenfurter Straße 5
28359 Bremen

Bibliothekstraße 1
28359 Bremen

Eidesstattliche Erklärung

Hiermit erkläre ich an Eides statt,

- dass ich die vorgelegte Dissertation selbständig und ohne unzulässige fremde Hilfe angefertigt und verfasst habe, dass alle Hilfsmittel und sonstigen Hilfen angegeben und dass alle Stellen, die ich wörtlich oder dem Sinne nach aus anderen Veröffentlichungen entnommen habe, kenntlich gemacht worden sind;

- dass die Dissertation in der vorgelegten oder einer ähnlichen Fassung noch nicht zu einem früheren Zeitpunkt an der Universität Bremen oder einer anderen in- oder ausländischen Hochschule als Dissertation eingereicht worden ist.

09.05.2017 Vijay Vittal Parsi Sreenivas

Abstract

Material modification inside its bulk via high powered lasers involves much more than just heat transfer and melting of materials. It entails with it complex nonlinear physical phenomena such as multiphoton absorption, self-phase modulation, and self-focussing, amongst many others. These phenomena occur only with ultrafast lasers at very high intensities. Realising subsurface or bulk modifications in semiconductors such as silicon, opens up new avenues in the fields of optoelectronics and optical computation with the potential of increasing current computational speeds by orders of magnitude. The technology of three dimensional volume modification in materials via ultrafast lasers and nonlinear physics, is however, still in its nascent stages. This work explores the possibility of realising bulk modification in silicon and other polymers, and as well as their integration with optoelectronic devices; thus paving way for the future of optical computation.

Zusammenfassung

Die Materialmodifikation im Volumen mit Hochleistungslasern beinhaltet mehr physikalische Effekte als nur den Wärmetransport oder ein Aufschmelzen des Materials. Komplexe Phänomene der nichtlinearen Physik, wie die Multiphotonenabsorption, Selbstphasenmodulation und Selbstfokussierung müssen berücksichtigt werden. Diese Effekte treten nur bei ultrakurzen Laserpulsen unter sehr hohen Intensitäten auf. Die laserinduzierte Materialmodifikation von Halbleiterkristallen wie Silizium im Volumen oder dicht unter der Oberfläche eröffnet neue Wege im Bereich der Optoelektronik und der optischen Datenverarbeitung um in Zukunft die Verarbeitungsgeschwindigkeiten um mehrere Größenordnungen zu verbessern. Die Technologie der dreidimensionalen Materialmodifikation durch Ultrakurzpulslaser und dem Ausnutzen von nichtlinearen Effekten steckt jedoch noch in der Entwicklung. Diese Arbeit untersucht die Möglichkeiten zur laserinduzierten dreidimensionalen Materialmodifikation in Silizium und Polymeren, sowie die Integration in optoelektronische Bauteile. Damit leistet diese Arbeit einen Beitrag zur Zukunft der optischen Datenverarbeitung.

Acknowledgement

Firstly, I would like to express my sincere gratitude to my advisor Prof. Dr. Ralf B. Bergmann for giving me the opportunity to start my professional scientific career and for the continuous support for my Ph.D. research. His patience, motivation, and knowledge in the field of silicon has continuously motivated me throughout the course of my work. My sincerest thanks to Prof. Dr. Walter Lang for agreeing to be the second supervisor to my doctoral thesis and overseeing my work. I would like to also extend my thanks to the groups of Prof. Walter Lang, Prof. Garcia-Ortiz, and Prof. Gutowski for the fruitful collaboration during the project - Saphir. My work wouldn't have been quite complete without the continuous guidance of my group leader Mike Bülters and the long yet rigorous discussions with my colleague Martin Schröder. My thanks also extends to Ms. Eva Maria-Meyer who tirelessly and joyfully helped me characterise my samples in the SEM. I would also like to thank Dr. Gerrit Dumstorff for wonderful discussions and brainstorming sessions. I would like to also take this opportunity to thank my other colleagues (in no particular order): Christian Kapitza, Reiner Klattenhoff, Dr. Claas Falldorf, Dr. Colin Dankwart, Lars Rosenboom, Dr. Edwin Kamau, Dr. Mostafa Agour, Heike Weers, Prof. Thomas Kreis, Marc Sandner, and Alexander Hildebrand - who were instrumental in making my stay at BIAS memorable and also in improving my German language skills!

During the course of this work, I had the excellent opportunity of working with various industry and research partners. My sincerest thanks to them all - especially, Dr. Holger Fischer from Nanoscribe GmbH and Dr. Thomas Walter from Soliton GmbH. I have also had the pleasure of working with a handful of students and guiding them during their Bachelor's and Master's theses, whom I would like to thank for the great company and of course for helping me with my routine work schedule. Many thanks to all the students (in no particular order): Heiner Gerdes, Nanda Therakanambi, Martial Nana, Michael Brink, Katharina Morosov, Andreas Braun, and Aditya Chauhan.

I am eternally thankful and grateful to my parents and sister who have had faith in me and have supported me all my life. Finally, I would like to thank my lovely wife, Dr. Gayatri Rane - who has stood by me and motivated me through ebb and flow.

Contents

1 Introduction **1**
1.1 Lasers 1
1.1.1 Working principle of lasers 2
1.1.2 Properties of lasers 4
1.1.3 Types of lasers 6
1.2 State of the art laser material modification techniques 10
1.2.1 Multiphoton absorption 10
1.2.2 State of the art laser microstructuring 13
1.3 Motivation 18
1.4 Objective and outline 19

2 Laser Irradiation and Material Interaction **21**
2.1 Introduction 21
2.2 Material properties of silicon 22
2.2.1 Crystal structure 23
2.2.2 Band structure 25
2.3 Material properties of polycarbonate 27
2.4 Material properties of SU-8 28
2.4.1 Processing guidelines for SU-8 29
2.4.2 Positive and negative photoresists 30
2.5 Laser material interaction 31
2.5.1 Maxwell's equations 32
2.5.2 Ultrafast laser material interaction 35
2.5.3 Interaction of fs laser radiation with silicon 36
2.6 Summary 40

3 Experimental Set-Up, Design, and Analytic Tools **41**
3.1 Introduction 41
3.2 Comparison of laser systems 42
3.3 Laser enabled Nano-structuring Apparatus 42
3.3.1 Optics and objectives 43
3.3.2 Motion stages and controller 43
3.3.3 User controls 46

3.4 Photonic Professional . . . 46
3.4.1 Sample preparation . . . 46
3.4.2 Photoresists . . . 48
3.5 Modular Optic Nano Analyser . . . 49
3.5.1 Mechanical and electro-optical components . . . 49
3.6 Scanning Electron Microscope and Focussed Ion Beam . . . 52
3.7 Optical and infrared microscopes . . . 54
3.8 Summary . . . 55

4 Subsurface Modification in Silicon and SU-8 **57**
4.1 Material modification in silicon . . . 57
4.1.1 Infrared imaging of subsurface modifications . . . 57
4.1.2 Diffraction tests with infrared laser source . . . 60
4.1.3 Effect of pulse energy variation . . . 63
4.1.4 SEM and FIB analysis . . . 64
4.1.5 Defect etching with Potassium Hydroxide . . . 67
4.1.6 Simulation results of waveguides in silicon . . . 69
4.2 Material modification in SU-8 (IP-L) . . . 75
4.2.1 3D Polymer Optical Waveguides . . . 75
4.2.2 Results and discussion . . . 77
4.3 Summary . . . 85

5 Applications of 3D Microstructuring **87**
5.1 Optical Vector Matrix Multiplier . . . 87
5.1.1 Electronic components of Optical Vector Matrix Multiplier . . . 89
5.1.2 Waveguide optimisation for OVMM . . . 91
5.1.3 OVMM operation and prototype . . . 95
5.2 3D Computer Generated Volume Holograms - CGVH . . . 96
5.3 Summary . . . 97

6 Conclusion and Future Work **99**
6.1 Conclusion . . . 99
6.1.1 Nonlinear absorption of laser irradiation & process parameters . 99
6.1.2 Experimental set-up . . . 100
6.1.3 Subsurface modification in silicon and polycarbonates . . . 100
6.1.4 3D polymer lithography for photonic applications . . . 101
6.1.5 Optical Vector Matrix Multiplier . . . 101
6.2 Future work - Optical Circuit Board . . . 102

Appendices **105**

A Technical specifications of LeNA **107**

A.1 Laser system . . . 107
A.2 User controls . . . 110
A.3 User interface: Raydiance M50 . . . 111
A.3.1 Status panel . . . 111
A.3.2 Control and measurement panel . . . 111
A.3.3 Pump and beam control . . . 113
A.3.4 Packet mode and trigger . . . 113
A.4 Fringe Processor . . . 113
A.4.1 Re-init & Home . . . 114
A.4.2 Load sample . . . 116
A.4.3 On screen joystick . . . 116
A.4.4 Position . . . 116
A.4.5 Saved position . . . 116
A.4.6 Velocity . . . 116
A.4.7 Acceleration . . . 116
A.4.8 Generate . . . 117
A.4.9 Set zero & load . . . 117
A.4.10 Start . . . 117

B .yal File Format **119**
B.1 Syntax . . . 119
B.2 Minimum Working Examples . . . 122
B.2.1 A simple .yal Script . . . 122
B.2.2 A .yal script calling other .yal scripts . . . 123

C Technical Specifications of OVMM Components **125**
C.1 LED . . . 125
C.2 Photodiode . . . 126
C.3 Arduino microcontroller . . . 126

Bibliography **129**

List of Figures **137**

List of Tables **139**

Glossary of Terms **141**

Curriculum Vitae **143**

1 Introduction

The beginning in every task is the chief thing.

— Plato

This chapter provides an introduction to lasers, materials, and their interactions with each other. Various kinds of laser systems that are commercially available are discussed along with their ability to interact with the materials of interest, especially single crystalline silicon. Based on thorough literature review and a discussion on state of the art technologies, a foundation for this research work is established.

1.1 Lasers

A laser (an acronym for **L**ight **A**mplification by **S**timulated **E**mission of **R**adiation) is a device that produces and amplifies an intense beam of highly coherent, highly directional light. In 1917, Albert Einstein laid down the theoretical foundations of the principles of laser through his seminal paper “Zur Quantentheorie der Strahlung” [1]. He proposed the concept of ‘stimulated emission’, where a photon interacts with an excited molecule or atom and causes the emission of a second photon having the same frequency, phase, polarisation and direction. By using mirrors to send the light emitted right back into atoms, Einstein suggested, a chain reaction could be triggered releasing an avalanche of same-wavelength light. He introduced the probability coefficients for absorption, spontaneous and stimulated emission of electromagnetic radiation, which are now known as Einstein coefficients. Several years and failed attempts later, Theodore H. Maiman demonstrated at Hughes Research Lab in 1960 [2] the operation of the first device for Light Amplification by Stimulated Emission of Radiation in the visible wavelength region. Since then, numerous patents involving the laser have been granted and lasers have been ubiquitous finding utility in varied applications from industry and medicine, to several areas of science and technology that are routinely used in everyday consumer products. Laser devices, as of 2016, range in sizes from as small as a few μm [3] (semiconductor lasers) to as a large as tens of metres [4] (petawatt lasers).

1.1.1 Working principle of lasers

A laser consists of three main components:

1. A gain medium, to amplify light by means of stimulated emission
2. A pump source, to create a population inversion in the gain medium
3. An optical cavity, to trap the light created by the pump source

The laser beam is the tiny portion of the light that is intentionally allowed to escape from the optical cavity that has a fixed oscillation wavelength. The wavelength of emitted laser beam is controlled by varying the parameters of these three main components. Figure 1.1 shows a schematic of a laser oscillator. The gain medium can be a solid, liquid, or gas. Depending on the gain medium, a laser is classified as a semiconductor laser, gas laser, dye laser, etc. The pump source can be an electric spark, a lamp, or even another laser. The pump source is required to activate the gain medium and cause a population inversion, leading to a stimulated emission. This is shown in figure 1.2c. The emitted photons from this process are repeatedly reflected back and forth between two reflecting surfaces (mirrors). Depending on the length of the optical cavity, one or several characteristic modes of the emitted photons get repeatedly amplified and form the laser beam.

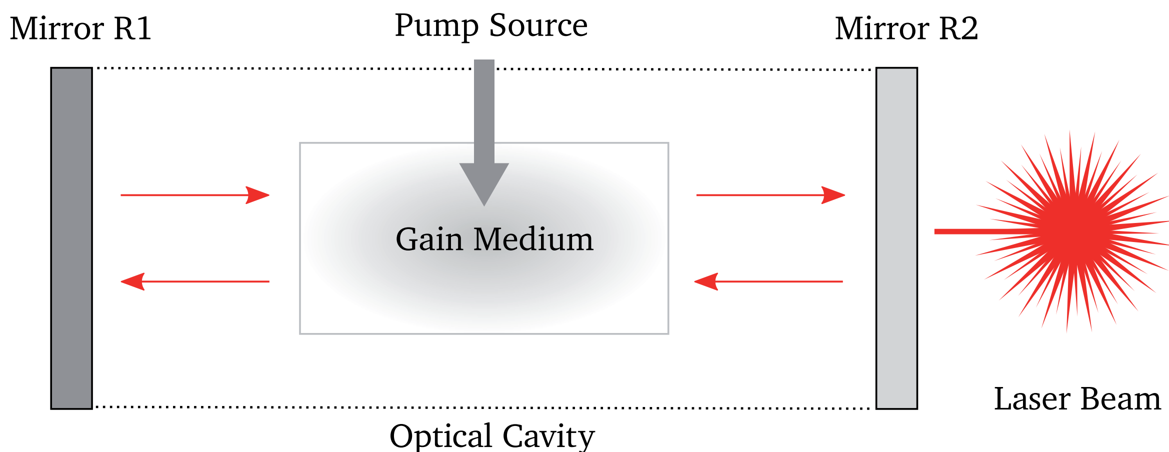

Figure 1.1: Schematic of a laser oscillator. Mirror R1 is fully reflective and R2 is partially reflective. This allows the laser beam to escape the cavity. The pump source activates the gain medium. The red lines indicate the laser beam oscillating in the optical cavity.

When an electromagnetic wave interacts with matter, absorption occurs followed by the process of either spontaneous or stimulated emission. Absorption of a photon will occur only when the energy of the photon exactly matches the energy gap between the initial and final states of the system (see figure 1.2a). In this interaction, if there is no pair of energy states such that the energy of the photon can excite the system from the lower to

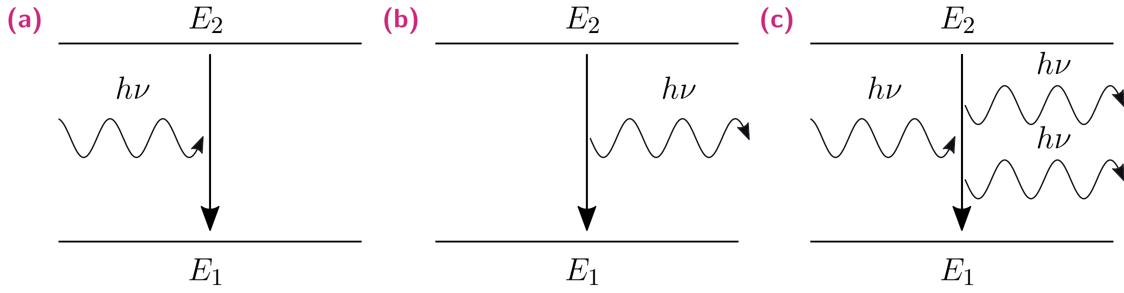

Figure 1.2: (a) Absorption, (b) spontaneous and (c) stimulated emission of electromagnetic waves in a two-level system with E_1 as the ground state and E_2 as the excited state.

the upper state, then the system is said to be transparent to that photon. The change in the number density of atoms in state E_1 per unit time due to absorption is

$$\frac{\partial z_{abs}}{\partial t} = -n_1 \rho(\nu) B_{12} \tag{1.1}$$

where $\rho(\nu)$ denotes the spectral energy density of the isotropic radiation field at the frequency of the transition, n_1 denotes the number density of atoms in energy level 1 and B_{12} is the Einstein coefficient which gives the probability per unit time per unit spectral energy density of the radiation field that an electron in state 1 with energy E_1 will absorb a photon with an energy $(E_2 - E_1) = h\nu$ and jump to state 2 with energy E_2. Its SI unit is $m^3 J^{-1} s^{-2}$.

In the case of spontaneous emission, if the atom is initially in the ground state E_1 and raised to an excited state E_2, it spontaneously tends to decay into the stable ground state. The difference in energy between the states ΔE is released in the form of an electromagnetic wave. This process is referred to as spontaneous or radiative emission (see figure 1.2b). The frequency of the emitted radiation is given by the equation, $\nu = E_2 - E_1/h$. Where h is the Planck's constant. Therefore, a photon with an energy $h\nu$ is emitted during each spontaneous emission process. Spontaneous emission can also occur in isolated systems with no external perturbation and it can be shown that the rate of emission of photons from a higher to lower (stable) energy level is proportional to the number of atoms per unit volume (n_2) in E_2 and is expressed as

$$\frac{\partial z_{spon}}{\partial t} = -n_2 A_{21} \tag{1.2}$$

where A_{21} is the Einstein coefficient denoting the spontaneous emission lifetime and its SI unit being s^{-1}. The photon characteristics of the emission is random and hence the

light emitted is said to be incoherent. Due to the energy-time uncertainty principle, the transition actually produces photons within a narrow range of frequencies called the spectral line width.

If an electromagnetic radiation of frequency ν is incident onto the system while in its excited state E_2, the interaction of radiation with the system stimulate the decay to level E_1. In this case, a photon with the same frequency ν of the incoming radiation and with the same propagation direction, polarisation, and phase is emitted - unlike the case of spontaneous emission. This is a major distinction and a fundamental reason why a laser emits coherent light. The stimulated emission process can be best described by the equation

$$\frac{\partial z_{stim}}{\partial t} = n_2 \rho(\nu) B_{21} \tag{1.3}$$

where the Einstein coefficient B_{21} is the rate of stimulated emission and is proportional to the incident radiation flux and its SI unit is $m^3 J^{-1} s^{-2}$.

In the simplest case, a laser transition occurs as a result of stimulated emission, and involves only two energy levels of the active atoms or ions of the gain medium: an upper and a lower laser level. When the population of the upper laser level is higher than that of the lower level (i.e. more laser-active atoms or ions are in the higher level), in other words, more laser-active ions are in the upper state than in the lower state, the laser medium is in a state called population inversion. Population inversion is a state of the system which deviates from thermal equilibrium; in thermal equilibrium, the population of the lower level is always higher, and a positive net gain can never occur. Inversion can be achieved by optical pumping and it must maintain the necessary population inversion to keep the laser process stable.

1.1.2 Properties of lasers

Lasers show an extremely high degree of monochromaticity, coherence, and directionality. Since the radiation is oscillating in resonance with the optical cavity, monochromaticity is integral to laser radiation. Any deviation from the central frequency of the radiation arises from the quantum noise. In some laser systems with frequency stabilisation, a line width of a few Hz can be achieved.

The coherence of a laser radiation refers to either *temporal* or *spatial* coherence. To define spatial coherence, let us consider two points P_1 and P_2 that, at a time $t = 0$, belong to

the same wavefront. If the difference between their phases also remains zero at times $t > 0$, we say that there is perfect spatial coherence between the two points P_1 and P_2. In practice, for any point P_1, in order to have some degree of phase correlation, point P_2 must lie within some finite area around P_1, which is called the coherence area. The high degree of spatial coherence of laser radiation stems again from the fact that the spatial field distribution of the beam generated by stimulated emission is a mode of the optical resonator.

To define temporal coherence at a given point P, let us consider the phase difference for the electric field at P at times $t + \delta t$ and t. For a given delay δt, if the phase difference is independent of time t, we say that there is temporal coherence over a time δt. If this occurs for any value of δt, the EM wave is said to have perfect temporal coherence. If, conversely, this occurs only for delays δt smaller than a given delay δ_o, the wave is said to have partial temporal coherence, and δ_o is called the coherence time of the electromagnetic wave at point P. The concept of temporal coherence is closely related to that of monochromaticity; in fact, for a continuous wave laser one can show that the coherence time δ_o is related to the laser line width $\Delta\nu_L$ by the simple relation $\delta_o \approx 1/\Delta\nu_L$. The high degree of temporal coherence of laser radiation is therefore due to its extreme degree of monochromaticity.

The directionality of the laser beam is due to the fact that the gain medium is placed inside an open optical resonator and, as a consequence, stimulated emission preferentially occurs in the direction orthogonal to the two cavity mirrors (figure 1.1), where feedback from the mirrors is most effective and diffraction losses are the smallest. The laser beam emitted from the output coupler shows a divergence angle which, in the ideal case, is limited by diffraction. From diffraction theory, the divergence angle [5] for a monochromatic beam of wavelength λ is given by

$$\theta_d = M^2 \left(\frac{\lambda}{\pi w_o} \right) \tag{1.4}$$

where M^2 is a numerical coefficient (also called the beam quality factor) whose specific value depends on the particular transverse field distribution and w_o is the beam radius at the beam waist. The M^2 factor can be calculated from the measured evolution of the beam radius along the propagation direction. For non circularly symmetric beams, this factor can be different for two directions orthogonal to the beam axis and to each other. The beam quality factor limits the degree to which the beam can be focussed for a given beam divergence angle. A diffraction-limited beam has an M^2 factor of 1, and is a Gaussian beam. This theoretical limit represents an ideal laser beam in the traverse electro-magnetic mode, TEM_{00}. A laser beam with an M^2 value x is said to be x times diffraction limited.

1.1.3 Types of lasers

Lasers can be broadly classified by their operating principle into continuous and mode-locked lasers. They can also be classified based on the gain media or the lasing material; Ex. Helium Neon, Ruby, Dyes, Nd:YAG. The next few subsections will briefly gloss over these variations.

Continuous wave and mode-locked

A laser can be classified as operating in either continuous or pulsed mode, depending on whether the power output is essentially continuous over time or whether its output takes the form of pulses. A laser emitted from a cavity can have either of these two modes. The first continuous wave laser was a helium–neon laser operating at 1153 nm [6]. The commonly used He-Ne emission wavelength of 632.8 nm was developed later. Other lasers which can also be operated continuously are: gas lasers, many types of solid-state lasers (including semiconductor lasers), and dye lasers. The output power of a continuous wave laser is more or less constant on longer time scales.

In pulsed lasers the optical power appears in pulses of a certain duration and repetition rate. This encompasses a wide range of technologies addressing a number of different motivations. Some lasers are pulsed simply because they cannot be run in continuous mode. The most commonly used methods in pulsed lasers are

1. Pulsed Pumping (for pulses in the μs range)
2. Q-Switching (for pulses in the ns range)
3. Mode Locking (for pulses in the ps-fs range)

Pulsing can be achieved by using a pulsed source to pump the gain media. The pulsed source can either be electronically controlled, or optically controlled, or via another laser that is already pulsed. Pulsed pumping is also required for three-level lasers in which the lower energy level rapidly becomes highly populated preventing further lasing until those atoms relax to the ground state.

In a Q-switched laser, the population inversion is allowed to build up by introducing loss inside the resonator which exceeds the gain of the medium; this can also be described as a reduction of the quality factor or 'Q' of the cavity. When the pump energy stored in the laser medium approaches the maximum possible level, the introduced loss mechanism (often an electro- or acousto-optical element) is quickly removed, allowing lasing to begin

which rapidly obtains the stored energy in the gain medium. This results in a short pulse incorporating that energy, and thus a high peak power.

A laser oscillates in a large number of spectral modes. When the modes are *forced* to oscillate together with the same phase, the laser is said to be mode-locked. Mode-locking can be broadly classified into active and passive mode locking techniques. In active mode-locking, an electro-optical or an acousto-optical crystal is placed inside the laser cavity and driven into resonance by a piezoelectric crystal. The standing acoustic waves that are created induces a periodic refractive index variation in the crystal. This allows the crystal to act as a diffraction grating that is electronically controlled. When the laser light is reflected back and forth in the cavity, fixed phases or laser modes are reflected back by this electronically controlled crystal and a single central laser frequency is outputted. In passive mode-locking, a saturable absorber is placed in the laser cavity that selectively absorbs the unwanted laser modes. The saturable absorbers are generally intensity dependent. They absorb the lower intensity side modes of the laser oscillations and transmit the higher intensity modes which leads to a selective amplification of a single laser mode. For this purpose, they are expected to have a very small relaxation time.

It is also, however, possible to intentionally turn a continuous laser on and off at a desired rate to create a pulsed laser. When this modulation rate is on time scales much slower than the cavity lifetime and the time period over which energy can be stored in the lasing medium or pumping mechanism, then it is still classified as a modulated laser.

Gain media classification

Laser systems are also classified based on the material used as their gain medium. Some of the commonly available types are lasers are:

1. Solid state lasers
2. Semiconductor lasers
3. Dye lasers
4. Gas lasers

The first laser in the visible range was demonstrated in 1960. It was a solid state laser with Ruby as the active material. Ruby is crystalline aluminium oxide (Al_2O_3) doped with Chromium (Cr). The triply ionised Cr ions replace some of the Al^{3+} ions, that make the otherwise transparent crystal, a pink/red crystal. In the original design by Maiman, a Ruby cylinder $4\,cm$ in length and $0.5\,cm$ in diameter was used. Both ends were polished

and silvered. One of the ends had a transmission of 10%. A xenon flash lamp was helically wrapped around this cylinder, which provided flashes of white light in the ms range. The chromium ions in ruby strongly absorb light in the blue ($420\,nm$) and green ($545\,nm$) wavelength regions. They then quickly and non-radiatively decay into a metastable state with a lifetime of $5\,ms$ creating a population inversion suitable for lasing. The final output wavelength of the laser is a deep-red $694.3\,nm$.

Neodymium lasers are a class of four-level laser systems using rare-earth ions: neodymium, erbium, etc. in various crystals. Many of these lasers work in the far infrared range ($> 1\mu m$). The lasers used during the course of this work, belong to this class of rare earth ions lasers. The neodymium ion (Nd^{3+}) is incorporated in the $Y_3Al_5O_{12}$ lattice, also commonly known as the YAG - Yttrium Aluminium Garnet. The resulting Nd:YAG system is one of the most versatile systems of currently used solid state lasers.

Erbium doped fibre lasers is a sub-category of a larger erbium-doped glass based gain media lasers. Erbium is used in its trivalent Er^{3+} form as a dopant in host materials such as crystals and glass. The transition between the energy levels $^4I_{13/2}$ and $^4I_{15/2}$ is the most commonly transition that is used to generate an output wavelength of $1.55\,\mu m$. As this wavelength lies in the C-band of telecommunications bandwidths, it is one of the most widely used commercial wavelengths. The most common pump scheme is based on the transition $^4I_{15/2} \rightarrow {}^4I_{11/2}$ with a wavelength around $0.9 - 1\,\mu m$, as shown in figure 1.3.

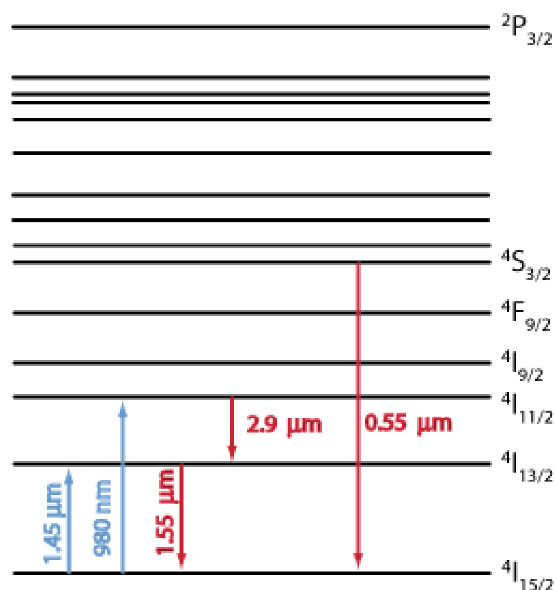

Figure 1.3: Energy level structure of the trivalent erbium ion, and some common optical transitions. Source [7]

Semiconductor lasers were first predicted in 1961 by Bernhard et. al. [8]. It was theorised that stimulated emission of photons may be obtained in semiconductor materials from

transmission between conduction and valence bands. The working principle is similar to other laser systems. A pumping mechanism pumps the electrons from valence band into a higher energy level in the conduction band. The electrons then rapidly and non radiatively fall to a conduction band minima and create a population inversion. At the same time, holes are generated in the valence band that move to a local maxima. The recombination process is followed by a release of photon which is governed by the band energy gap. Most semiconductor lasers are laser diodes that are created by p-n junction and electrically pumped.

Dye lasers and gas lasers, use liquids and gases as gain media, respectively. They use optical excitation as well as electric discharge as pump sources. Although they are commercially available, they are seldom used in consumer products due to the use of liquid and gas as their gain media. However, they do present certain advantages over semiconductor and solid state lasers. The material in the gain media for gas lasers is relatively inexpensive and almost impossible to be damaged. A comparison between different laser systems is shown in table 1.1.

Table 1.1: Comparison of a few different types of lasers based on their gain media

Gain Media	Pump Source	Typical Wavelength (nm)
Ruby	Flash lamp	694.3
Nd:YAG	Flash lamp, diode	1064
Ti:Sapphire	Solid state Laser	650 - 1100
Er:YAG	Flash lamp, laser	2940
GaN	Electrical current	400

Femtosecond lasers

Femtosecond ($1\,fs = 10^{-15}\,s$) laser is a pulsed laser that generate extremely high intensity pulses with each pulse having a temporal duration that typically ranges between $1-1000\,fs$ and was developed in the late 80's. Also known as ultrashort pulses, they have a broadband optical spectrum, and can be created by mode-locked oscillators. They are commonly referred to as ultrafast events. Amplification of ultrashort pulses require the technique of chirped pulse amplification. They are characterised by a high peak intensity that usually leads to nonlinear interactions in various materials, including air. These processes are studied in the field of nonlinear optics.

Femtosecond lasers are a clear technological breakthrough with exciting potential for many applications and have brought about impressive progress in the study of light and matter interaction. Ever since the pioneering reports on femtosecond laser microstructuring in

the mid 90's, revolutions in laser technology together with photonic material design have enabled the observation of numerous kinds of new physical and chemical phenomena [9–11]. It has also helped in creating induced nano and microstructures, and hence, made possible to control and manipulate light in unusual and interesting ways [12, 13]. The extreme high peak intensities in the focus of femtosecond laser pulses have offered the possibility for a variety of new applications ranging from precise scalpels for delicate life science to driving sources for table-top particle accelerators. One of the most promising applications of femtosecond lasers is microstructuring in transparent materials, such as glasses, crystals, and polymers [14, 15].

1.2 State of the art laser material modification techniques

Research into new types of lasers and laser phenomena is a highly active area in physics laboratories for applications such as holography, interferometry, distance measurement, data storage etc. One of the important applications of lasers are in areas where high-intensity electromagnetic fields are required. For instance, the ability to accurately deliver large amounts of energy into confined regions of a material in order to achieve a desired response has been used for the realization of material modification and two-photon absorption [16, 17]. This work is focused on the application of lasers using the principle of multiphoton absorption for material processing.

1.2.1 Multiphoton absorption

In 1931, Maria Göppert-Mayer first postulated the existence of two or more photon absorption and established it theoretically in her doctoral dissertation [18] titled "Über Elementarakte mit zwei Quantensprüngen". The derivation was based on the work of Kramer and Heisenberg's study of two-photon emission which uses Dirac's dispersion theory of calculation. In simple terms, e.g. two photon absorption is a process in which two photon are absorbed by a sample simultaneously (or within less than a nanosecond), exciting e.g. an atom or ion to a higher energy [19, 20]. Neither photon is at resonance with the available energy states of the system, however, the combined frequency of the photons is at resonance with an energy state. An electron absorbs two photons and achieves an excited state that corresponds to the sum of the energy of the incident photons, as shown in figure 1.4. When absorbing multiple photons simultaneously, an atom will proceed to an intermediate state corresponding to a characteristic eigenstate or to a virtual state. These virtual states are not eigenstates; they correspond to no specific n or l

state (Principal or Azimuthal quantum numbers). Instead, they are merely superposition of waves. No population of electrons transitions to the virtual state. The lifetime of a virtual state is short, relative to eigenstates. The closer the virtual state is to an actual eigenstate, the longer the lifetime of the virtual state. Through two-photon absorption, the high energy levels can be populated, which are otherwise unreachable by single photon transitions from the ground state. Once the electrons have absorbed two photons and are at a high energy level, it takes no more than the absorption of another photon to release the electron and ionize the atom. If there is an intense, monochromatic photon source (such as a high energy laser) used to excite these atoms through multiphoton absorption, ample photons would be present to continue the excitation process and ionize the atom before it radiates back to a lower energy level. Thus atoms can absorb two or more photons simultaneously, allowing an electron to transition to states unreachable by single photon absorption. An atom absorbing multiple photons simultaneously might be ionized by photons with energies less than the threshold energy. Since any observable effect of this phenomenon could not be possible without a very intense beam of radiation, her prediction could not be investigated in detail until the construction of the first laser in 1960. The typical non-resonant cross section for two-photon absorption [21] is exceedingly small ($\sim 10^{-35} m^4/W$) and therefore, the experimental confirmation of such a process had to await the advent of laser sources with sufficient intensity to observe processes with such small cross sections.

Two-photon absorption (TPA) is a third-order process several orders of magnitude weaker than linear absorption at low light intensities. It differs from linear absorption in that the atomic transition rate due to TPA depends on the square of the light intensity, thus it is a nonlinear optical process, and can dominate over linear absorption at high intensities.

The invention of laser had a great impact on this field because of the necessity of a high intensity electromagnetic field to induce transitions. Multiphoton absorption increases with the square of the light intensity and hence require intense laser beams, focused pulsed lasers that generate a very high instantaneous photon density. Immediately after the invention of the laser, W. Kaiser and C. G. B. Garret in 1961 reported [22] the first experimental verification of the two-photon absorption of a compound. They used the new laser technology to excite the Europium-doped crystal CaF_2:Eu^2+ with both red and blue light to induce a two photon transition. The invention of two-photon fluorescence microscopy by Webb et. al. [23], and the rapid adoption of this technique by manufacturers of confocal microscopes, has led to an explosion of interest in all types of multiphoton processes, opening a new area of light and matter interactions. The origin of three dimensional processing by means of two-photon absorption can be attributed to the proposal of 3D data storage by Parthenopoulos and Rentzepis in 1989 [24]. Bit data were recorded and erased in a photo-chromic dye-embedded polymer matrix through photo chromic reactions, and were read through the excitation of fluorescence from the

dye. They induced two-photon absorption by a tightly focused laser spot both for the writing and reading processes in order to stack the bit data in 3D. Two-photon absorption allows for unprecedented depth in medical imaging technology. Traditional single photon methods result in an enormous amount of scattering from the biological tissue samples. However, these nonlinear optics allow for the assignment of the scattered photons to their origins. Much of the research in this area is focused on maximising the depth and clarity of the signal for this potentially non-intrusive medical procedure [25, 26]. Several parameters have been looked at including excitation wavelength, beam size, pulse width, and pulse frequency. Other applications of multiphoton absorption include 3D micro-fabrication, optical logic, pulse reshaping and optical power limiting.

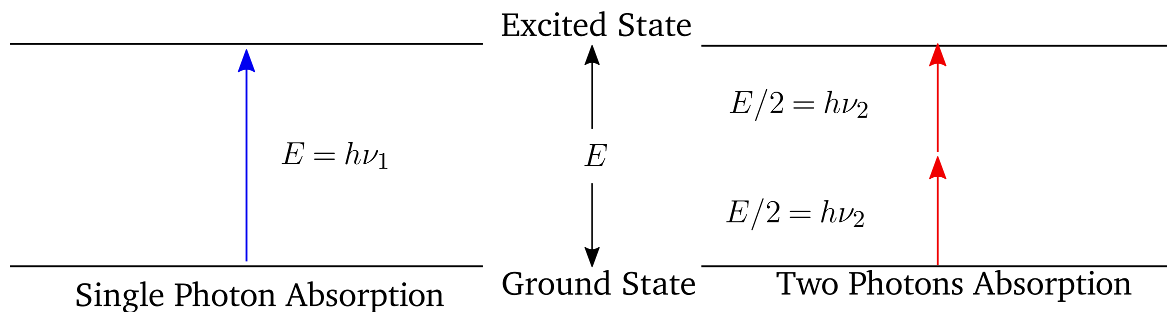

Figure 1.4: Single and two photon absorption. The photon energy must match the energy required to excite the molecule from its ground state. In the case of TPA, this is fulfilled by two photons with exactly half the energy to excite the molecule.

Thus the fields of two-photon absorption and nonlinear light and matter interactions in materials have since then been exploited to study and characterise various elements and molecules [27, 28]. Since the two-photon process is non-linear in nature, high electromagnetic light densities are required to initiate it. The invention of laser made it possible to efficiently collimate and focus coherent light into confined regions of space, opening a new area of light and matter interactions. In this work, we investigate the light and matter interactions for microstructuring.

The Beer–Lambert's law for the one photon or linear absorption is

$$I(z) = I_0 e^{-\alpha z} \tag{1.5}$$

where, the instantaneous intensity of light I is represented as a function of the initial intensity I_0, and path length z. α is the coefficient of linear absorption which is specific for a given material. In the case of two photon absorption, this law takes the form [29]

$$I(z) = \frac{I_0}{1 + \beta z I_0} \tag{1.6}$$

where, β is the coefficient of two photon absorption. The general expression for the electromagnetic flux and the coefficients of absorption for linear and nonlinear processes is shown in equation 2.26 and for silicon specifically in equation 2.28. These equations form the basis of laser matter interaction in silicon.

1.2.2 State of the art laser microstructuring

Femtosecond laser microstructuring is a rapidly advancing area of ultrashort laser applications. It utilises the properties of ultrashort laser pulses to achieve an unprecedented degree of control in sculpting the desired microstructures internal to the materials without collateral damage to the surroundings [30–34]. Using femtosecond rather than picosecond or nanosecond light pulses, laser energy is deposited into small volumes by multiphoton nonlinear optical absorption followed by avalanche ionisation. Because typical heat diffusion time is in the order of nanosecond to microsecond time scale whereas the electron-phonon coupling time of most materials are in the picosecond to nanosecond. Therefore, when laser energy is deposited at a time scale much shorter than both the heat transport and the electron-phonon coupling, the light and matter interaction process is essentially frozen in time. The affected zone is altered from solid to vapour phase and to plasma formation almost instantaneously. Unlike conventional laser machining, femtosecond laser machining reduces material damages to the surroundings. Because the machining process is not dependent on the linear absorption at the laser wavelength, virtually any dielectric, metals, and mechanically hard materials can be machined by the same laser beam [35–40].

Subsurface modification of dielectric materials is of great importance for optical applications such as the production of waveguides, gratings, lenses and three-dimensional data storage [41–43]. Furthermore, the technique is of growing interest for engineering subsurface modifications in semiconductors. Of particular interest for the semiconductor industry is the process of subsurface laser-dicing that enables the accurate sectioning of wafers and devices. Subsurface laser-dicing involves inducing closely spaced subsurface modifications that act to guide subsequent crack propagation in a highly controlled manner during cleaving.

By careful control of the laser intensity, one can produce permanent refractive index modification on the work piece. Direct writing of optical waveguides in three-dimension becomes possible. More importantly, passive and active optical devices can potentially be fabricated directly in three-dimension using one laser system in one processing step [44–47].

Because of the nature of the nonlinear optical fabrication process, features size smaller than the diffraction limit can be created internal to the substrate at various depths. Three dimensional sub-micron sized structures can be defined to produce miniature photonic components, read only memory chips, and hollow channel waveguides that may be of interest in the area of optical communication network, optical data memory, and biological optical chips [48–52].

Laser Wafer Dicing

Due to its excellent electronic properties, Silicon dominates the semiconductor industry today. Silicon is the corner stone of the photovoltaics industry where continuous efforts are being made to improve the solar cell efficiencies and increase the throughput but at the same time keeping the production costs down. Silicon also forms the basis of almost all electronic devices currently in use. It is used as the substrate for integrated circuits that are cut out of large wafers, $20 - 30\,cm$ in diameter. These wafers are sliced out of silicon ingots that are between $1 - 1.5\,m$ in length. Presently the most common technique used to slice a wafer off the ingot is the Diamond Inner Diameter saw blade method, wherein a circular steel blade is equipped with a diamond cutting edge at its inner diameter and its outer diameter is mounted on an air bearing and rotated by belt-drive. The second approach is to use a continuous wire saw, instead of a blade that claims to reduce the losses during the cutting process.

The kerf losses incurred during the wafer cutting process from the above methods is around 30%. The thickness of wafers produced is dependent on the thickness of blades or the diameters of wires. Presently, wafers of thickness ranging from $200 - 300\,\mu m$ are commonly produced. If necessary, the wafer is further polished down to the required thickness. In addition to this, the wafers are cut into much smaller rectangular shaped pieces in a process known as dicing. These pieces are used as substrates on ICs. These pieces are smaller usually by orders of magnitude as compared to the whole wafer. Therefore, the dicing process employs the use of lasers in automated fashion to increase the dicing efficiency.

One of the most recent and commonly used method for this purpose is the stealth dicing method [53]. In the stealth dicing process, a laser beam at a wavelength permeable to a semiconductor wafer is focussed through an objective lens onto a point within the semiconductor wafer and the beam made to scan along a dicing line. The extremely high focussing power of the optics combined with the high repetition and short pulses of the laser beam delivers a very high peak power density to an extremely localised region within the vicinity of the focal point [54–57]. Optimising the optical system and

laser characteristics allows controlling the focal point within the semiconductor wafer so that laser beam selectively machines only certain localised points without damaging the surfaces of the semiconductor wafer. A schematic of this process is shown in figure 1.5

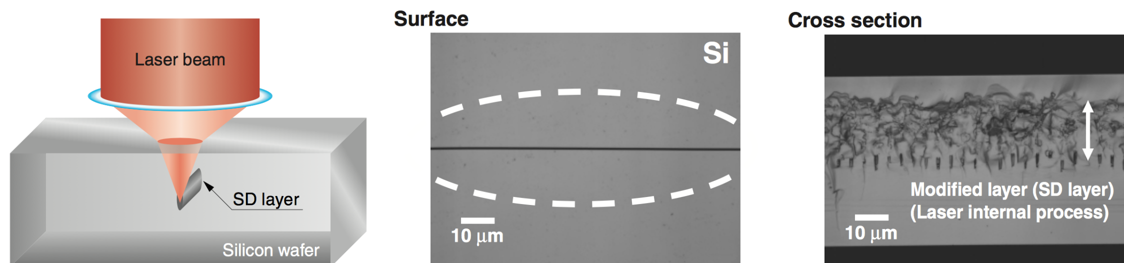

Figure 1.5: Stealth Dicing (SD): The laser beam is focussed inside a silicon substrate. The surface of the substrate has a clean cut and the subsurface is modified, as seen in the cross-sectional view. Source [58, 59]

Wafer Separation Methods

Wafer fabs continually face challenges in manufacturing semiconductor devices because the devices continue to get tinier and more complicated. Integrated circuits continue to increase in circuit density. Trends in chip design and materials, such as using die attach films and wafers as thin as $50\,\mu$m, add to the complexity of manufacturing. In fabrication processes, wafer dicing plays an early and critical role in the quality of the final product. For instance, separation of silicon wafer material is one of the essential processes in the semiconductor industry, including MEMS production and photovoltaic manufacturing.

Silicon wafers thicker than $100\,\mu$m traditionally are cut by diamond blades or saws, and the blade's thickness, grit size, and rotating and cutting speeds affect the cutting quality. This technique has been refined over the years, yet it still causes problems that cannot be ignored. Chipping of the wafer occurs because of the force of the sawing process. The large cut width (kerf) caused by the blade wastes the wafer and produces debris that must be cleaned up. Other issues include wearing down of the blade over time and the cost of blade replacement. Presently, this mechanical separation methods has reached its technological limits that will hinder both the ongoing trend of product miniaturization and the increase of the productivity in photovoltaic production. The major concerns and limitations of these separation technologies can be addressed, among others, as follows: mechanical stresses, dicing street contamination with material inherent debris or/and external material, limited machining speed (up to $200 mm/s$) and throughput, as well as imperfect edge quality.

For silicon wafers less than 100μm thick, laser ablation offers an alternative to the blade technique, which is too powerful for the delicate thin wafers. Laser ablation dicing has been proposed as preferable for thin and brittle materials compared to saw dicing. However, laser ablation has its own problems. Vaporising the wafer with a laser along the dicing path creates molten debris and micro-cracks. The debris deposition due to material ablation and reduced machining speed (in the range of $50mm/s$) deposited on the surface of the wafer is difficult to clean up, and the cracks result in chips with lower strength. Alternatively to the conventional laser ablation dicing, different other laser based silicon cutting technologies have been introduced recently: laser micro-jet separation, thermal laser separation, and laser-induced subsurface modification.

For clean and dry separation of silicon wafers, thermal laser separation with dry cooling as well as laser induced subsurface separation have been suggested as the most promising technology for MEMS dicing. From industrial point of view, slow processing speeds between $25mm/s$ and $300mm/s$ as well as the limited geometric shapes can be pointed out as major disadvantages for these technologies. In addition, laser cutting based on thermal stresses to silicon wafer by using a Gaussian single mode fibre laser is possible. Here, thermal gradients inducing compressive stress inside and tensile stress outside the laser spot is used to separate silicon in defined geometries. For this, an initial crack (seed crack) is created at the outer area of the wafer, subsequently following the laser beam along its path across the wafer. By using this method, the maximum processing speeds are $0.55m/s$ and 1.0 m/s obtained at 220μm and 60μm thick silicon wafers, respectively. Moreover, high machining qualities, vertical cutting edges, and completely flat cutting surface without any material losses or damage to the wafer surface is possible. Another technology called 'water assisted thermally driven separation mechanism' [60] works without a seed crack and silicon wafers with a thickness of 200μm are separated with a maximum cutting speed of $180mm/s$. All the conventional laser dicing methods use laser at wavelengths that can be highly absorbed by the material to be diced. This utilises physical phenomena such as heat melt cutting, ablation and thermal stress cutting due to absorption of the laser energy by the irradiated surface. Thus these methods have significant problems such as heat and debris that are unavoidable during laser machining. Monocrystalline silicon wafers generally absorb light at wavelengths shorter than $1000nm$ and tend to allow longer wavelength near-infrared range to transmit through them. If such longer wavelengths that transmit through silicon are guided to a focal point inside the wafer, selective and localised laser machining with the wafer is possible. A transmitting laser beam can be condensed by an objective lens and focussed onto a point inside the wafer. When the beam exceeds a peak power density during the condensing process, a nonlinear absorption process can take place leading to extremely high absorption at localised points. By optimising the laser and optical system characteristics to cause the nonlinear absorption effect just in the vicinity of the focal point inside the semiconductor wafer, only localised points in the wafer can be selectively laser-machined without damaging the front and

back surfaces of the wafer. This is the foundation of sub-surface modification of materials with lasers that transmit through the material.

Laser microstructuring via multiphoton absorption

The highly attractive property of nonlinear multiphoton absorption and subsequent modification is that the resultant modification or damage can be fine tuned to have smaller dimensions than that of the focus spot diameter of a typical Gaussian beam of the laser. This has allowed for opening of many interesting fields in integrated optics. The miniature size offered by integrated optics is crucial to taking experiments and turning them into consumer products. A lot of research is being done to create the so-called lab-on-a-chip or generally on-chip platforms. The basis of integrated optics lies in the ability to create extremely efficient waveguides in the substrate material. The advantage of creating integrated optics in silicon is that the existing CMOS technology would be able to easily merge with the novel integrated optics technology. This possibility is tested during the course of this work. Also, the possibility of creating efficient 3D waveguides in polymers such as SU-8 via multiphoton absorption is also tested. This, however, omits the integration of electronic and optoelectronic components with the integrated optics. A premier example of this integration approach is the glassPack - an integrated photonic package in a glass substrate (see figure 1.6) that works as an electro-optical transceiver [45, 61, 62]. It was designed and manufactured at the Fraunhofer Institute for Reliability and Microintegration in Berlin.

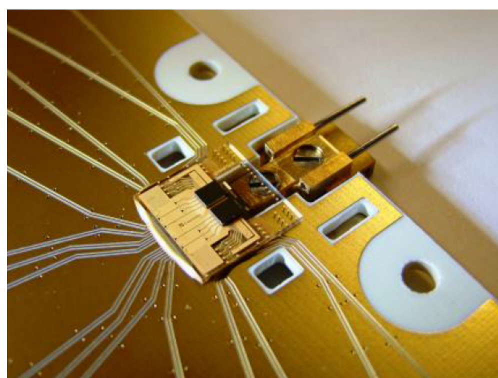

Figure 1.6: glassPack transceiver with data rates of $4 \times 12 Gbit/s$. Golden: electrical fan-out; Black rectangles: trans-impedance amplifier (TIA)/driver with photodiode (PD)/ vertical cavity side emitting laser (VCSEL); Two pins: alignment pins for a MT ferrule; Reflection between pins and first screw: end facet of glass waveguide between TIA/driver and pins. Source [61]

1.3 Motivation

The planar CMOS architecture currently used in the semiconductor industry will soon reach its physical limits [63]; also increasing power losses due to metal interconnects are becoming more and more challenging [64]. Therefore, novel methods and architectures will be required to further improve the packing density on a chip. Additionally, so-called “more-than-Moore” approaches of tackling these problems consider to increase the functional density of a chip rather than merely the transistor density. For this reason, it has long been considered [65, 66] to supplement CMOS technology by photonic approaches. Photonics aims to integrate the creation, tailoring, transmission and detection of light at the micro and nano scale akin to existing electronics[67–69]. Chip designers and manufacturers investigate various possibilities of integrating photonic architecture on electronic chips [70, 71], see example given in figure 1.7.

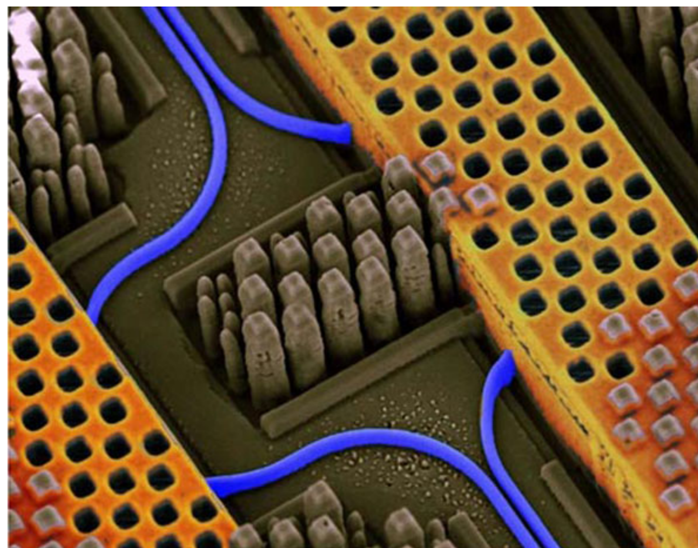

Figure 1.7: Electron micrograph (in false-colour) of a chip from IBM with optical waveguides (blue) alongside conventional copper inter- connects (yellow) integrated on a single chip, based on 90 nm technology. Source [70]

This is one of the primary motivations behind this thesis. To exploit the advantages of laser structuring via nonlinear processes in crystalline silicon and polymers and to determine the limits to which integrated optics can be utilised in everyday consumer products.

1.4 Objective and outline

The primary objective of this research is to study the subsurface modification of single crystalline silicon via laser irradiation. The subsequent objective is to study the bulk material modifications in transparent materials such as polymers and glasses.

The motivation for this research stemmed from a requirement to introduce a laser based process to cut thin single crystalline silicon films from its ingots. To be able to perform this, the following topics had to be studied and understood:

1. Multiphoton absorption and associated nonlinear processes in silicon
2. Damage threshold in bulk of silicon
3. Process parameters to cause modifications in silicon
4. Analytical model to understand the physical processes

Since the literature available on the above mentioned topics was sparse, at the time of conducting this research, the goals of this thesis were accordingly adapted and executed. To begin with, a laser system was chosen that provided enough parameter spectrum to create and analyse the nonlinear processes in silicon. For this reason, a number of lasers were short-listed and experiments were performed, of which only the Raydiance MD-50 showed promising results. The details are discussed in the next chapter.

The goals and objectives of this thesis are as follows:

1. To review the analytical model to investigate the nonlinear processes in polycarbonate and silicon and to identify the necessary parameters to induce these processes.
2. To develop and improve the experimental set-up in order to make it more versatile to include μm to nm precision. As a technical aspect, the writing process to enable writing complex 3D structures had to be automated.
3. To create subsurface modifications in silicon and to investigate three dimensional subsurface modifications in polycarbonate and extend applications to holography.
4. To investigate three dimensional polymer lithography for photonic applications.
5. To design and construct an optical vector matrix multiplier as a proof of concept of extending micro sized lithography to macro sized optoelectronics.

This thesis is divided into six chapters. Following the introduction in this chapter, the second chapter reviews the analytical model describing the nonlinear processes in polycarbonate and applies it to the nonlinear processes in silicon and subsequent subsurface

modifications. The interaction between laser irradiation and materials is discussed in this chapter.

The third chapter describes the experimental set-up designed and used during the course of this work. Other experimental devices, bought and developed, are also discussed in detail.

The fourth chapter concentrates on the subsurface modification in silicon. The methods used and the process parameters along with the results are discussed in detail. It also introduces three dimensional polymer optical waveguides that were designed and fabricated for on-chip optical communication. Various designs along with their advantages and disadvantages are discussed.

The fifth chapter concentrates on the bulk material modification in polycarbonate and Foturan glass. The applications of bulk three dimensional and subsurface modifications are discussed. The materials used and the process parameters are also discussed. Bulk modification of Foturan glass is demonstrated for its use in holography. This chapter also covers the experimental Optical Vector Matrix Multiplier as a prototype to demonstrate macro-scale on chip optical connections with optoelectronic components.

The sixth and final chapter in this thesis summarises and concludes all the above mentioned topics and also suggest a few improvements that can be implemented to extend the scope of this work.

The appendices collects data sheets and sample codes to demonstrate the working principle of the instruments that were built during the course of this work. Appendix A contains the details of the components used in the Laser enabled Nano-structuring Apparatus (LeNA). It also shows the technical details of hardware and the software (user interfaces) that is used and programmed specifically during the course of this work. Appendix B contains sample codes for 'yet another language' (yal) - a scripting language syntax that was developed during the course of this work for LeNA. Appendix C contains the technical details from the data sheets for the electronic and opto-electronic components used for the optical vector matrix multiplier.

2 Laser Irradiation and Material Interaction

If we knew what it was we were doing, it would not be called research, would it?

— **Albert Einstein**

In this chapter, an analytical model is presented to explain laser-silicon and laser-polycarbonate interactions. The few initial observations are shown and discussed that were used to determine the type of laser to be used in the experiments. The experimental parameters are calculated and are compared against existing technologies.

2.1 Introduction

Laser structuring is a process to selectively remove materials from a substrate to create a desired feature on or inside the substrate. The process has a high spatial confinement despite being contact-less. Compared to other mechanical machining techniques, laser structuring exhibits low heat deposition to the substrate. The process generally relies on the linear optical absorption and plasma formation mechanisms. However, conventional laser structuring, CW or pulsed, cannot create micron-sized structures because linear optical absorption of the materials often lead to heat deposition, micro-cracks and observable collateral damage to the substrate. To avoid this and to achieve the aims and objectives of this thesis, as described in section 1.4, we employ the nonlinear optical methods. In this chapter, the physics of these nonlinear optical methods which includes multiphoton absorption, avalanche ionisation, etc. will be discussed. Based on the information available in literature and our analytical model, the laser parameters that are used will be estimated. To begin with, the crystal structure of silicon and polycarbonate along with its acousto-opto and optoelectronic properties are briefly discussed.

2.2 Material properties of silicon

Monocrystalline or single-crystal silicon is a semiconductor element with an atomic number 14. At room temperature, it is a solid with a melting temperature of $1687\,K$. In its natural state, it crystallises into a diamond cubic lattice structure. Crystalline silicon has a grey colour and a metallic lustre. Despite being mechanically strong, it is brittle. The electronic configuration of silicon is - $1s^2 2s^2 2p^6 3s^2 3p^2$. The $1s$, $2s$, and $2p$ sub-shells are completely filled while the $3p$ sub-shell contains two electrons out of a total possible 6. The outer valence shell of silicon, therefore, has four valence electrons; thereby making it a semiconductor. Like most semiconductors, it has a negative temperature coefficient of resistance. This is because the number of free charge carriers increases with temperature. Silicon is also a metalloid. With four electrons in its outer shell, it readily forms four bonds with many other elements or compounds to form other compounds. The high strength of silicon-oxygen bonds dominates the chemical behaviour of silicon - which coincidently, is also its naturally occurring form as silicon dioxide. A few material parameters of crystalline silicon is listed in table 2.1.

Table 2.1: Material parameters of silicon at 300 K

Parameter	Value
Crystal structure	Face centred diamond cubic
Band gap	$1.12\,eV$
Space group	$Fd-3m$
Thermal conductivity	$149\,Wm^{-1}K^{-1}$
Debye temperature	$640\,K$
Density	$2.329\,gcm^{-3}$
Dielectric constant	11.7
Lattice parameter	5.431 Å
Bulk modulus	$97.6\,GPa$
Young's modulus	$130-188\,GPa$
Hardness	7 on the Mohs scale
Cleavage plane	{111}

Silicon has three stable naturally occurring isotopes: ^{28}Si, ^{29}Si, and ^{30}Si. Of these three, ^{28}Si is the most abundant and also most commonly used in semiconductor industry to make ingots. A handful of radioisotopes also have been discovered and characterised, eg. ^{32}Si ($t_{1/2}$ = 170 years) and ^{31}Si ($t_{1/2}$ = 157 minutes).

2.2.1 Crystal structure

The unit cell of silicon consists of:
8 atoms at corners at 1/8 each in cell
6 atoms in faces at 1/2 each in cell
4 atoms within the cell

Thus, there are 8 silicon atoms per unit cell as shown in figure 2.1. Apart from this state, which is also known as Si-I, silicon exists in many stable and quasi-stable states that have different crystalline phases. However, most of these phases exist in pressure regimes of greater than $10GPa$. Amorphous silicon or a-Si is the non-crystalline form of silicon. Its made by vapour deposition of crystalline silicon on glass or metal. Besides these two forms, there is also an intermediate polycrystalline (poly-Si) stage where the atoms are arranged in a semi-continuous ordered lattice. At ordinary pressure, silicon exists in the Si-I state and crystallises in the diamond structure with an FCC (Face Centred Cubic) Bravais lattice. The chemical bond is purely covalent in nature. Each atom in the Bravais lattice is tetrahedrally coordinated and the valence electrons form an sp^3 hybridisation state.

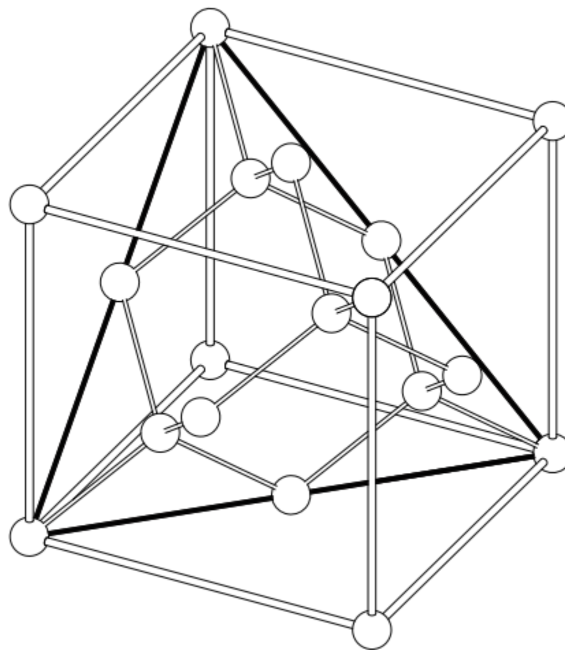

Figure 2.1: Silicon unit cell. The thick black lines indicate the {111} cleavage plane. Source [72]

The lattice parameter of silicon has a linear temperature dependence. This dependence can be expressed in terms of a linear thermal expansion coefficient, $\alpha(T)$. The value of

this coefficient was calculated between $300\,K$ and $1500\,K$ by Okada and Tokumaru [73] and can be expressed phenomenologically as

$$\alpha(T) = (3.725(1 - exp(-5.88 \times 10^{-3}(T - 124))) + 5.548 \times 10^{-4}T) \times 10^{-6}K^{-1} \tag{2.1}$$

where T is the absolute temperature expressed in Kelvin. α varies from 0 to $4.5 \times 10^{-6}K^{-1}$ between $130\,K$ and $1400\,K$. The lattice parameter, thus, can be expressed in terms of α as

$$a(T) = a_0\left[\int_{295.7}^{T} \alpha(T)dT + 1\right] \tag{2.2}$$

where a_0 is the lattice parameter at $295.7\,K$.

Impurities in monocrystalline silicon that may arise during its production can also significantly alter its lattice parameters. According to Vegard's law [74], if the atomic radius of the impurity atom is small than the atomic radius of the parent atom (silicon) then unit cell of the crystal will undergo a uniform contraction or expansion in proportion to the concentration of the impurity atoms. This modification is expressed by

$$\frac{\Delta a}{a} = \beta N \tag{2.3}$$

where N is the concentration of the impurity atoms. The coefficient β is dependent on the impurity atom. The most frequent impurities in silicon are oxygen and carbon and the β values are $-6.9 \pm 0.5 \times 10^{-24}\,cm^3/atom$ and $4.4 \pm 0.2 \times 10^{-24}\,cm^3/atom$, respectively [75]. It is apparent from these values that carbon decreases whereas oxygen increases the lattice parameter in silicon.

The density of silicon is $2.3296\,g/cm^3$ at $300\,K$. This value has been perfected and verified over the years [76–81] with extremely great accuracy. It is noteworthy to mention here, that currently, the Physikalisch-Technische Bundesanstalt or the National Metrology Institute of Germany is actively involved in redefining the kilogram in terms of basic universal constants. For this reason, a crystalline silicon sphere of an extremely precise volume is fabricated using various optical metrology techniques and using the known values of the Avogadro constant, the kilogram is redefined with better accuracy and stabler values [82]. As of October 2016, these silicon spheres are successfully fabricated and are

ready to be presented at the General Conference on Weights and Measures in 2018. The calculation of the Avogadro constant follows the simple equation

$$N_A = nM/\rho a^3 \tag{2.4}$$

where n is the number of atoms per unit cell of a silicon crystal which is 8. ρ is the density, M is molar mass, and a is the lattice parameter of monocrystalline silicon.

2.2.2 Band structure

Silicon is an indirect semiconductor, which means that the maximum energy of the valence band occurs at a different value of crystal momentum to the minimum energy in the conduction band. Phonon assistance is in this case required to excite an electron from the valence band to the conduction band, using a single photon. Figure 2.2 shows the intrinsic silicon band structure at room temperature (300K). The indirect band gap can be seen along the [100] axis between $k = 0$ and $k = 2\pi/a$, a being the lattice parameter of silicon. The value of this band gap is 1.08 eV for intrinsic silicon at 300 K. One can also, however, notice that silicon possesses a direct band gap at k = 0, which has a value of 3.4 eV under similar conditions. This corresponds to a photon wavelength of $\approx$ 360 nm and an absorption depth of around $1\mu m$. This implies that a ultraviolet laser (at 360 nm) cannot be focused into the silicon bulk without inducing surface damages.

The energy bandgap varies with temperature and this is mainly attributed to two internal mechanisms in silicon:

1. Change in bond lengths - related to thermal expansion coefficient [83]
2. Electron-phonon interaction [84]

At temperatures around $100\,K$, the energy band gap strongly reduces with temperature non-linearly whereas at higher temperatures, many theories predict a linear shift. This behaviour is understood if one considers the inter-atomic spacing increasing when the amplitude of the atomic vibrations increases with increased thermal energy, which is dependent on the linear expansion coefficient of silicon. An increased spacing decreases the potential as seen by the electrons in the material which in turn reduces the size of the

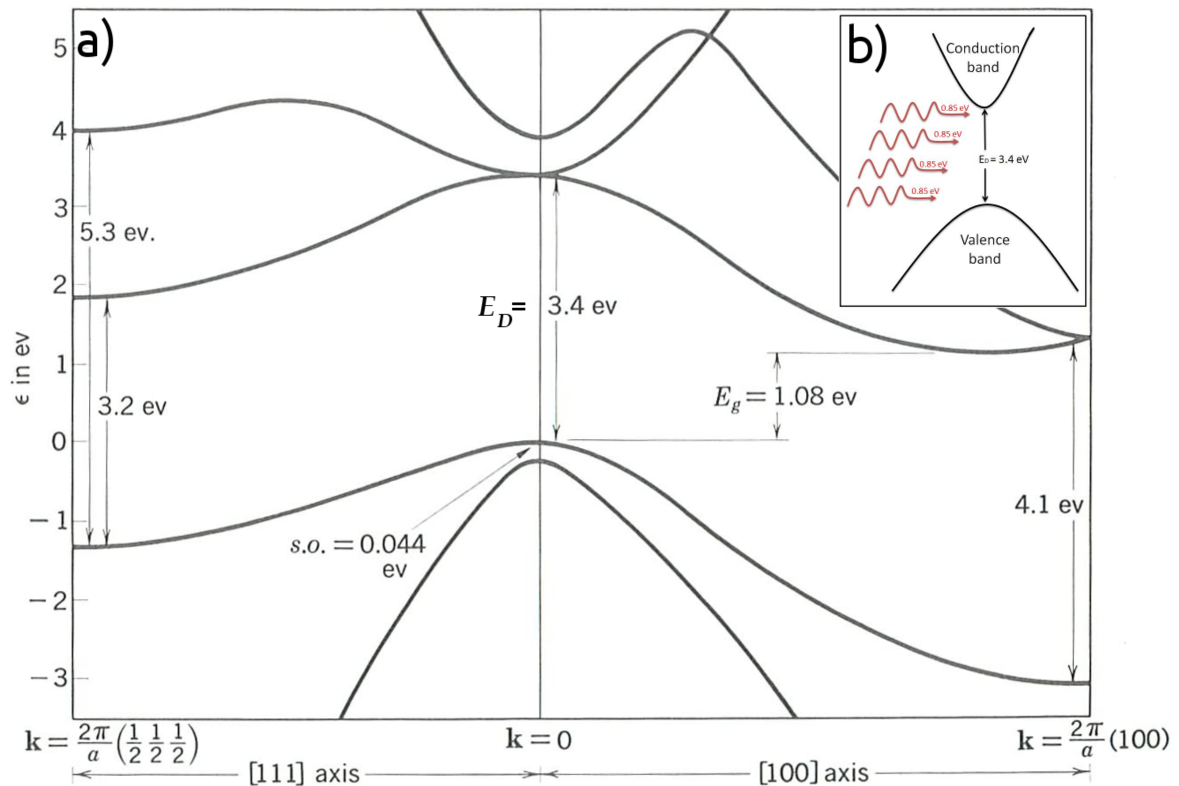

Figure 2.2: A band diagram of undoped silicon at room temperature. The zero energy level is set at the top of the valence band. The indirect band gap E_g = 1.08 eV and the direct band gap E_D = 3.4 eV at k = 0. Inset: Multiphoton absorption process in silicon. The arrows in red depict the infrared photons used in the experiment, each having energy of 0.85 eV. E_D = 3.4eV. Source [72]

energy bandgap. One of the most commonly accepted empirical and analytical expressions used to determine the energy bandgap is

$$E_g(T) = E_g(0) - \frac{\alpha T^2}{T+\beta} \tag{2.5}$$

where $E_g(0)$ is the energy band gap at $T = 0$ and α, β are fitting parameters that are experimentally determined. For silicon, the experimentally determined values of α and β are $4.73 \times 10^{-4}\, eV/K$ and $636\, K$. The bandgap can also be altered by directly modulating the inter-atomic distance, such as by applying high compressive stresses in silicon.

2.3 Material properties of polycarbonate

Polycarbonates is a name given to a group of plastic polymers containing carbonate groups in their chemical structures. Since they are artificially manufactured, their physical properties can be accurately engineered as desired within the allowed parameters. They belong to the thermoplastic group of polymers, which means that they are moldable above a specific temperature and harden upon cooling. Chemically, they are long chain linear polyesters of carbonic acid and di-hydric phenols, such as bisphenol A, as shown in figure 2.3. These two phenyl groups (hexagons) in the polymer chain are largely responsible to the molecular stiffness in polycarbonate. The attractive forces acting between these two groups contributes to the lack of mobility to individual molecules. This results in good thermal resistance and relatively high viscosity. This feature also prevents polycarbonate from developing any crystalline structure. A few important material parameters are listed in table 2.2.

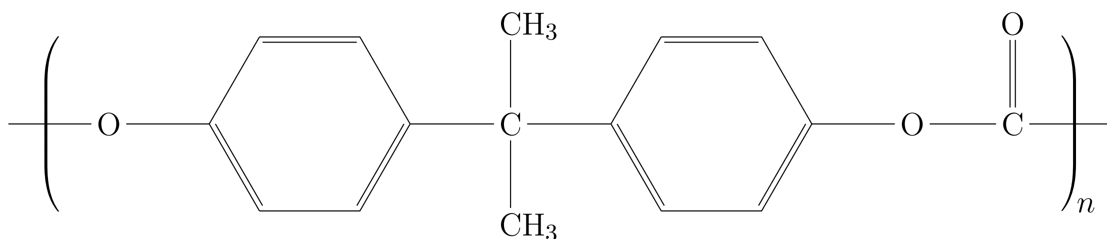

Figure 2.3: Repeating chemical structure unit of polycarbonate made from bisphenol A. The two methyl groups are attached to the carbon atom and the hexagons represent the two phenyl groups.

Table 2.2: Material parameters of polycarbonate at 300 K

Parameter	Value
Thermal conductivity	$0.19-0.22\,Wm^{-1}K^{-1}$
Specific heat capacity	$1.2-1.3\,kJK^{-1}kg^{-1}$
Density	$1.2\,gcm^{-3}$
Dielectric constant	$2.9@10MHz$
Refractive index	1.584
Young's modulus	$2-2.5\,GPa$

2.4 Material properties of SU-8

SU-8 is a near-UV negative photoresist designed for MEMS and other microelectronic applications. It was originally developed and patented by IBM [85]. When SU-8 is exposed to UV light its molecular chains cross-link, causing the SU-8 to solidify. It is also highly transparent in the ultraviolet range. It allows for the fabrication of hundreds of micrometers tall structures with nearly vertical side walls. The large quantity of epoxy moieties gives SU-8, excellent mechanical and chemical stability against many acids and bases when polymerised. Meanwhile, the benzene rings in the monomer give it high absorptive property in the UV range ($< 300\,nm$). The '8' in SU-8 refers to the presence of 8 epoxy groups (see figure 2.4) that cross-link to give the final structure. A few physical properties of SU-8 are given in table 2.3.

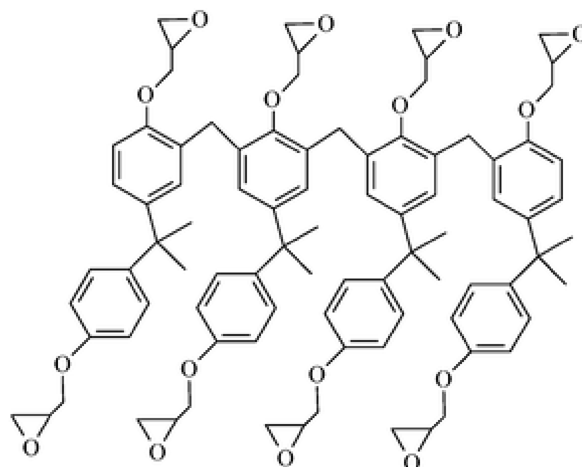

Figure 2.4: Molecular structure of SU-8 monomer. It contains eight reactive epoxy groups and eight benzene rings in its chemical structure. Source [86]

Table 2.3: Material parameters of SU-8 at 300 K

Parameter	Value
Adhesion Strength - Silicon/Glass	$38/35\,mPa$
Glass Transition Temperature	$210°C$
Thermal conductivity	$0.3\,Wm^{-1}K^{-1}$
Tensile Strength	$60\,MPa$
Dielectric Constant	$3.2@10MHz$
Young's Modulus	$2.0\,GPa$
Water Absorption	$0.65\,\%wt\,@85°C, 85RH$

2.4.1 Processing guidelines for SU-8

Currently, the company Microchem [87] manufactures SU-8 resist in numerous variants. SU-8 2000 is an improved formulation of the earlier SU-8 resist. It is a faster drying and more easily soluble in many polar solvents. This allows for a uniform coating layer and higher throughputs. Variations of this resist are available that allow for different coating thickness at different spin coating parameters. A complete work flow of the SU-8 process is shown in figure 2.5.

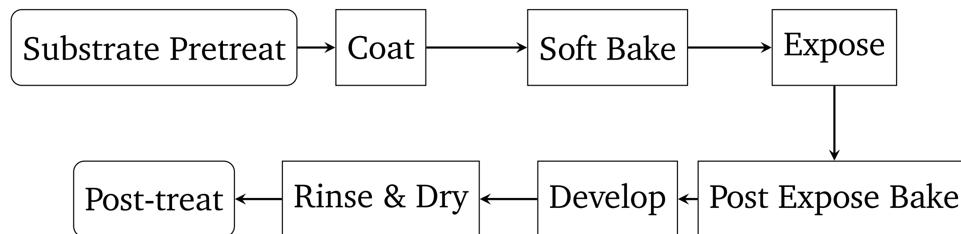

Figure 2.5: Work flow of SU-8 process. A normal process is: spin coat, soft bake, expose, post expose bake, followed by develop. The entire process is to be optimised for the specific application.

SU-8 2000 photoresist is most commonly exposed with conventional UV (350-400 nm) radiation. The i-line (365 nm) is the recommended wavelength. SU-8 2000 can also be exposed with e-beam or x-ray radiation. Upon exposure, cross-linking proceeds in two steps:

1. Formation of a strong acid during the exposure step
2. Acid-catalysed, thermally driven epoxy cross-linking during the post exposure bake step

The substrate is pretreated by cleaning it with a piranha wet etch (H_2SO_4 & H_2O_2) followed by rinsing it with deionised water. They can also be cleaned by using reactive ion etching method. Next, they are spin coated with SU-8 using a set of calibrated parameters

that determine the thickness of the final coating. The thickness varies depending on the viscosity of the resist used. In the case of 3D laser lithography, this step usually consists of placing a drop of SU-8 on the surface of the substrate. Soft baking is required to ensure effective acid formation during the exposure step. Soft bake also enables high aspect ratio structures in the resist. In 3D laser lithography, this step is often skipped. The resist is then exposed to UV light under a photo mask for a very specific duration of time. During the post exposure bake step, cross linking of the thermally driven epoxy groups takes place. This also ensures extremely strong adhesion to the surface of the substrate. When the resist is developed, the unlinked areas are washed away and the desired structure remains. The substrate is then post treated either via a hard bake procedure or just drying it using pressurised air or nitrogen.

This is a standard procedure for using a negative tone resist, such as SU-8. Positive tone resists and image reversal resists include a few extra steps, such as flood exposure. The difference between positive and negative tone photoresists are described in the next subsection. The resist used in the fabricated of optical micro structures during the course of this work is a variant of the SU-8 resist and is officially known as the IP-L resist. It was made by the company Microchem for the company Nanoscribe GmbH.

2.4.2 Positive and negative photoresists

There are two types of photoresists: positive and negative. In positive resists, the resist is exposed with UV light wherever the underlying material is to be removed. In these resists, exposure to the UV light unlinks the chemical structure of the resist so that it becomes more soluble in the developer. The exposed resist is then washed away by the developer solution, leaving windows of the bare underlying material. The photo mask, therefore, contains an exact copy of the pattern which remains on the substrate. Examples of positive tone resists are, PMMA Series (e-beam), S1800 Series (g-line), SPR-220 (i-line), and ma-P1200 Series (broadband).

Negative resists behave in just the opposite manner. Exposure to the UV light causes the negative resist to become polymerised. Therefore, the negative resist remains on the substrate wherever it is exposed, and the developer solution removes only the unexposed portions. Masks used for negative photoresists, therefore, contain the inverse of the pattern to be transferred. The figure 2.6 shows the pattern differences generated from the use of positive and negative resists. Examples of negative tone resists are, SU-8 Series (i-line), KMPR Series (i-line), UVN-30 (DUV), ma-N 1400 Series (i-line), and ma-N 2400 Series (DUV).

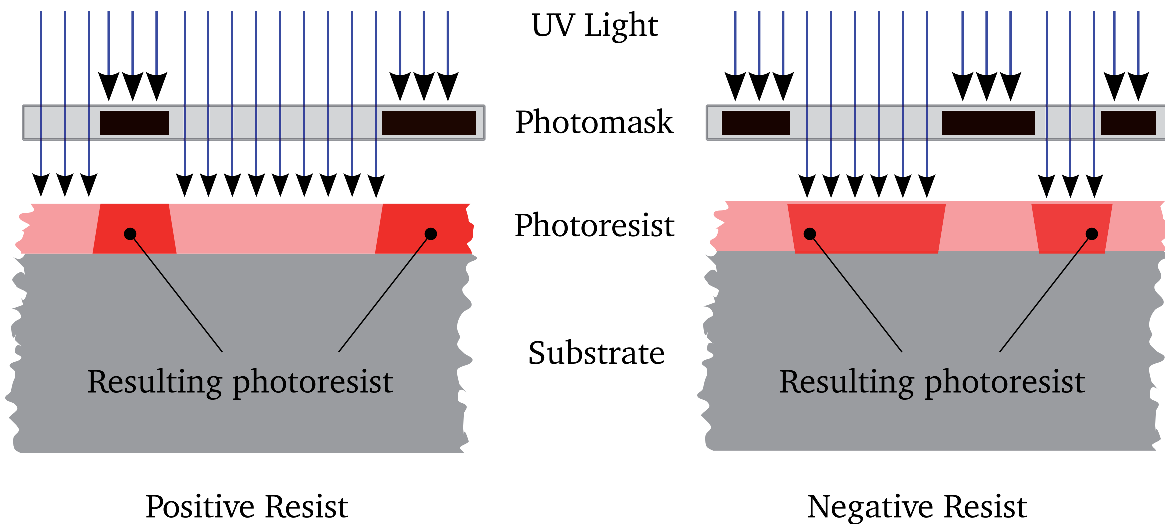

Figure 2.6: Comparison of patterns generated between positive and negative photoresists. The photomask blocks the incoming UV light and hinders the reaction with the resist in its shadow. The resulting photoresist pattern is obtained after developing the substrate.

Apart from these two kinds, there is also a third kind of photoresist called the Image Reversal Photoresist. This is often intended for lift-off-techniques which call for a negative wall profile. Lift-off- technique is a process in which a substrate, after being deposited with the desired metal, is developed to lift-off the undesired metal surfaces along with the resist; thus leaving only certain metallic patterns on the substrate. The image reversal capability is obtained by a special cross-linking agent in the resist formulation which becomes active at temperatures above $110°C$ only in exposed areas of the resist. The cross-linking agent together with exposed photo-active compound leads to an almost insoluble (in developer) and no longer light sensitive substance, while the unexposed areas still behave like a normal unexposed positive photoresist. After a flood exposure (mask-less) these areas are dissolved in standard developer for positive photoresist, the cross-linked areas remain. The overall result is a negative image of the mask pattern. This allows for extremely accurate metallisation of the substrate which is required for making micro-electrical contacts.

2.5 Laser material interaction

The generation and interaction of laser light pulses revolve around the subject of light and matter interaction. A beam of laser passing through a material with little or no change in the material response is relatively easy to model. It can be represented as a linear dependence of the output field on the input field - which is a feature often attributed to the linear optical elements. The medium, in this case, is described by a transfer function

$H(\Omega)$, which for a material, is completely determined by a complex dielectric constant $\epsilon(\Omega)$. The real part of $\epsilon(\Omega)$ is responsible for dispersion, phase and group velocity. The imaginary part is responsible for the frequency dependent loss or gain. If the intensity of the laser beam is 'high' enough, then nonlinear optical effects in the material become more prominent, in which case many complex physical phenomena occur in the material and beam propagation. The next few subsections will focus initially on linear optical interaction and later with the aforementioned nonlinear optical phenomena in materials.

2.5.1 Maxwell's equations

Any electromagnetic field can be described by two related vector fields: the electric ($\vec{E}(r,t)$) and the magnetic field ($\vec{H}(r,t)$), that are both vector functions of position and time. In general, six scalar functions of position and time are required to describe any electromagnetic field. These functions satisfy a set of coupled partial differential equations and related to one another. Together they are known as Maxwell's equations. In a medium with no free charges or currents, two more vector fields are needed to define the propagation of light namely, the electric flux density or the electric displacement ($\vec{D}(r,t)$) and the magnetic flux density ($\vec{B}(r,t)$). The four Maxwell's equations that relate the four fields, $\vec{E}, \vec{H}, \vec{D}$, and $\vec{B}$, are:

$$\nabla \times \vec{E} = -\frac{\partial \vec{B}}{\partial t} \tag{2.6}$$

$$\nabla \times \vec{H} = \frac{\partial \vec{D}}{\partial t} \tag{2.7}$$

$$\nabla \cdot \vec{D} = 0 \tag{2.8}$$

$$\nabla \cdot \vec{B} = 0 \tag{2.9}$$

The relation between the electric flux density $\vec{D}$ and the electric field $\vec{E}$ depends on the electric properties of the medium. Similarly, the relation between the magnetic flux density $\vec{B}$ and the magnetic field $\vec{H}$ depends on the magnetic properties of the medium. The two equations that define these dependencies are:

$$\vec{D} = \epsilon_o \vec{E} + \vec{P} \tag{2.10}$$

$$\vec{B} = \mu_o \vec{H} + \mu_o \vec{M} \tag{2.11}$$

where, $\vec{P}$ is the polarisation density and $\vec{M}$ is the magnetisation density. In a dielectric medium, the polarisation density is the macroscopic sum of the electric dipole moments that the electric field induces and the magnetisation density is the macroscopic sum of the magnetic dipole moments that the magnetic field induces. In free space, $\vec{P} = \vec{M} = 0$, so that $\vec{D} = \epsilon_o \vec{E}$ and $\vec{B} = \mu_o \vec{H}$. If the electromagnetic wave passes through a non-magnetic medium, then $\vec{M}$ will be equal to 0.

When an electric field interacts with a medium, it creates a polarisation density as shown in the equations above. This polarisation density can be represented by a polarisation vector $P(\vec{r}, t)$. The properties of a dielectric medium can be described solely based on the relationship between these two vectors, as shown in table 2.4.

Table 2.4: Material properties of a dielectric medium based on relationship between the electric field vector $\vec{E}$ and the polarisation vector $\vec{P}$.

$\vec{E} - \vec{P}$ relationship	Material property
$\vec{P} \propto \vec{E}$	Linear medium
$P(\vec{t})$ is determined by $E(\vec{t})$	Medium is instantaneous and non-dispersive
$\vec{P} \& \vec{E}$ are independent of position r	Medium is homogeneous
Independent of the direction of $\vec{E}$	Medium is isotropic $\Rightarrow$ the vectors are parallel

In the case of a linear, non-dispersive, homogeneous, and isotropic media, the vectors $\vec{P}$ and $\vec{E}$ at any position and time are parallel and proportional. So, the following equation holds true

$$\vec{P} = \epsilon_o \chi \vec{E}, \tag{2.12}$$

where χ is a scalar constant called the electric susceptibility of the medium. From equations 2.10 and 2.12, one can deduce that

$$\vec{D} = \epsilon \vec{E}, \tag{2.13}$$

where

$$\epsilon = \epsilon_o (1 + \chi) \tag{2.14}$$

is another scalar constant called the electric permittivity of the medium. The ratio ϵ / ϵ_o is the relative permittivity or the dielectric constant. From these deductions, the Maxwell's equations for a linear, instantaneous, homogeneous, and isotropic media can be simplified to

$$\nabla \times \vec{H} = \epsilon \frac{\partial \vec{E}}{\partial t} \tag{2.15}$$

$$\nabla \times \vec{E} = -\mu_o \frac{\partial \vec{H}}{\partial t} \tag{2.16}$$

$$\nabla \cdot \vec{E} = 0 \tag{2.17}$$

$$\nabla \cdot \vec{H} = 0 \tag{2.18}$$

An assumption that is inherent in these deductions is that for $\vec{E}$ and $\vec{H}$ to satisfy Maxwell's equations, each of their components should satisfy the wave equation, as shown in equation 2.19.

$$\nabla^2 u - \frac{1}{c_o^2}\frac{\partial^2 u}{\partial t^2} = 0 \tag{2.19}$$

where

$$c_o = \frac{1}{\sqrt{\epsilon_o \mu_o}} \approx 3 \times 10^8 \, ms^{-1} \tag{2.20}$$

During the course of this thesis, several nonlinear dielectric media were used. This means that the relation between P and E is nonlinear. If the medium is homogeneous, isotropic and non-dispersive, then P is a nonlinear function of E, which can be written as

$$P = a_1 E + a_2 E^2 + a_3 E^3 + \ldots, \tag{2.21}$$

where $a_1, a_2, a_3, \ldots$ are appropriate constants. The wave equation described in 2.19 does not apply to electromagnetic waves in nonlinear media. However, using Maxwell's equations, a suitable partial differential equation can be deduced which these electromagnetic waves in nonlinear media obey. If we operate with a curl operator ($\nabla \times$) on the Maxwell's equations shown in equations 2.6 and 2.7, we obtain using the relation $B = \mu_o H$, $\nabla \times (\nabla \times E) = -\mu_o \partial^2 D / \partial t^2$. Using the relation, $D = \epsilon_o E + P$, we can write

$$\nabla(\nabla \cdot E) - \nabla^2 E = -\epsilon_o \mu_o \frac{\partial^2 E}{\partial t^2} - \mu_o \frac{\partial^2 P}{\partial t^2}. \tag{2.22}$$

For a homogeneous and isotropic medium $D = \epsilon E$ and from Maxwell's equation, $\nabla \cdot D = 0$. Therefore, $\nabla \cdot E = 0$. Substituting this and the relation $\epsilon_o \mu_o = 1/c_o^2$, we obtain

$$\nabla^2 E - \frac{1}{c_o^2}\frac{\partial^2 E}{\partial t^2} = \mu_o \frac{\partial^2 P}{\partial t^2}. \tag{2.23}$$

The equation 2.23 is applicable to all homogeneous and isotropic dielectric media. Since the equation is nonlinear, it cannot be super-positioned. This equation describes the electromagnetic wave propagation in a nonlinear media. In this thesis, due to the use of high powered and highly focussed laser beams, the medium responds non-linearly to the applied laser beam.

2.5.2 Ultrafast laser material interaction

Integrated optical components can be directly inscribed into the bulk of transparent materials by using the focused femtosecond laser beam due to the locally altered structures and properties in the host materials. The femtosecond laser induced structures exhibit enormous potentialities for widespread applications of micro-photonic crystals, coupler, 3D optical data storage, bio-photonic components, multicolour imaging, and so on. The advantages of femtosecond laser microstructuring in transparent materials over other photonic micro-device fabrication techniques are numerous.

Physical processes such as phase transitions, chemical reactions, oscillation of atoms and molecules take place on timescales in the range of femtoseconds to picoseconds. Femtosecond lasers have thus been used to study fundamental physical processes in solids occurring on ultrashort time scales. Figure 2.7 shows the timescale of different processes.

Upon irradiating a material with a laser, the electrons in the material absorb the incident laser energy which leads to an increase of the electron kinetic energy. The activated electron transfer the energy to the lattice by means of electron-lattice collisions leading to the rise in material temperature. The time taken for the excited electronic states to transfer energy to the phonons and thermalise depends on the material properties. For most metals, this time is on the order of $10^{-12} - 10^{-10}\,s$. In non-metals the time taken can be as long as $10^{-6}\,s$. Polymers and dielectrics are on the slower end of this range. When the rate of the laser-induced excitation is lower than the thermalisation rate, the absorbed laser energy is directly transformed into heat. Such photo-thermal (pyrolytic) material response is observed upon laser processing of metals and semiconductors with slow laser

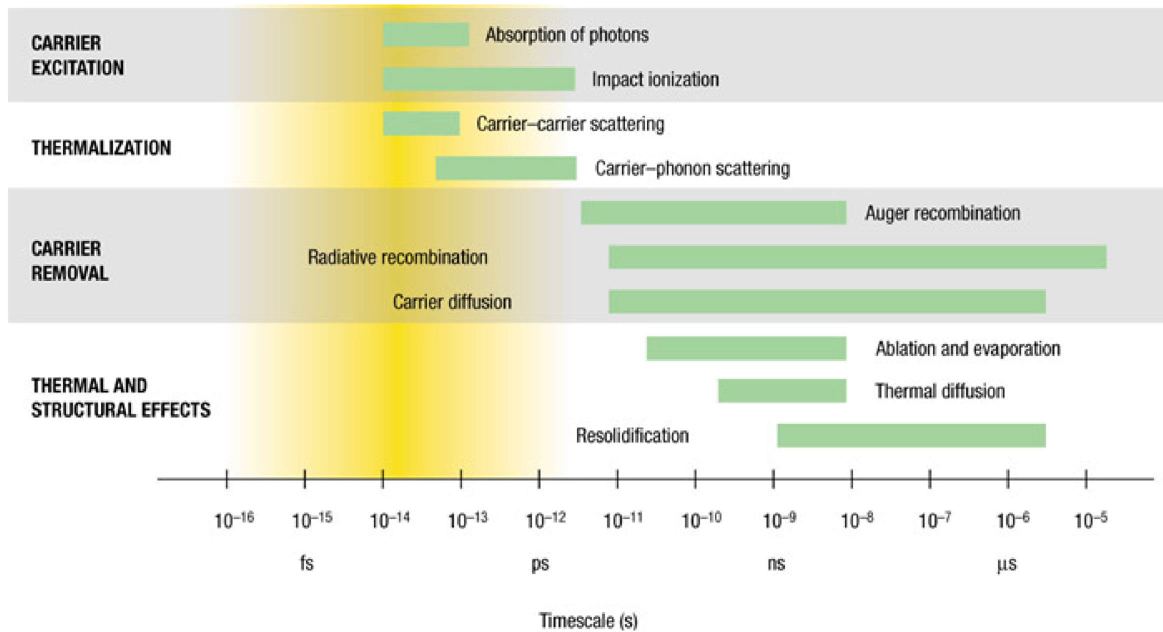

Figure 2.7: Timescale of the physical processes in materials when exposed to ultrafast laser pulses. The data is taken from reference [88]

pulse times $> ns$. However, when the laser induced excitation rate is high in comparison to the thermalisation rate, large excitations can build up in the intermediary states.

In this case, in a transparent material, no linear absorption of the incident femtosecond laser light occurs. With sufficiently high energy added into the target material, significant nonlinear absorption takes place, leading to transfer of electrons from the valence band to the conduction band. There are two classes of nonlinear excitation mechanisms that play a role in the nonlinear absorption, namely, multiphoton ionisation and avalanche ionisation.

2.5.3 Interaction of fs laser radiation with silicon

The non-linear effects in silicon originate from the interaction of the optical field with electrons and phonons. This arises, in principle, from the resonance of the electric field of the electric field of the optical signal with the electrons in the valence shell of the silicon atom which causes polarisation. The polarisation of the atom occurs by the displacement of an electron orbital, with respect to the nucleus, using a photon oscillating at a frequency ω.

It is well-known that the optical absorption in a dielectric media where the polarisation ($P(t)$) is induced due to an applied electric field ($E(t)$) in an isotropic material, assuming an instantaneous dielectric response, is given by the power series

$$P(t) = \varepsilon_o \chi^{(1)} E(t) + \varepsilon_o \chi^{(2)} E^2(t) + \varepsilon_o \chi^{(3)} E^3(t) + \ldots, \tag{2.24}$$

where χ is the electrical susceptibility of the material and defines the order of the interaction between E and P, and ε_o is the vacuum permittivity. The susceptibility terms are tensors of rank (i+1) and they describe:

1. if the relation between the induced polarisation would be linear or non-linear
2. if the electric fields would either induce phase-shift, or absorb, or amplify the incident field
3. if new frequency waves would be generated

At a wavelength of $1552nm$, the linear absorption coefficient of silicon is very low 10^{-8} cm^{-1} and hence, the first term in the above equation can be neglected. Silicon is a centrosymmetric crystal and belongs to the $m3m$ point group. The characteristic feature of crystals belonging to the $m3m$ point group is the absence of the second-order susceptibility term. Thus, the third-order susceptibility is the predominant contributing factor to the electromagnetically induced polarisation in silicon atoms. Thus, the above equation can be simply written as

$$P(t) \simeq \varepsilon_o \chi^{(3)} E^3(t). \tag{2.25}$$

By introducing the frequency components of the electric field E, one can expand equation 2.24 and derive the polarisation in terms of its frequency components. These can be associated with the physical processes such as self phase modulation (SPM) and third harmonic generation. The SPM leads to a local increase in the focussed electromagnetic densities which can further initiate non-linear processes such as the multi photon absorption (MPA) [28, 89]. The electromagnetic flux and the coefficients of absorption in MPA is governed by

$$-\frac{d}{dz} I(t,z) = \alpha I(t,z) + \beta I^2(t,z) + \gamma I^3(t,z) + \ldots \tag{2.26}$$

Here, I is the intensity of the electromagnetic radiation, z is the depth of the absorption, t is the time variable and α, β, γ are the first, second and third order photon absorption coefficients, respectively. The value of β is known to vary in between $1.8 - 0\,cm/GW$ in a wavelength range between $800 - 2200\,nm$ [90]. The maximum value in this range is $\approx 0.45\,cm/GW$ at $1550\,nm$ [91].

Multiphoton absorption creates the initial seed electron density which is then increased by the avalanche ionisation process. Initial ionisation takes place when a few seed electrons in the conduction band oscillate in the laser electromagnetic field and are accelerated to energies greater than the band gap of the silicon. These high energy electrons then interact with the valence electrons and transfer enough energy to excite them to the conduction band. This iterative process leads to an avalanche ionisation in the material [92]. The criteria for initiation of the avalanche ionisation by multi-photon process is given by the Keldysh parameter ($\epsilon_{osc}/\Delta_{gap}$) to be greater than unity. The parameters ϵ_{osc} and Δ_{gap} are the electron oscillation energy and the electronic band gap, respectively. The probability of the multiphoton absorption P_{mpi} per atom per second is given by

$$P_{mpi} \approx \omega n_{ph}^{3/2} \left(\frac{\epsilon_{osc}}{2\Delta_{gap}} \right), \tag{2.27}$$

Here, n_{ph} is the number of photons involved in the transition of one electron and $\Delta_{gap} = n_{ph}\hbar\omega$. Since the probability is directly proportional to the oscillation energy of the electron, the intensity of the incident electromagnetic radiation from the laser is critical in initiating the process. The subsequent generation of the electrons results in the formation of an electron plasma cloud that can exert an outward pressure inside the silicon crystal lattice. This outward pressure can lead to damage inside the bulk and the extent depends on the variation of the mechanical stress in different crystal orientations.

Based on the rate of the photon absorption and electron-phonon interactions, the time span in which the entire process takes place is of the order of 10^{-14} – 10^{-11} seconds. The defect formation is dependent also on the Young's modulus of the material and its thermal coefficients. In case of silicon, the time span is expected to be a couple of tens of nano seconds, as shown in table 2.5.

Table 2.5 shows, why silicon is much more difficult to process using multi photon absorption as compared to polymers, such as SU-8 and PMMA. The nonlinear effects are non-isotropic, which means that the crystal orientation plays an important role. The Young's modulus (averaged over primary crystallographic orientations) is $130\,GPa$, therefore the amount of electromagnetic energy to be concentrated to initiate the nonlinear effects is enormous as

Table 2.5: Comparison of physical parameters between polymers and silicon for 3D bulk modifications

Properties	Polymers	Silicon
Isotropic	Yes	No
Young's Modulus	$2-3GPa$	$130GPa$ (avg.)
Transparency	VIS-NIR	NIR
Thermal diffusivity (ξ)	$0.8mm^2/s$	$90mm^2/s$

compared to polymers. Also, in the case of dielectric polymers, the nonlinear processes are aided by their low values of thermal diffusion coefficient . This can be incurred from the fact that the time taken for a region of size l to cool down after being thermally excited is given by the relation $t \approx l^2/\xi$. The value of thermal diffusivity ξ for polymers is about 120 times lower than that of silicon [93]. This implies that glass can be micro-machined by depositing low energy laser pulses over a rather long duration of time, whereas in the case of silicon micro-machining, a high-repetition rate and a high pulse energy laser is necessary. Besides these restrictions, the transparency imposes a severe limitation on the availability of a laser system in the NIR region delivering sufficiently high intensities. Considering the fact that the linear absorption of silicon at $1552nm$ (wavelength used during the course of this work), is almost zero, equation 2.26 can be expressed as

$$\begin{aligned} -\frac{d}{dz}I(t,z) &= \cancel{\alpha I(t,z)} + \beta I^2(t,z) + \gamma I^3(t,z) + \dots \\ &= \beta I^2(t,z) + \gamma I^3(t,z) + \dots \end{aligned} \tag{2.28}$$

According to this equation, the value of β plays a major role in the multi-photon absorption process [91, 94]. This parameter directly describes the ability of silicon to absorb a given wavelength of light depending on the intensity. When this value is high enough, large values of electromagnetic radiation can be focussed at a given point and this can lead to a local change in the refractive index of the material. This is known as the Kerr effect. The local increase in the refractive index further focusses the already focussed light and leads to a chain reaction called 'self-focussing'. The increase in the refractive index is related to the second order Kerr coefficient. These parameters are related by

$$\eta = \eta_0 + \eta_2 I \tag{2.29a}$$

$$\eta_2 = \frac{3\chi^{(3)}}{8\eta_0} \tag{2.29b}$$

with η= increased refractive index, η_0= linear refractive index, η_2= second order nonlinear part of the refractive index and $\chi^{(3)}$= third order susceptibility. For silicon, the value of η_2 at $1552\,nm$ is found to be $4 \times 10^{-14}\,cm^2/W$ [95]. Thus, the local increase in the refractive index leads to further increase in the absorption of light and tighter focussing at the given point. This leads to a large deposition of energy in the lattice and subsequently the atoms, which are able to knock out the electrons from the outer shells. When this avalanche ionisation reaches a critical point of $10^{23}\,electrons/cm^3$, instantaneous electron plasma is formed that exerts an outward pressure on the lattice which causes modifications in the crystal lattice. We use these modifications to structure the silicon to obtain wave guiding properties that could be transformed into useful three dimensionally shaped optical components.

In the sections above, relevant techniques and physical phenomena have been discussed. Until now, wave guiding in silicon is realised via photo-lithographic technique. Although this process is well characterised, it is time consuming and has limited degrees of design freedom due to its mainly two-dimensional character. Three dimensional waveguiding via photonic structures was also discussed but until now, these photonic structures have only been realised in glass or polymers such as SU-8 and PMMA, owing to the large physical constraints imposed by the properties of silicon, see table 2.5.

2.6 Summary

The governing physics behind laser-mater interactions at ultrafast scales has been presented. As described, the principle aim to realise subsurface modification in silicon and other materials is to confine the energy in a small volume in the bulk. For this reason, the photon energy or the wavelength that is to be focussed inside silicon is chosen to be well above the main bandgap of silicon. This allows for silicon to be transparent at this wavelength ($1552\,nm$) thereby, avoiding linear absorption in the material.

With regard to material modifications in SU-8, the system chosen for it is the Photonic Professional, which comes with a $780\,nm$ fs laser. Since the system is pre-calibrated and tested for the laser properties, it is used without any major modifications. Polycarbonate and acrylic, on the other hand, do show nonlinear absorption at $1552\,nm$. Therefore, bulk modification will be performed with the same apparatus as that for silicon.

3 Experimental Set-Up, Design, and Analytic Tools

An experiment is a question which science poses to nature, and a measurement is the recording of nature's answer.

— **Max Planck**

In this chapter, the experimental set-up that was designed to induce subsurface and volume modifications in materials is discussed. The 3D lithography tool, Photonic Professional by the company Nanoscribe is also briefly discussed with a few relevant technical details. Apart from the commercially available analytical tools such as microscopes and scanning electron microscopes (SEM), a nanometre precise optical tool was developed (MONA) which will also be described in detail.

3.1 Introduction

In the previous chapter, the laser material interaction model was discussed for different materials. The feasibility of producing volume modifications in silicon and as well as polymers was analytically testified. To experimentally realise these modifications, an experimental set-up has been constructed by choosing an appropriate laser system.

Apart from discussing the experimental set-up, its parameters, and its characterisation, the software used to control the entire system is also discussed. This software, Fringe Processor, which is built in BIAS has a modular feature by means of which a plugin can be programmed to extend its features. During the course of this work, a plugin named LeNA was developed which is briefly discussed in this chapter.

Also discussed is the Photonic Professional tool, which is a two photon absorption based 3D nano lithography instrument developed by Nanoscribe GmbH. It was used to fabricate nano to micro scale optical structures in SU-8 based polymer resin. The analytical tools used during this work, are also briefly mentioned and discussed.

3.2 Comparison of laser systems

As shown in chapter 2, introducing bulk modification in silicon requires laser systems with extremely high output values. In principle, many laser systems with output of $5\,W$ or more are available but *only* in the visible light spectrum or in the micrometre range (CO_2 laser). For this reason, a considerable amount of time and effort was put in order to find the right laser to induce subsurface modification in silicon. Initial tests were conducted with free space lasers. Subsequent tests were made with fibre lasers. These possess excellent beam quality and can produce energy pulses in the μJ range. Table 3.1 shows the different lasers used and the one that was finally chosen for the purpose of this work.

Table 3.1: Comparison of Laser Systems. PE: Pulse Energy. PW: Output Power. PD: Pulse Duration. λ: Wavelength.

Manufacturer	Model	Type	λ(nm)	PE,PW	PD (fs)
Coherent	Mira	Ti:Sa	1064	$300\,nJ$ - $33\,\mu J$	< 100
Polytec	fs Laser	Ti:Sa	770	$< 50\,mW$	< 100
Menlosystems	T-Light	Fibre	1560	$120\,mW$	< 250
Raydiance	M50	Fibre	1552	$50\,\mu J$	< 800

After initial tests with these lasers, the Raydiance M50 was chosen as the laser system for this work solely based on the criteria that its repetition rate and hence the total output power was high enough to induce initial subsurface modification in silicon. As discussed further in this chapter and also in chapter 4, the versatility of this laser was used to induce volume modification in a wide variety of materials. In the following sections, the experimental set-up LeNA is described which includes the selected laser.

3.3 Laser enabled Nano-structuring Apparatus

Laser enabled Nano-structuring Apparatus (LeNA) is a three dimensional Direct Laser Writing (DLW) system developed at BIAS GmbH, as part of this thesis work. The primary components of the system consists of a high-powered femtosecond laser, motion stages and laser optics. Three dimensional micro to centimetre scale objects can be written in photosensitive materials such as glass and acrylic (PMMA) substrate and silicon, via DLW technique. The working principle of LeNA is shown in figure 3.1. The source used here is the Raydiance M 50 laser, whose details are given in appendix A.1.

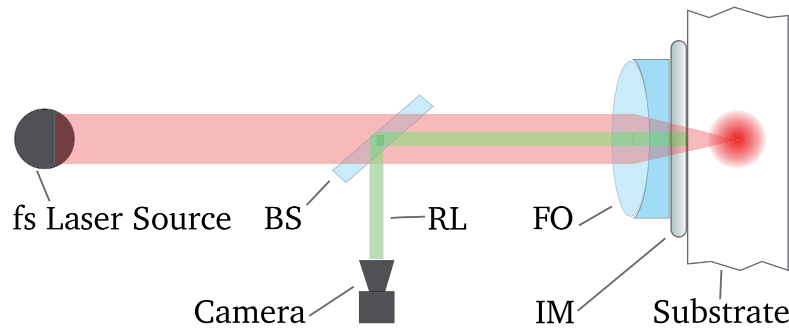

Figure 3.1: Working principle of the LeNA system. The laser beam emitted from the fs laser source passes through a beam splitter (BS) unaffected and gets focussed via the focussing optics (FO). An index matching material (IM) is used between the FO and the substrate to minimise losses via reflection and refractive index mismatch. Reflected light (RL) from the substrate, that is generated during the focussing, is reflected off via the BS and into a camera, which is then used to position the substrate in to the focus.

3.3.1 Optics and objectives

During the course of selecting the appropriate optics to focus light tightly, the initial setback was the unavailability of finding a microscope objective that was corrected for infrared ($1552\,nm$) ultrafast laser beam, since most of the microscope objective are corrected for their chromatic aberrations only in the visible light range. The use of simple focussing lens was ruled out as the required numerical aperture (NA) could not be achieved without a microscope objective. Secondly, ultrafast and high energy laser beam heats up the optics. Which means that a complex set of lenses that are held together with optical glue were easily destroyed during the focussing procedure. This meant that the use of such complex lens systems that were only suitable for visible light applications were ruled out. A numerical aperture of values > 1 is only possible with the use of oil immersion objective. Hence, the choice of objective was a commercially available microscope objective with high NA. Its parameters as shown in table 3.2. Later on, an aspherical focussing lens was purchased that was corrected for $1552\,nm$ but a smaller NA. The advantage with this lens was that it allowed the surface to be protected via a microscope cover slip, so as to protect it from possible ablation during the write procedure. Images of both these types are shown in fig 3.2.

3.3.2 Motion stages and controller

The ILS series linear stages from Newport offering $150\,mm$ travel ranges were chosen to be XY stages for LeNA. Its extruded aluminium body has been optimized to avoid bending

Table 3.2: Specifications of the focussing objectives in the LeNA system

Properties	Microscope Objective	Aspherical Lens
Design Wavelength	VIS	$1552\,nm$
Numerical Aperture	1.25	0.64
Magnification	$100x$	$40x$
Focussing medium	Oil	Air

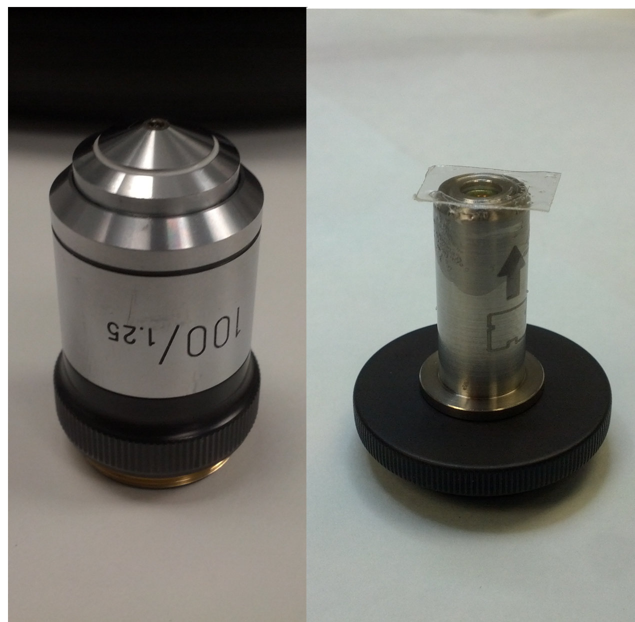

Figure 3.2: Two variants of focussing objectives used in LeNA. On the left, is a commercially available oil immersion high NA objective. On the right is a $0.64\,NA$ aspherical lens mounted on an objective thread, corrected for $1552\,nm$ and with a cover slip.

effects caused by the different thermal expansion coefficients of the aluminium body and steel rails. Their specification are given in the table 3.3. The travel range of $150\,mm$ was sufficient to fully scan an area of a $4\,in$ or $100\,cm$ wafer holder. Even with the added constraints of the holder mechanics, etc. there was enough room for the XY stages to fully scan the area of the sample/wafer.

Table 3.3: Specification Table for XY Stages - LeNA

Properties	Values
Travel Range	$150\,mm$
Resolution	$0.5\,\mu m$
Uni-directional Repeatability	$1.1\,\mu m$
Reversal Value - Hysteresis	$0.7\,\mu m$
On-Axis Accuracy	$3\,\mu m$
Maximum Speed	$100\,mm/s$
Maximum Acceleration	$250\,mm/s^2$
Pitch	$70\,\mu rad$
Yaw	$75\,\mu rad$

For the Z-axis, the VP-5ZA was chosen. It is an ultra-low profile, precision vertical translation stage ideally suited for semiconductor wafer inspection, photonics test and packaging, micro-assembly, precision metrology, and surface inspection systems. It is achieved by an inclined-plane design consisting of a unique arrangement of two wedges which move past each other via inclined, recirculating ball bearings. To avoid any side motion, the upper wedge is constrained by two pairs of vertically mounted double-row linear ball bearing slides resulting in pure vertical motion. Its specifications are given in the table 3.4. This stage offered the advantage of carefully positioning the sample within the focus of the laser beam. The travel range provided by this stage in Z direction was $4.8\,mm$ but the resolution was well under $100\,nm$ which was key to achieving 3D bulk modification in materials.

Table 3.4: Specification Table for Z Stage - LeNA

Properties	Values
Travel Range	$4.8\,mm$
Minimum Incremental Motion	$0.06\,\mu m$
Uni-directional Repeatability	$0.3\,\mu m$
Bi-directional Repeatability	$\pm 0.25\,\mu m$
On-Axis Accuracy	$\pm 1.5\,\mu m$
Maximum Speed	$5\,mm/s$
Pitch	$\pm 50\,\mu rad$
Roll	$\pm 50\,\mu rad$
Weight	$2.4\,kg$

3.3.3 User controls

To enable quick and easy hardware controls to LeNA, joysticks and buttons were used. They were bought from the company Tinkerforge, that sells these electronic components along with the so-called 'Master Brick'. This Master Brick acts as a hardware interface between the individual bricklets (joystick and buttons) and the computer. The Master Brick is connected to LeNA and the corresponding bricklets are connected to the Master Brick. Technical details are provided in appendix A.2. The laser itself comes with a set of software based user controls, whose details are mentioned in appendix A.3. The entire set-up is controlled via a unified software interface provided by Fringe Processor. During the course of this thesis, an entire plugin was developed which connected the laser to the motion stages and the hardware controls. The technical details are mentioned in appendix A.4.

3.4 Photonic Professional

The 3D-Lithography process is based on a commercial laser-lithography system of the company Nanoscribe. The system is called Photonic Professional. The schematic set-up is illustrated in figure 3.3. The radiation source for the laser writing is a femtosecond laser of the company Menlo System (see table 3.1), with an emitting wavelength of $780\,nm$, a pulse duration of $100\,fs$ and a pulse frequency of $80\,MHz$. The intensity of the laser spot is controlled by an acousto-optic modulator (AOM). The AOM consists of a transparent crystal, with a piezo crystal on one side. The created sound waves operate on the beam as a diffraction grating, whereby the position of the intensity maxima of the laser beam is influenced by the frequency. After exiting the AOM, the laser spot is focused by an oil-objective with an NA of 1.4 and a magnification of 100. This spot is focused on the sample, which is mounted on a holder and introduced by a guide rail into the piezo table. The piezo table is furthermore connected with a positioning stage. To observe the writing process, a CCD-camera is used. It is possible to illuminate the probe with a transmission and a reflection LED.

3.4.1 Sample preparation

The preparation of the cover glass starts with cleaning the glass with isopropanol. Then the glass is glued into the slots of the substrate holder with an adhesive. A drop of immersion oil is placed in the centre of the cover glass, the substrate holder is turned upside down and a drop of IP-L resist is applied to the same location as the oil drop, but on the other

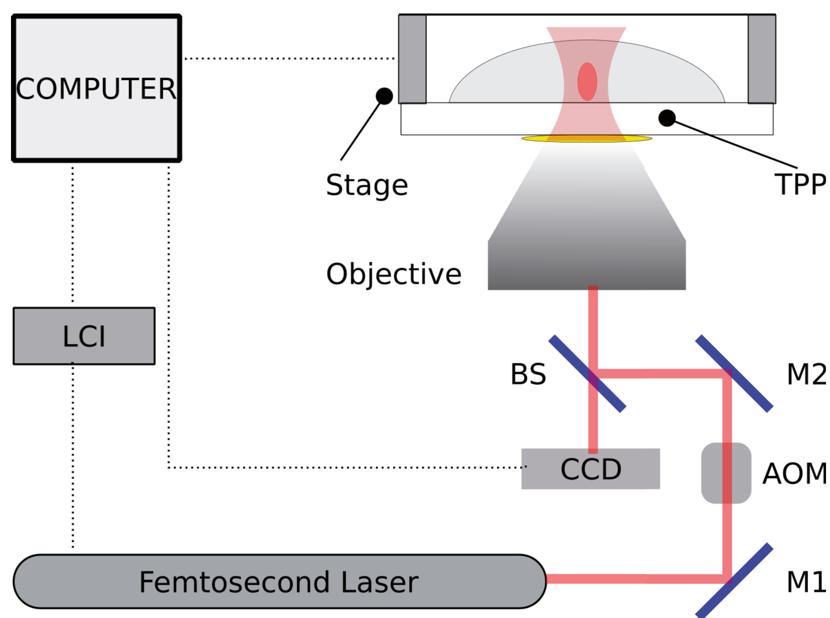

Figure 3.3: Schematic overview of the Photonic Professional System with the important components. The laser beam passes through the Acousto-Optic Modulator (AOM) and is directed onto a beam splitter (BS) . M1 and M2 are mirrors. Subsequently, the focussing is performed with a lens onto the sample, which is moved by a piezo stage. The laser beam is controlled via a Computer through the Laser Controlling Interface (LCI). The sample is focussed and aligned by imaging the reflection from its surface with a CCD. The process of Two Photon Polymerisation (TPP) is shown in detail in figure 3.4.

side of the glass. After the writing process the cover glass is immersed in a SU8-developer bath for seven minutes and afterwards in isopropanol for the same time. Finally the residues are blown off with pressurised nitrogen gas.

The waveguides are written on a $140\,\mu m$ thick borosilicate glass plate with a refractive index of 1.511. Figure 3.4 shows a schematic of the prepared glass substrate with the immersion oil and the resist. The objective is approached to the glass probe on the side of the immersion oil. The writing process is done on the other side of the glass, inside the photoresist. The location is illustrated as a dark red focus spot.

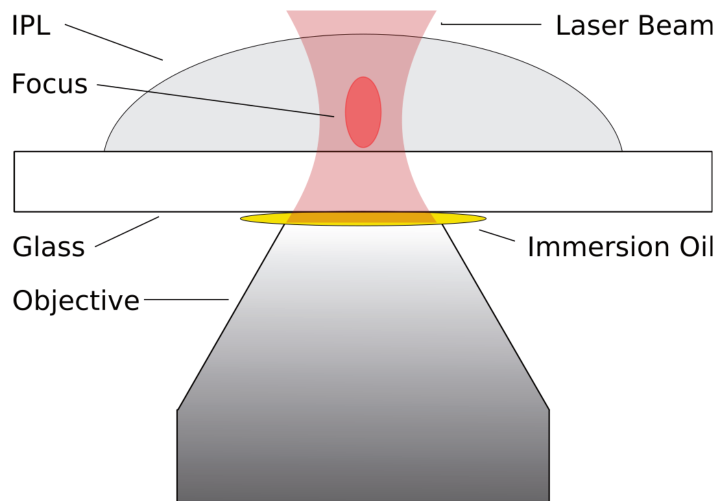

Figure 3.4: Schematic of the writing process. The laser spot is focussed on a small size in the resist (IPL) on the other side of the glass substrate, after coming in contact with the immersion oil.

3.4.2 Photoresists

In this work, the writing process is done with negative photoresists, the exposure by a focussed laser beam. This beam can write in all three dimensions and define the structure, which remains after the development as a 3D-structure. For this process, a photoresist with a large two-photon absorption cross-section and a high chemical quantum efficiency is essential.

The used photoresist is a special composition of the company Nanoscribe and Microchem, IP-L. It is liquid and has a resolution down to 150 nm. In addition, no pre - or postbake is necessary, it is drop-casting and has a good adhesion on the glass substrate. Prior to exposure it has a refractive index of 1.48.

3.5 Modular Optic Nano Analyser

Modular **O**ptic **N**ano **A**nalyser (MONA) is an optical characterisation set-up that can perform a multitude of characterisation operations. Due to its modularity, it can also be used in holography and other spectroscopic methods. We currently use it to measure the mode field diameter (MFD) and optical field distribution from the 3DPOW. It consists of an input and an output fibre based ports that are mounted on piezo-actuated nano-positioners that have a resolution of $\approx 2nm$. These are mounted on a longer range micro-positioners that have a travel range of $15mm$. Together, they form a highly resolved large area optical field scanner. The sample it mounted on a rotational stage and the entire set-up is controlled via two cameras. The MFD scanning algorithms are automated via LabView are optimized for 3DPOW. The input can be either connected to a laser diode or a white light source and the output is generally connected to a fast photoreceiver. Figure 3.5 shows MONA configured to measure the MFD of the 3D-Polymer Optical Waveguide (3DPOW).

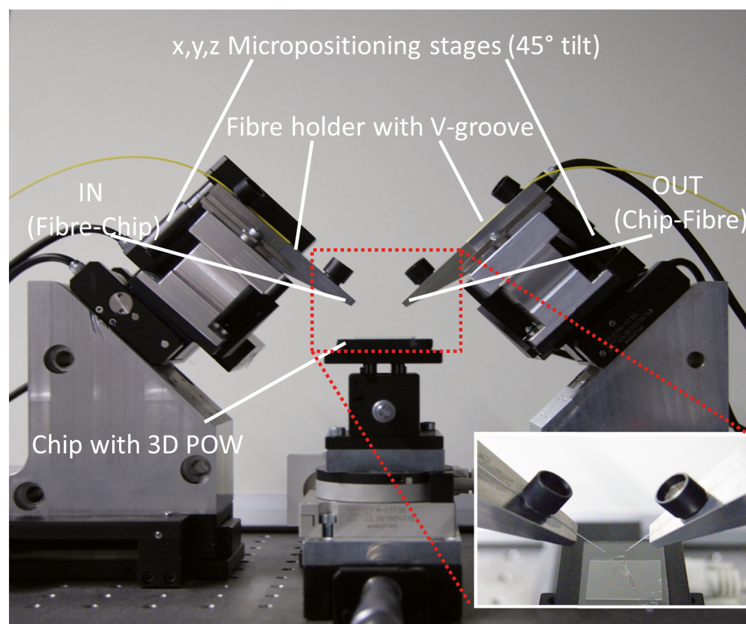

Figure 3.5: MONA: Modular Optical Nano Analyser. The high precision piezo translation stages are mounted on long range micro-positioners and are inclined at an angle of 45° to match the 3DPOW. The sample itself rests on a rotational stage. Inset: A close-up of the sample contacted with the input and output fibres. Source [96].

3.5.1 Mechanical and electro-optical components

MONA is controlled via a LabVIEW user interface. The primary hardware of MONA consists of:

1. Mechanical components: Linear translation stages, rotary stage, and nano-cubes
2. Electro-optical components: Laser diode, photodiode, fibre optics

Mechanical components

As shown in figure 3.6, at the hub of the mechanical components is the C880 controller from PI. The C-880 Automation Plat- form is a modular and highly versatile system for complex multi-axis positioning and automation tasks. It was conceived for applications relating to photonics alignment. It makes it possible to control nano-positioning systems with up to 18 axes. Servo-motors and piezo actuators / stages can be combined in almost any combination.

The command structure for the controller is based on the PI General Command Set (GCS). With GCS the development of custom application programs is simplified, because the commands for all supported devices are identical in syntax and function. However, this controller is also delivered with LabView libraries and DLLs, which makes it easier to integrate it with other devices and controllers.

There are a total of six linear translation stages in MONA that are combined into two XYZ clusters. The M111.1DG compact micro translation stage is a motorised via a DC-Servo. They feature a precision lead- screw with sub-micron resolution and precision linear ball bearings guaranteeing $< 0.5\,\mu m$ straightness of travel. The DC servo motor actuates motion via a backlash-compensated screw and nut system. It is also equipped with a high resolution encoder. The linear stages have a travel range of $15\,mm$ with the smallest incremental motion of $0.05\,\mu m$. It can reach a maximum velocity of $1.5\,mm/s$.

Each of those two XYZ clusters carry a nano-cube in them, thereby extending their resolution. The P-611 nano-cubes are a closed-loop multi-axis piezo nano-positioning system. They have a zero-friction guiding system and are equipped with low-voltage piezoelectric drives $(0 - 100\,V)$ integrated into a sophisticated flexure guiding system. The force exerted by the piezo drive pushes a multi-flexure parallelogram via an integrated motion amplifier. Integrated strain gauge position feedback sensors provide nanometre-scale resolution in closed-loop operation. They have a travel range of $100\,\mu m$ in all three directions and a resolution of $1\,nm$.

The sample is placed on a rotary stage. This allows for fine adjustments in the position of the sample and as well as in a $360°$ scan. The M-037 rotation stage is equipped with worm wheel drives providing continuous rotation in both directions. An integrated spring

pre load eliminates backlash. The worm gear ratio is $180:1$, corresponding to a turntable rotation of $2°$ per revolution of the drive shaft. Coarse position can be read from an adjustable scale ring on the outer edge of the turntable graduated in 2 degree increments and a drive shaft mounted indicator with 0.1 degree graduations. The smallest possible rotation that can be made is $3.5\mu rad$ with a maximum rotational velocity of $6rad/s$.

Electro-optical components

The two major electro-optical components are the laser diode and the photodiode. They are controlled via the Thorlabs Pro8000 controller. It allows for a variety of photonic components to be connected and measured. The connection to the controller can either be via ethernet or via RS-232 interface. The laser diode used was a $655nm$ variant mounted on a Thorlabs LDM21 temperature controlled laser diode mount. It has a built in thermo-electric cooler to regulate the temperature of a standard $9mm$ packaged laser diode. The photodiode used in MONA was the SM05PD1B type, also from Thorlabs. It is a large area silicon photodiode and is sensitive between $350-1100nm$ which is well within the range of the laser diode and most photonic applications. With a rise and fall time of $10ns$, high speed scans with this module is possible. An overview of the components is shown in figure 3.6.

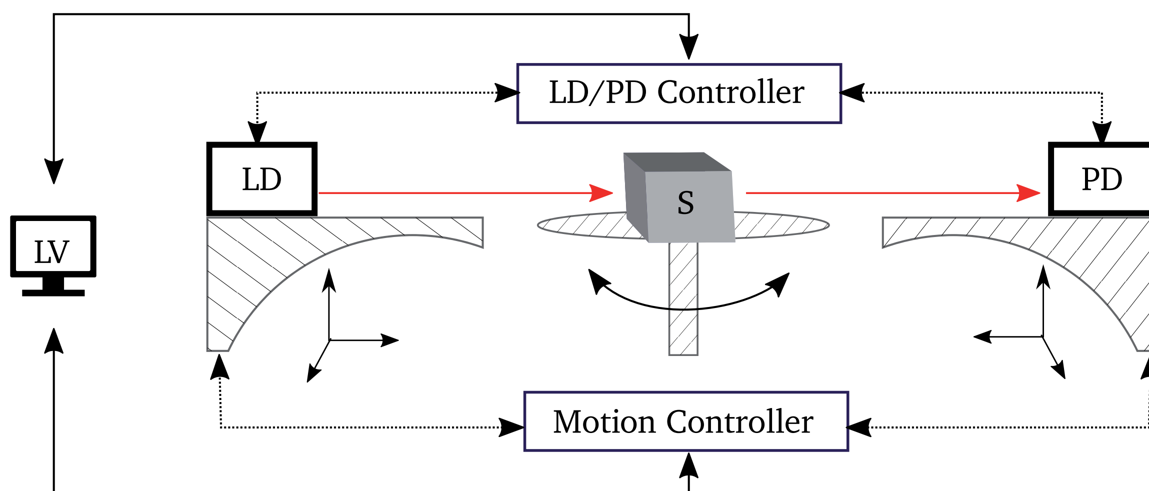

Figure 3.6: MONA: Modular Optical Nano Analyser. A sample (S) is placed on a height adjustable and rotary table. A fibre coupled laser diode (LD) is used as a source that is fixed on to a three dimensional stage set-up. A similar set-up carries the photodiode which is used to read out the transmission/reflection signals from the sample. The stages are controlled by an automated motion controller C880. The LD and the PD are controlled by the Pro 8000 controller. The measurement is carried out by reading out the signals via a LabVIEW (LV) user interface.

3.6 Scanning Electron Microscope and Focussed Ion Beam

A Zeiss Gemini model scanning electron microscope (SEM) was employed to obtain high resolution micro graphs of silicon samples. To study the samples, the wafers were cut along the fracture plane. The top surface and the cut-plane were imaged using this SEM. Depending on the sample orientation, the signals were either read out via the secondary electron (SE) sensor or the back scattered electrons (BSE) sensor, to obtain maximum contrast and image detail.

The SEM was upgraded with a focussed ion beam (FIB) via the Zeiss Crossbeam upgrade, see figure 3.7. The FIB was primarily used to etch through the surface of silicon and detect the presence of subsurface modifications and their influence on the etching process.

With the upgrade, see figure 3.7, the imaging capabilities of the system was greatly enhanced. Equipped with an electron Schottky emitter gun, imaging resolutions of $1.9nm$ at $1kV$ and $1.0nm$ at $15kV$ could be achieved. The FIB was Gallium based Liquid metal ion source (LMIS) which has a resolution of less than $3nm$. The system is fitted with an

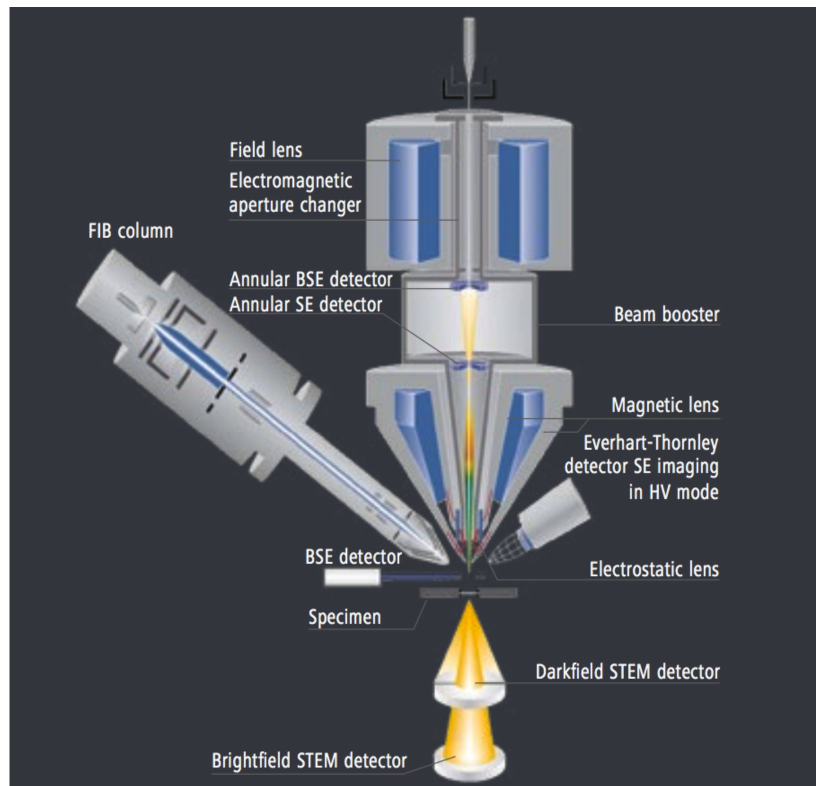

Figure 3.7: Arrangement of FIB and SEM column in Crossbeam systems with an inclination angle of 54°. The Scanning Transmission Electron Microscopy (STEM) detector can only be used to detect signals in case of samples with thickness less than a few hundred nanometres. Source: Product Information Sheet (Version 1.0) for Zeiss Crossbeam 340 from Zeiss.com

Inlens Duo Detector for Secondary Electrons (SE) and Energy selective Backscattered (EsB) imaging. For the FIB, a multi-gas injection system (GIS) is also installed.

The SEM was primarily used as a analytical tool whereas the FIB was also used to further alter the structures in silicon and polymers. The etching via FIB allows for a fine resolution of upto 10 nm but only in 2.5 dimensions, which means that true 3D structuring in FIB isn't feasible. On the other hand, structuring via photonic professional (sec. 3.4), yields real 3D structures but with a maximum resolution of 100 nm in the axis of writing.

3.7 Optical and infrared microscopes

To detect subsurface modifications in silicon, a Müller Optronics Laboratory Microscope was used. Although traditionally used for biological specimen, this microscope enabled two modes of operation: transmissive and reflective. The microscope was equipped with a halogen light bulb and a neutral density filter. When used in the transmissive mode the filter was removed and a camera was mounted on the microscope. The camera used was a Thorlabs DCC1545M CMOS type monochrome camera. It has 1280×1024 pixels and a frame rate of 25 fps. An infrared glass filter that was fixed in the front of the sensor was removed. This allowed for wavelength $> 900 nm$ to hit the sensor. The major challenge with this imaging technique was that both the sample and the camera sensor were made of silicon; which means that there is a very narrow band-gap around $1100 nm$ where silicon is semi-transparent and the sensor (also silicon) detects the incoming light and is able to image the bulk modifications.

During the tests, the sample was imaged in reflective and the transmissive mode for the same test area. This allowed for subsurface modifications to be detected and to distinguish between damages and modifications on and below the surface. For subsurface damages, the bright and dark field illuminations showed similar results. Another major challenge for this method is the use of microscope objectives that are corrected only for the visible light spectrum. This means that the chromatic aberrations that occur for longer wavelengths go uncorrected and provide a below-average blurry image. For this reason, even though subsurface modifications could be detected, further analysis with this system was limited.

Figure 3.8: An image of a laboratory optical microscope. A halogen light bulb is situated at the base of the microscope that provides a broadband illumination to the sample. This is used to obtain transmission images in silicon by removing the neutral density filter. A camera is attached to the top to capture the infrared images.

3.8 Summary

The experimental Laser enabled Nano-structuring Apparatus (LeNA) was developed as a fully functional and semi-automated 3D Direct Laser Writing apparatus. It is capable of aligning and positioning samples over a range of $150\,mm$ with $500\,nm$ accuracy in the xy direction. The sample is mounted on an automated translation axes set-up and can move in all three directions. In the z direction, the translation stage is much finer and has a resolution of $< 100\,nm$ with a travel range of $4.8\,mm$. This fine adjustment is necessary to accurately position the focus inside or on the surface of the sample, as required. The samples are written with a wavelength of $1552\,nm$ with variable repetition rate and pulse energies. The repetition rate can be adjusted between $1\,Hz - 100\,kHz$ and independent of the pulse energy which can be adjusted between $5 - 50\,\mu J$. With a pulse width of $800\,fs$, LeNA can be used to inscribe confined and highly accurate micro to nano structures within the bulk of optically transparent materials. The system requires the input of a '.yal' file (see appendix B) to transfer the required structure into the sample.

Photonic Professional from Nanoscribe was used to developed micro structures for opto and opto-electronic applications. These structures are fabricated via 3D Lithography as compared to LeNA which is 3D Direct Laser Writing. They are essential in micro-optical and nano-optical applications such that are described in chapter 5.

The Modular Optic Nano Analyser (MONA) is an analytical tool that is used mainly to scan the optical mode fields of micro structures. It can also be used to image micro structures at high resolutions. Its translation stages that have a resolution of $< 50\,nm$ are also fitted with piezo-actuated nano-cubes. These nano-cubes have a resolution of $1\,nm$. Together with the translation stages, MONA is capable of scanning over $15\,mm$ with an accuracy of a nanometre. The samples are analysed via various destructive and non-destructive methods. The non-destructive methods include optical and infrared microscopy. Electron microscopy involves treating the sample with a layer of gold or some reflective surface to enhance the contrast. Inside the FIB, the sample is cut or 'destroyed' during analysis.

4 Subsurface Modification in Silicon and SU-8

The most exciting phrase to hear in science, the one that heralds the most discoveries, is not 'Eureka!' but 'That's funny...'

— **Isaac Asimov**

In this chapter, the experimental results of subsurface and bulk modifications in silicon and SU-8 will be discussed. LeNA, a custom built 3D Direct Laser Writing apparatus, introduced in the previous chapter, was used to realise subsurface modification in silicon. A few simulation results of silicon based waveguides are also presented. Photonic Professional by Nanoscribe was used to realise 3D optically relevant structures in SU-8. Further characterisation of these samples via SEM and MONA is also presented.

4.1 Material modification in silicon

Based on the data from chapters 2 and 3, a laser system is used that has a centre wavelength of $1552\,nm$, a pulse duration of $800\,fs$, a pulse energy of $50\,\mu J$ and a maximum repetition rate of $100\,kHz$.

Figure 4.1a shows the experimental set-up. The laser beam is focussed using an oil immersion microscope objective with an N.A. of 1.25. Figure 4.1b shows the principal working area of the experiment where the focus of the laser beam is driven into the bulk of silicon to realise subsurface modifications. The position of the focus spot is monitored by the back reflection of the laser beam from silicon that is sampled into a camera. When positioned, the motion stages carrying the wafer is activated. Figure 4.1c schematically shows the subsurface pattern in a silicon wafer.

4.1.1 Infrared imaging of subsurface modifications

Figure 4.2a and 4.2b show visible and infra red light images, respectively, of the structures written via this process. The two images reveal the buried structures in silicon with

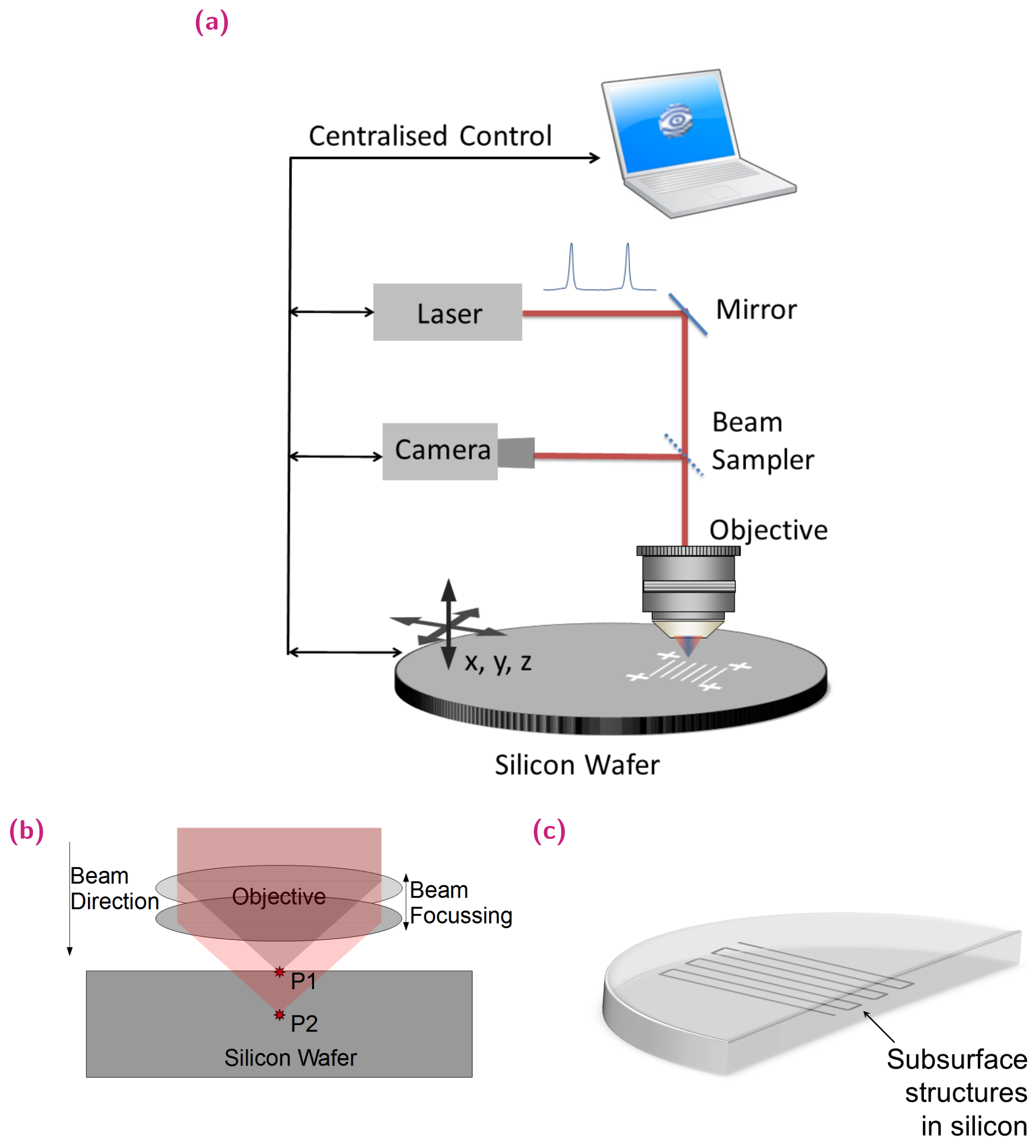

Figure 4.1: (a) Experimental set-up: The laser beam is focussed into the silicon wafer with an objective. The motion stages are programmed to drive the wafer into the laser focus spot and to move in a pre-defined pattern to create the desired structures. The camera is used to control the position of the focus. A silicon wafer with a thickness of 200 μm is used so that it is easier to make the transmission light images after writing the structures as displayed in figure 4.2b. (b) Schematic of the focussing mechanism of the set-up shown in (a). P1 and P2 are the positions on the wafer and inside the wafer, respectively. As the beam is focussed into the wafer, structures are created at the depth of P2 within the wafer. These are imaged using an IR microscope. (c) Schematic representation of the structures written in silicon. Source [66].

accompanying surface structures attributed to shock waves in some regions on the surface. The width of the buried structures as measured by a $40x$ objective is around $5\,\mu$m. For the writing process, the refractive index of the index matching liquid is 1.4917. The experiment was performed with a pulse energy of $50\,\mu$J. Also, as argued in the previous section and from the directional dependency of the mechanical stresses in silicon was observed in our experiments. The wafer used was (100) oriented, highly doped silicon with a resistivity of $5-50\,\Omega$cm that showed traces of subsurface modification, also shown in figure 4.2b.

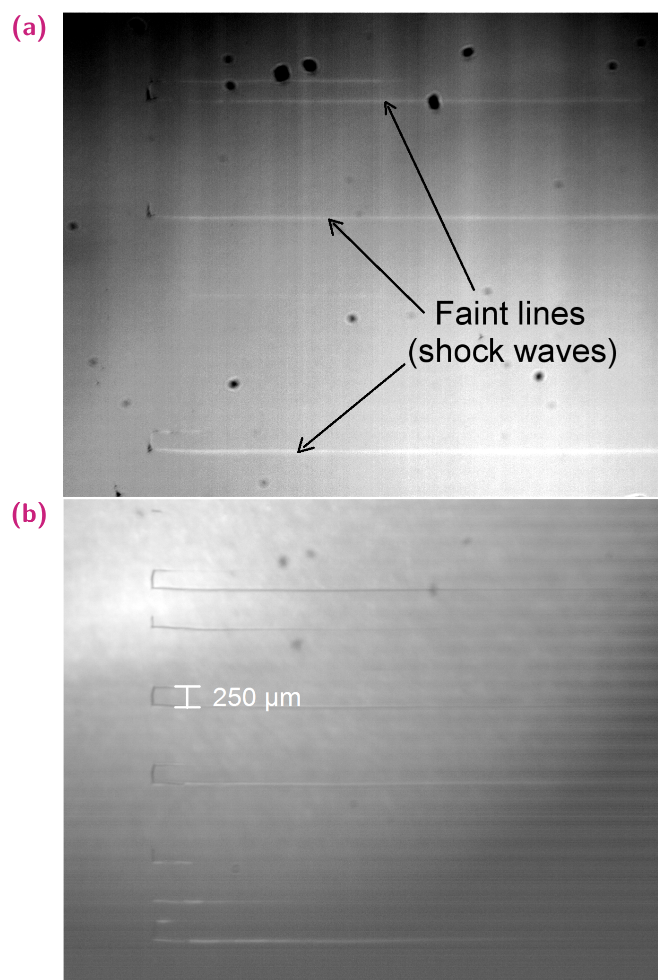

Figure 4.2: (a) Contrast enhanced visible light image, taken from the surface facing the laser beam. A few faint lines can be seen which appear to be shock waves that have travelled from the bulk to the surface. (b) An infrared image of the same section reveals buried lines within the bulk of the silicon with a width of $\approx 5\,\mu m$. The neighbouring lines are $\approx 250\,\mu m$ apart. Source [66].

4.1.2 Diffraction tests with infrared laser source

Figure 4.3 shows results of experiments performed with an optical grating with a line spacing of 25 μm. The structures are written using the procedure described in figure 4.1. When these structures are observed under a visible light microscope, the surface shows irregularities as shown in figure 4.3a presumably caused by shock waves travelling to the surface. However, a surface scan reveals no periodicity in the roughness pattern. The height of the roughness is of the order of 200 nm. The possible modifications of the material due to the processing described here is a subject of further investigation.

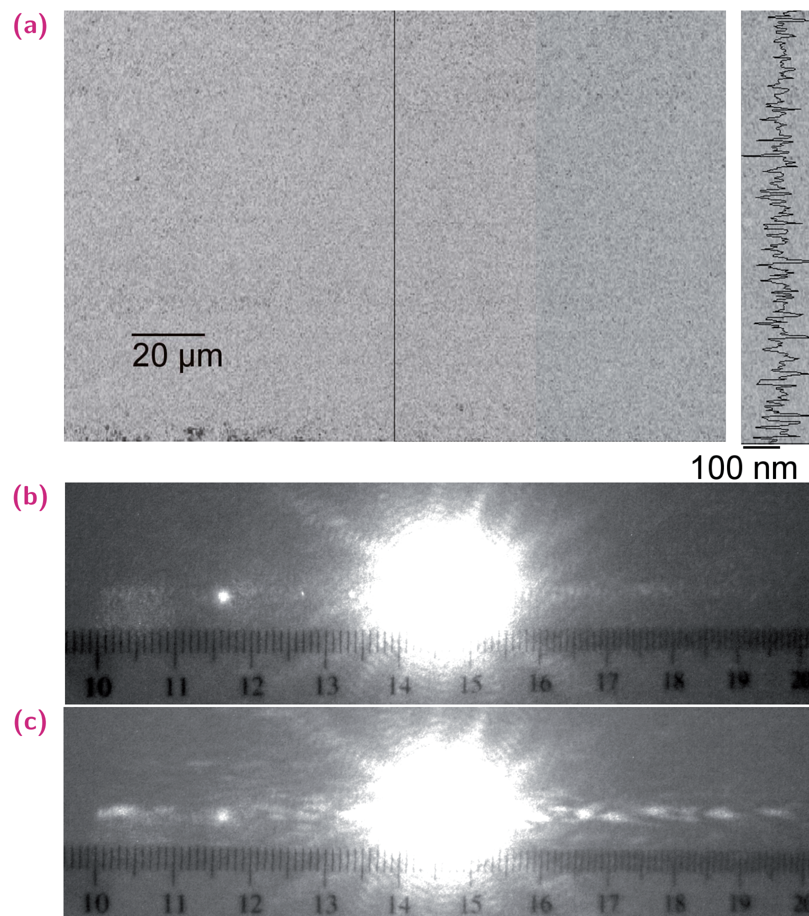

Figure 4.3: (a) Silicon surface after subsurface modification. Right: Height profile as measured along the black line, close to the centre of the picture. The height variation is ~200 nm. (b) An image of laser light with a wavelength of 1064 nm passing through the unmodified single crystal silicon. The bright spot of the left side of the beam is an artefact of the imaging lens and must be ignored. (c) Diffraction pattern observed due to the subsurface modifications. These modifications arise from the diffraction grating, as show in figure 4.1c with a spacing of 25 μm. A cm scale shows the dimensions of the pattern.

The structures were illuminated using a $1064\,nm$ light of a CW laser and a diffraction pattern is achieved which is projected at a distance of $56\,cm$ from the wafer surface. Figure

4.3b shows the un-diffracted light without the subsurface modifications, so as to visualise the differences from figure 4.3c showing the diffracted light through the subsurface modifications. By ignoring an artefact of the imaging lens on the left hand side of the zeroth order, we use the right hand side of the pattern shown in figure 4.3c to extract the intensities of the diffraction peaks as shown in figure 4.4.

The diffraction pattern consists of major and minor peaks as shown in figure 4.4. The positions of the major peaks up to the third order agrees with the theory of diffraction to a large extent. This goes on to prove the assumption that the subsurface modifications are indeed diffracting the incoming light as the on-surface modifications do not show any kind of repetitive pattern, from figure 4.3a.

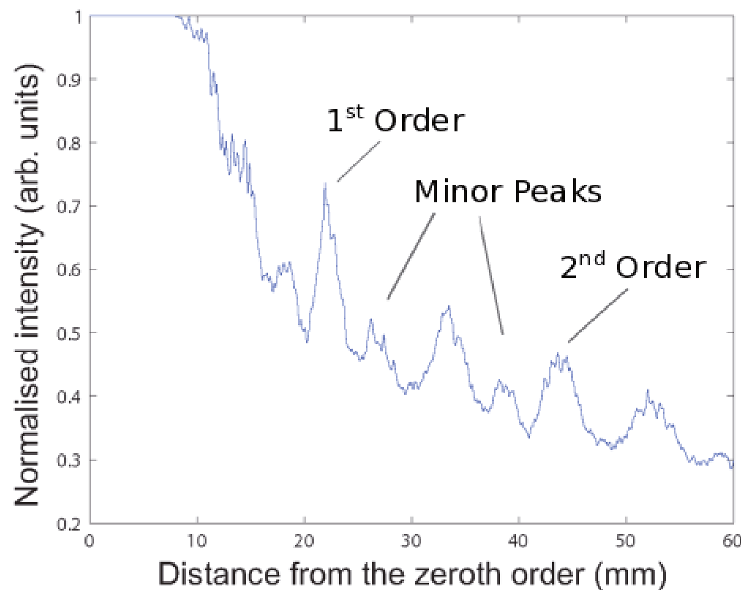

Figure 4.4: Plot of the diffraction peak intensity against the distance of these peaks to the right from the central maxima, corresponding to figure 4.3c. The position of the major peaks corresponding to the first and second diffraction orders have been analysed quantitatively in table 4.1. The positions and shapes of minor peaks is a subject of further investigation.

A diffraction pattern of an object or a source is an image of itself in the frequency space. Mathematically, it is the representation of the object in the Fourier space. Therefore, in the Fraunhofer diffraction, the diffraction pattern from square aperture will be a $sinc^2$ function and from a circular aperture will be Bessel function of the first kind. In the case of a grating, the diffraction pattern will be a Fourier transform of a function $g(x)$, that is a

convolution of a shape function $p(x)$ and a Dirac comb function $w(x)$. It can be shown as,

$$F\{g(x)\} = F\{w(x) * p(x)\} \tag{4.1}$$

For a grating with periodicity P,

$$w(x) = \sum_n \delta(x - nP) \tag{4.2}$$

The function $p(x)$, in ideal cases, can be represented as a rectangular function. But, in our case, the exact shape of the subsurface modifications is unknown. Assuming them to be lines of infinitesimally small width, we can arrive on an approximated expression for diffraction through a periodic structure, which is given by

$$m\lambda = dsin\theta \tag{4.3}$$

Where m is the order of diffraction, d is the spacing between the periodic structures, λ is the wavelength of the light, and θ is the angle between the zeroth and mth order of diffraction. For the case, as shown in figure 4.4, $\lambda = 1064\,nm$ and $d = 25\,\mu m$. The position of the peaks is in agreement with the theory of diffraction, as shown in table 4.1. The distance from the object to the zeroth peak is $560\,mm$. The error percentage between the positions of the calculated and measured values is approx. $10\,\%$, which is well within the acceptable range for an initial test.

Table 4.1: Analysis of the first two major diffraction peaks of a subsurface grating structure from figure 4.4 calculated using equation 4.3, using $\lambda = 1064\,nm$ and $d = 25\,\mu m$.

m	θ (degrees)	Peak Position (mm)		Error (%)
		Calculated	Measured	
1	2.4392	23.8551	21	11.96
2	4.8829	47.8407	43	10.11

The current understanding and explanation for the minor peaks and possible displacement or merging of major peaks (between the marked minor peaks in figure 4.4) is that the subsurface modifications are extended structures. The form and geometry of the modifications is yet to be studied in detail. One way to go about it is to fully optically characterise the subsurface modifications and include the form factor in a general diffraction equation. The other way is to calculate back the geometry using the transfer matrix method that may

yield the complete geometry of the subsurface structures [97]. These methods, however, are beyond the scope of this thesis and are hence suggested as future work.

4.1.3 Effect of pulse energy variation

To determine the effect of pulse energy on the subsurface modifications, a test was performed to vary the energy from $5-25\,\mu J$ The pulse rate of the laser was set at $100\,kHz$. A test structure was designed to write a line that would stop at every $100\,\mu m$ while travelling at $5\,mm/s$. This was to determine and amplify the effect of acceleration and deceleration on subsurface modifications. This method of stop-and-go also proved to be more effective in creating subsurface modifications as compared to writing lines with no change in velocities. The resulting structures were imaged with an infrared microscope. A consolidated image is shown in figure 4.5. At $5\,\mu J$, the width of the line was $\approx 6\mu m$ and at all other energies the width remained at an constant average of $\approx 10\mu m$.

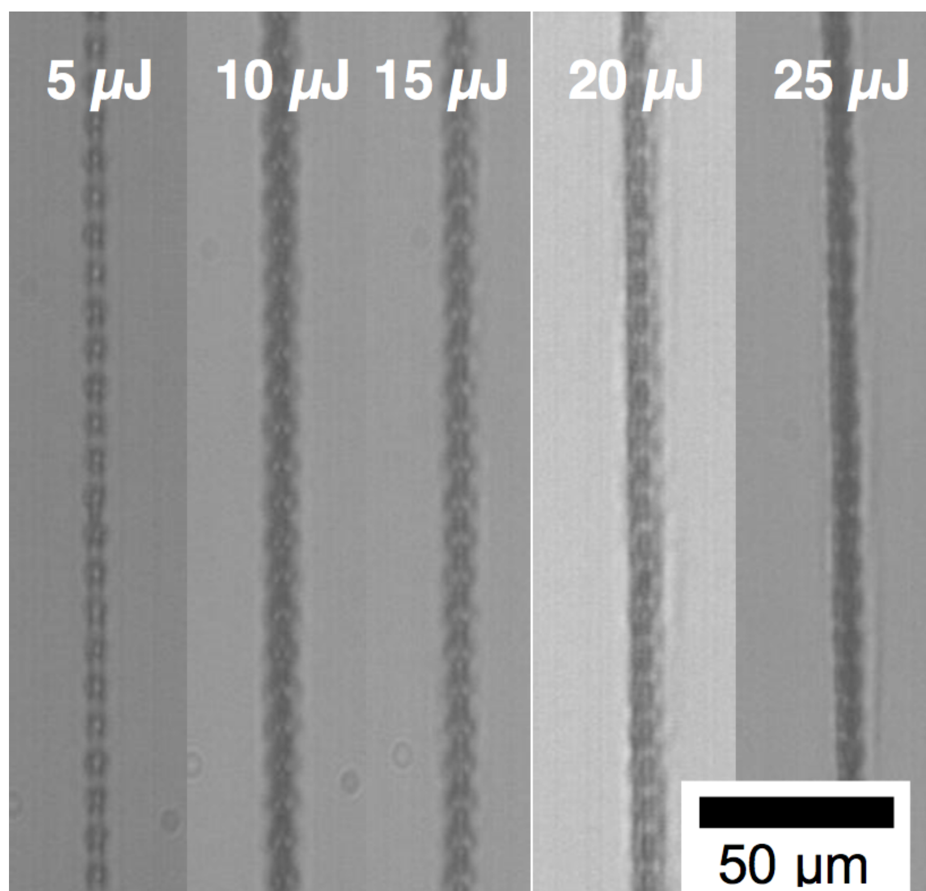

Figure 4.5: Assembly of five written lines with different laser pulse energies. The line on the left hand side is relatively faint with intensive sections where the stages interrupted. The right hand side line, which was written with five times higher pulse energy, is much more pronounced.

4.1.4 Scanning Electron Microscope (SEM) and Focussed Ion Beam (FIB) Analysis

Samples were tested in a SEM to detect and characterise the modifications. Initial preparation included coating the sample with a thin film of gold to enhance the contrast. The sample were cut along the cleavage plane of silicon, to expose the underlying subsurface modification in the cross section of the sample. Figures 4.6 and 4.7 are examples of two such samples. Since the sample was written with periodic lines separated by $100\,\mu m$, the subsurface modifications can be correspondingly found underneath the lines. Also, it can be seen that the subsurface modifications are almost likely to be accompanied with surface shock waves. These shock waves extend away from the surface and not form a crevice - as would be in the case of an ablation. The shock waves emanating from the point of focus inside the material is a result of a slight expansion of the lattice which travels to the surface, where the potential energy is the lowest.

When the sample is etched via FIB, an interesting phenomena called the curtaining effect begins to appear. The position of etching was specifically chosen to overlap half the area of a subsurface modification and half untreated monocrystalline silicon, as seen in figure 4.8. The FIB was used to etch a trapezoid shaped structure on the surface of the silicon sample with varying etching rates. This allows for a sloped and angled etch area. At the edge of the etch wall, which is about $15\,\mu m$ deep, the curtaining effect can be seen, see figure 4.8. The effects comes into effect when a tiny defect on the surface travels down during the etching process. This image reinforces the theory that the surface aberrations during subsurface modifications are due to shock waves are not laser ablations.

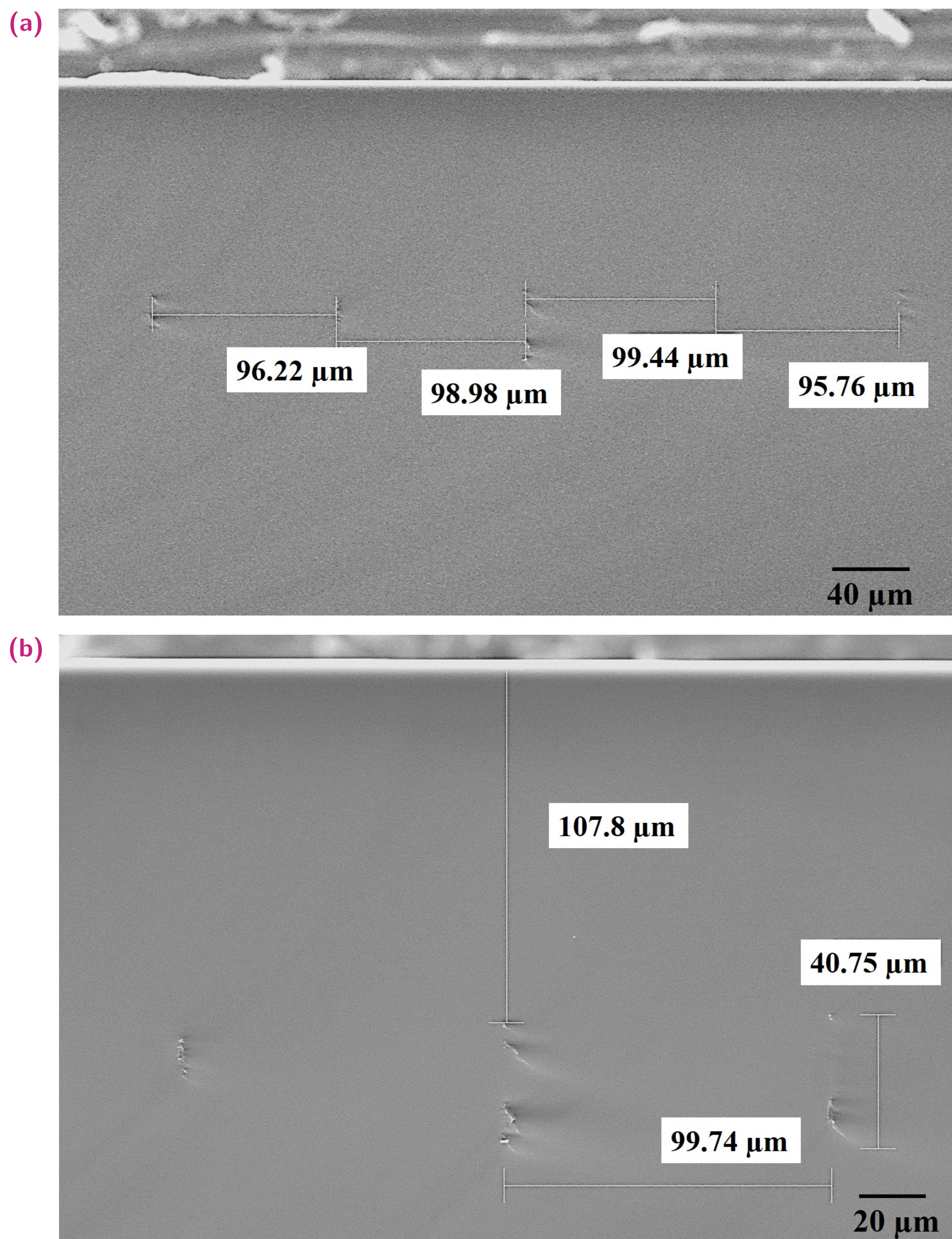

Figure 4.6: Cross sectional SEM images of silicon subsurface modifications. (a) The modifications are spaced out at approx. $100\mu m$. The design of the lines is similar to those depicted in figure 4.2b. (b) The modification occur at a depth of around $100\,\mu m$ below the surface.

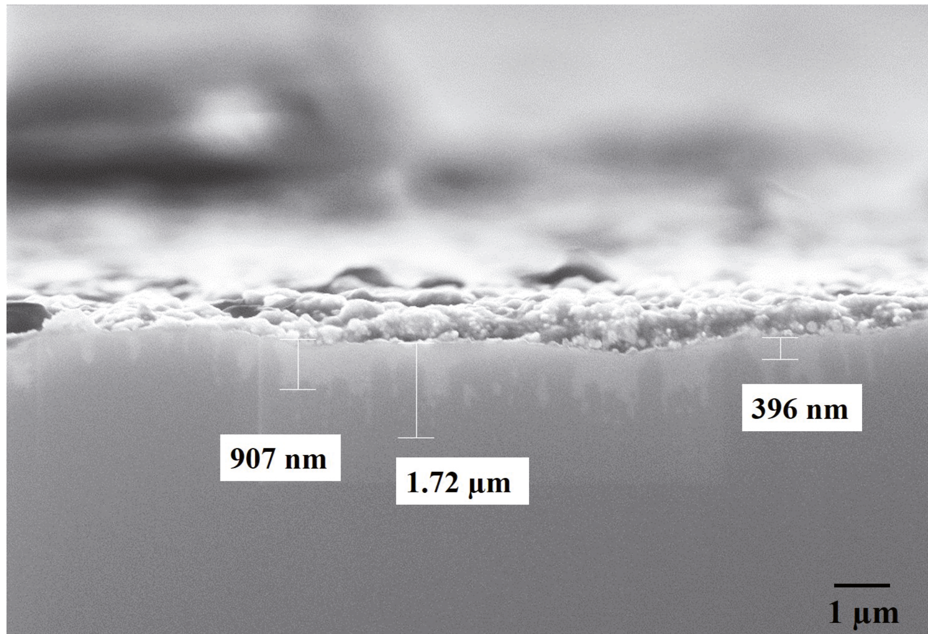

Figure 4.7: A SEM image of a cross section of silicon wafer containing subsurface modifications. The modifications can be seen at depths ranging from a few hundred nanometres to a couple of microns. The shock waves on the surface can also be seen.

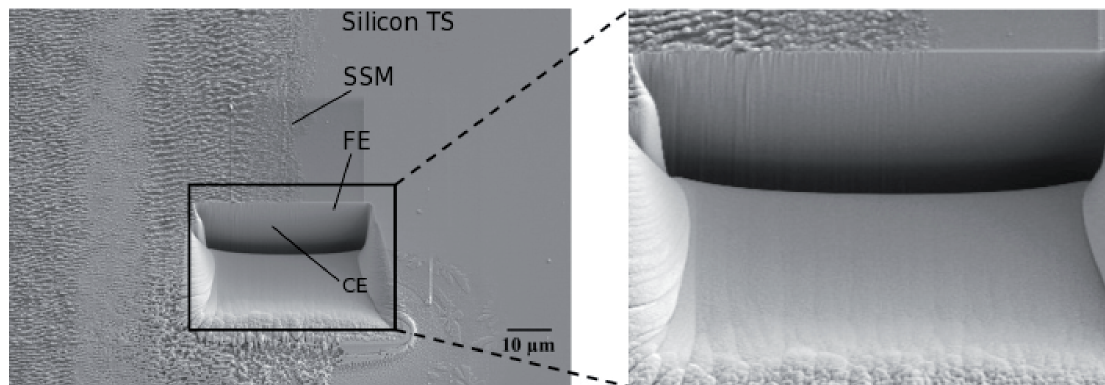

Figure 4.8: A SEM image of 100 silicon top surface (Silicon TS) with subsurface modification (SSM). The surface has been etched using Focussed Ion Beam. Curtaining effects (CE) arising from the irregularities on the surface are seen in the bulk in the FIB etched (FE) section of the substrate. However, there exists no damage upto a depth of around $15\mu m$.

4.1.5 Defect etching with Potassium Hydroxide

Heated Potassium Hydroxide (KOH) solutions can be used for preferential etching of silicon along crystal planes. The etch rate will depend on the doping and crystal orientation of the silicon and the type of KOH solution used, but is typically on the order of about a micron per minute. A typical (100) surface morphology of KOH etched silicon builds up from shallow pits. For a 100 surface, 40% KOH solution heated to $80°C$ will etch away about $60\,\mu m$ of silicon per hour. In the figure 4.9, the difference between pure single crystalline silicon and subsurface modified single crystalline silicon can be seen via KOH etch.

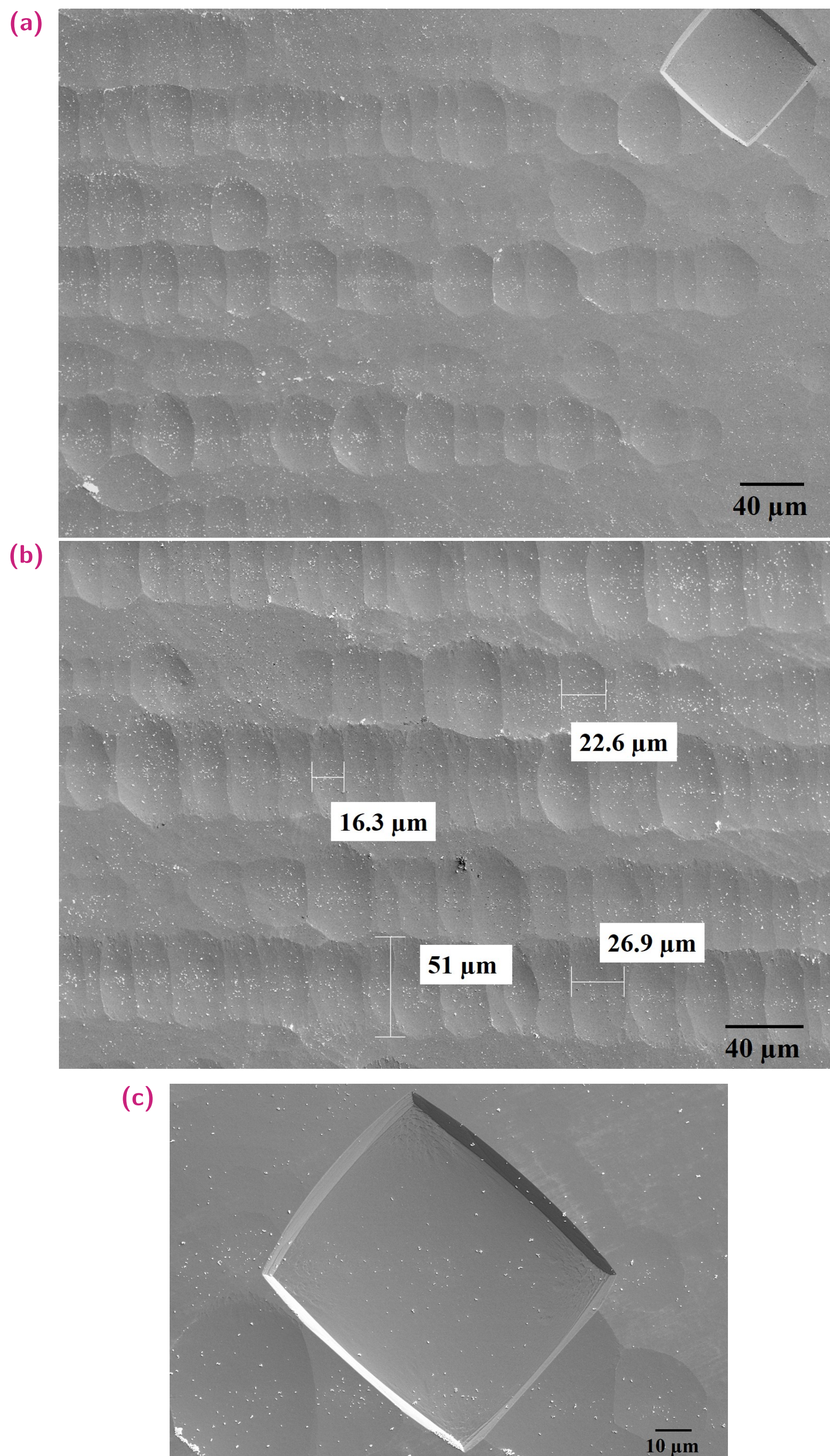

Figure 4.9: (a) A 40% KOH etched surface of 100 silicon surface containing subsurface structures. (b) Enlarged view of the hexagonal structures formed on the surface signifying subsurface modifications. (c) Enlarged view of a typical square etch profile of the 100 surface.

4.1.6 Simulation results of waveguides in silicon

The principle reason behind the subsurface modifications in silicon, as mentioned in chapter 1 is to realise buried optical interconnects that can be used to fabricate complex hybrid silicon CMOS technology based opto-electronic structures. These optical interconnects require wave guiding structures. For this purpose, index guiding is usually performed by using planar structures on silicon. The guiding mechanism is based on the total internal reflection of light at the interface between media of high and low refractive indices. For wave guiding in silicon, the refractive index of the cladding or surrounding material n_{cl} or the effective refractive index n_{eff} , e.g. of a photonic crystal surrounding the silicon must be lower than the refractive index n_{Si} of silicon. In addition, the absorption of the wavelength employed must be sufficiently low in silicon to allow transmission over the desired distances.

As follows from the discussion above, wave guiding can be realised either by

1. Creating a region of high index material in the bulk of a material with lower refractive index by modifying the material itself, or by
2. Creating regions of low index of refraction that encapsulate a region of high refractive index that serves as a waveguide

In the latter case, a photonic crystal is formed around the core of the wave guide. Figure 4.10 shows a basic structure of these three methods designed by using CST Studio suite. The structures demonstrate the idea of forming waveguides in silicon directly without any photo lithographic process and with three dimensional design capabilities. Until now, we have been able to modify the bulk of silicon and it is yet to be fully optically characterised. The modified region may consist of (nano) voids, amorphous or nano crystalline silicon or a mixed phase of these. In order to obtain a first idea of its behaviour we took the refractive index dispersion of amorphous silicon (a-Si) with 3.48 ($1550\,nm$) and simulated a waveguide structure as the one shown in figure 4.10a.

Figure 4.11a shows the E-field distribution in an a-Si waveguide of a structure corresponding to figure 4.10a. One can clearly see the rather tight confinements of modes here, despite a small difference in the refractive indices of a-Si and c-Si. Figure 4.11b shows a simulation of the transmission losses for wavelengths from $900 - 2000\,nm$. After further experimental characterization, the model will be optimised to minimise losses. The properties of a-Si and c-Si were taken into account and the characteristic absorption and transmission regions can also be clearly seen in figure 4.11b. For wavelength below 1200 nm the absorption of the evanescent field in the c-Si sets in. Below $960\,nm$ the absorption of the a-Si core starts. This behaviour results from a fit of the dispersion curve,

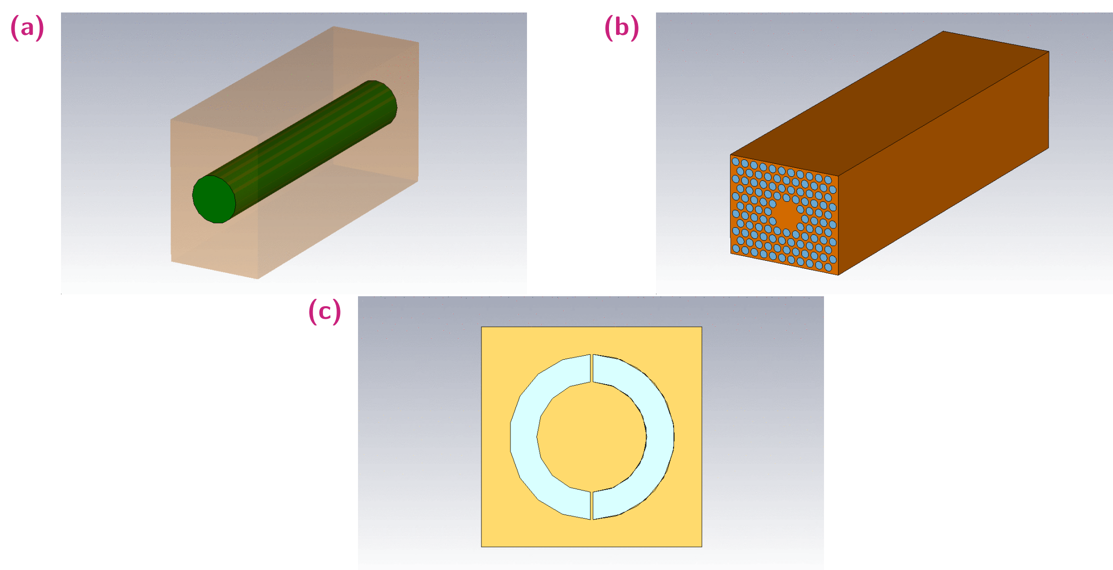

Figure 4.10: Waveguides with length $15\,\mu m$ and $2\,\mu m$ diameter. (a) Wave guiding region inside the bulk of crystalline silicon. The refractive index of this wave-guiding region is 3.48 (optimised for $1550\,nm$). (b) Silicon photonic crystal structure used as a waveguide. The cylinders have a diameter of $387.5\ nm$ and a spacing of $111.4\ nm$, so the lattice constant is designed to be the half of the telecommunication wavelength ($1550\ nm$) with respect to the refractive index difference of the materials. A waveguide of $1.5\ \mu m$ diameter is formed by 7 missing voids, which has the same refractive index as the surrounding bulk silicon. (c) Front face of a waveguiding structure formed by surrounding c-Si with voids in a semicircle shape.

which is necessary for the simulation process over a wide spectral range. As a consequence, absorption in the range of $\lambda > 1100nm$ is overestimated in this simulation.

Figure 4.12 shows the transmission characteristics of a photonic crystal based waveguide as shown in figure 4.10b. It represents a hexagonal pattern of air holes, where the central holes are missing. These missing voids have the same refractive index as the surrounding bulk Si. The region around it is however modified to have a lower refractive index – in our case, we considered it as 1. The waveguide has a length of $15\mu m$ and an effective diameter of $1.5\mu m$. Figure 4.12a clearly shows the tight confinement of the E-field in the waveguide due to a large difference in the refractive indices of silicon and vacuum (air). Figure 4.12b shows the calculated transmission properties of this model. At a wavelength of $1550nm$, the losses are around $0.4dB$ for $15\mu m$ long waveguide. For photonic crystals the transmission not only depends on the material properties but also strongly depends on the ratio of wavelength to model geometry.

Figure 4.13 shows the transmission characteristics of a c-Si waveguide surrounded by large voids with a refractive index of 1 (vacuum). This waveguide is $15\mu m$ in length and $2\mu m$ in diameter. Figures 4.13a and 4.13b show tightly confined E-field and the transmission properties, respectively. A loss of around $0.4dB$ is found for this waveguide at $1550nm$.

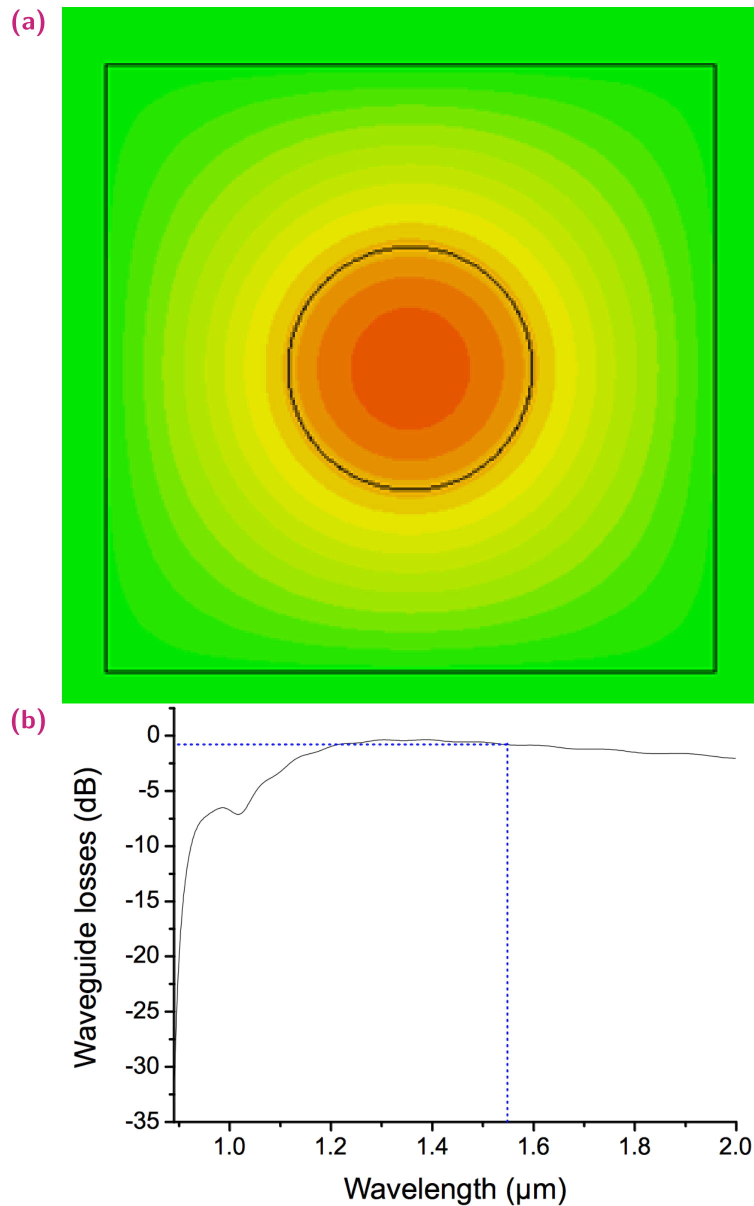

Figure 4.11: Transmission characteristics of the amorphous silicon waveguide model shown in figure 4.10a. (a) E-field distribution in a simulated a-Si waveguide of $15\,\mu m$ length and $2\,\mu m$ diameter. (b) Transmission properties of waveguide as function of wavelength, $1\,dB$ loss at $1550\,nm$.

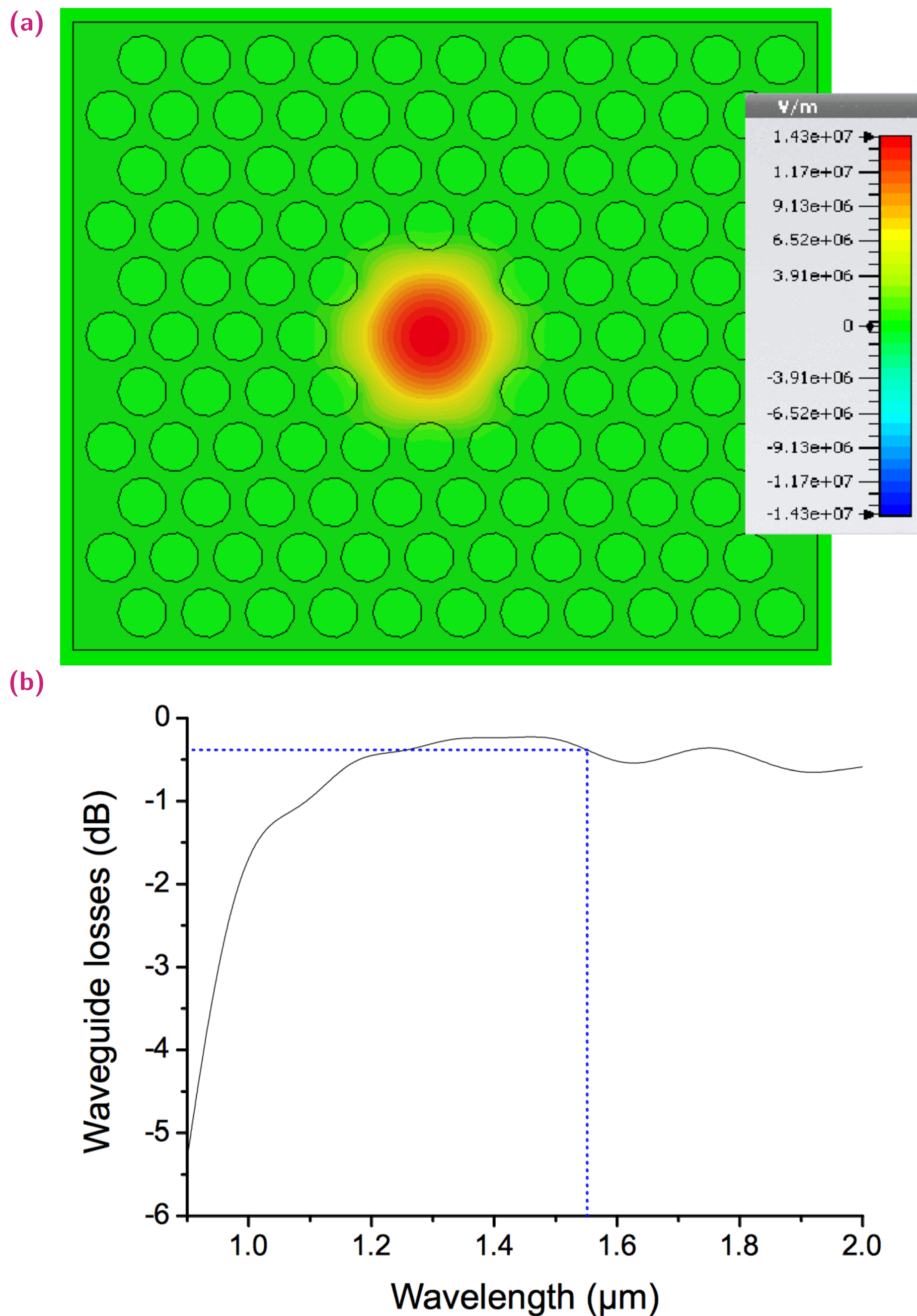

Figure 4.12: Transmission characteristics of the photonic crystal waveguide model shown in figure 4.10b. (a) E-field distribution at the output port of a photonic crystal waveguide with an effective $15\mu m$ length and $2\mu m$ diameter. The modes are strongly confined to the waveguide and do not leak into the neighbouring region. (b) Transmission curve of the photonic crystal waveguide shows losses of around $0.4dB$ at $1550nm$. The curve plateaus after 1200 nm as silicon is almost transparent beyond this wavelength.

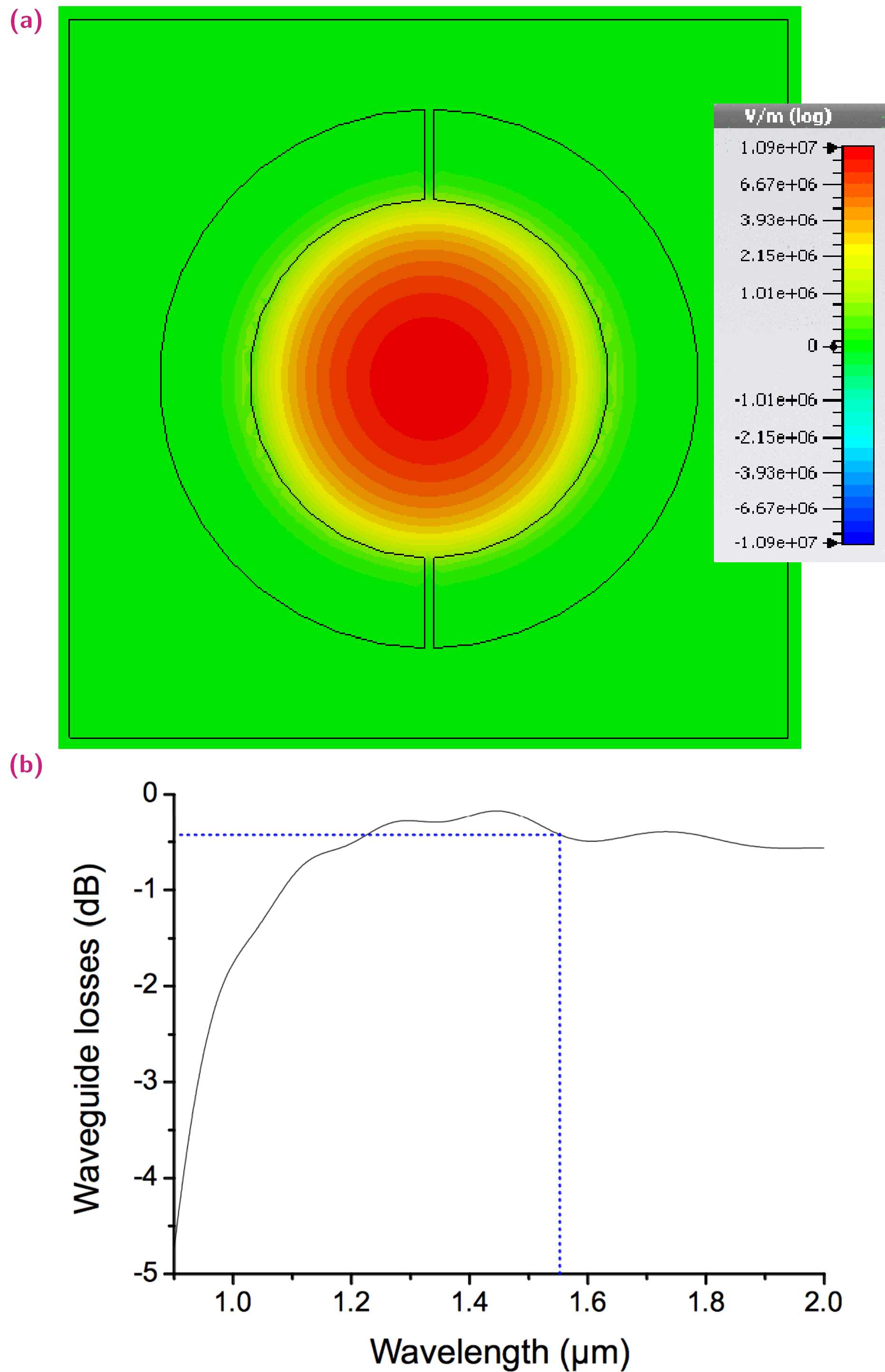

Figure 4.13: Transmission characteristics of the c-Si waveguide model as shown in figure 4.10c. (a) E-field distribution at the output port of the waveguide with a $2\,\mu m$ diameter shows that the modes are tightly confined to the waveguiding region owing to the geometry and the large difference in refractive indices. (b) The transmission curve shows that the waveguide has losses of around $0.4dB$ at $1550nm$. The curve plateaus after 1200 nm as silicon is almost transparent beyond this wavelength.

4.2 Material modification in SU-8 (IP-L)

As described in the previous chapters, material modification in SU-8 based IP-L resist was tested during the course of this work. Since Photonic Professional is a commercially available system, the focus of this part of the research was to extend the limits of the 3D designs and fabricate micro optical structures for on-chip optical communication and processing. These structures were fabricated as part of a larger framework of the project Saphir.

4.2.1 3D Polymer Optical Waveguides

The limits of the Photonic Professional, at the time of this research, was it write field. To achieve a highly accurate write field, it employed a piezo stage to move the sample in XYZ space. Due to this reason, the maximum movement in the XY plane was limited to $300\,\mu m$ along each direction. Although, this limit could be extended to a few centimetres by the so-called stitching process in which the linear stage carrying the piezo would move during the writing process. However, this method was seldom used as it resulted in a compromise to the quality of the micro optical structures. Therefore, it was decided to limit the length of the waveguides to $270\,\mu m$.

To be able to characterise the waveguides with MONA, they needed to have a coupling mechanism built into them during the writing process. For this, coupling lenses were designed that were to fit onto the waveguides. But this posed a problem with their relative sizes, which was easily solved by designing a taper at the end of the waveguides, also known as 3D Polymer Optical Waveguides (3DPOW). A CAD model of this technique is shown in figure 4.14. The 3DPOWs were all $270\,\mu m$ in length and $9\,\mu m$ in diameter. The diameter of the fabricated lens was $15\,\mu m$. The gap in these diameters was bridged by the taper.

To keep the waveguides erect and prevent them from falling, 'pillars' were designed along its length. The basic shape of the pillars is a tapering cylinder. They needed to have minimal contact to the waveguide, so as to minimise the losses due to leakage signal. Also, they needed to be stable, which meant that their bases had to be significantly large. Therefore, the top of the cylindrical pillar was designed to have a diameter of $4\,\mu m$ and the bottom $8\,\mu m$. Studies were performed to calculate the maximum stresses in 3DPOW (see figure 4.15). Design B was chosen as it showed minimal stress distribution and least pillar-waveguide contact area. In addition to that, the 3DPOW needed to have its end tilted at $45°$ angle. This was done to ensure that during measurement in MONA, only

(a)

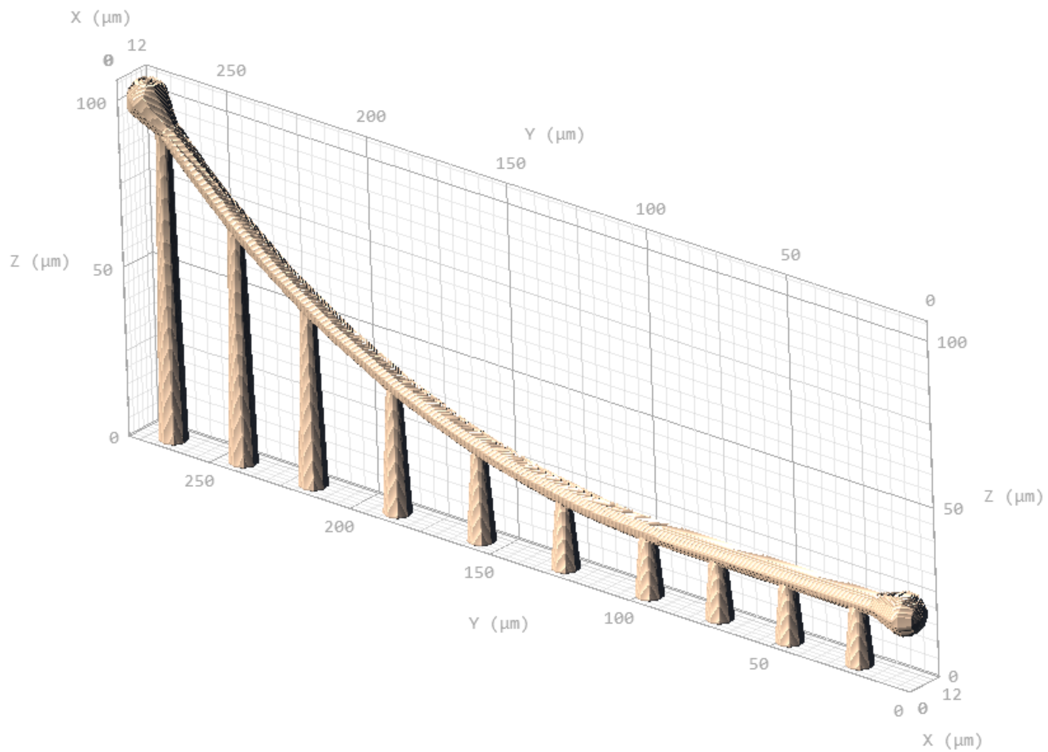

(b)

(c)

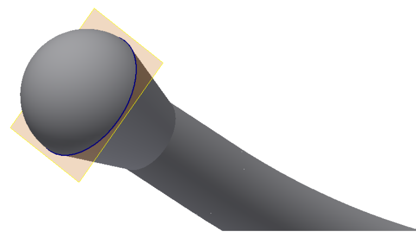

Figure 4.14: (a) A CAD design of 3DPOW, 270 μm in length and lenses on either of its ends. (b) The taper structure at the end of a 3DPOW of $9\,\mu m$ diameter. (c) A lens fabricated at the end of the taper with a diameter of $15\,\mu m$.

the signal that travelled through the waveguide was measured and not the one coming directly from the input fibre. The geometry of MONA was accordingly designed, as seen in figure 3.5.

4.2.2 Results and discussion

Along with 3DPOW, many more optically interesting structures were fabricated such as, rectangular grating couplers and interferometer structures. To determine the quality of the 3D lithography procedure with the Photonic Professional, the grating coupler's writing parameters were optimised for maximum reproducibility and its actual dimensions were tested on ten samples. Figure 4.16 shows a grating coupler from the top and an angled view. The dimensions are compared with the designed values in table 4.2. It summarises the estimated quantities. It is apparent that the dimensions agree broadly in line with the expectations. Only the height of the structure has a strong deviation, but this can be explained by a systematic error due to the change in viewing angle of the SEM. The waveguide is written accurately and is completely planar on the substrate.

Table 4.2: Dimensions of a grating coupler as shown in figure 4.16 - theoretical vs measured values.

Dimension	Theoretical (μm)	Avg. Measured (μm)
Waveguide length	100	105.48
Waveguide width	5	5
Waveguide height	3	7
Width of coupler area	60	61.78
Length of coupler area	70	72.45
Length of angled side of coupler area	35	34.11
Angle of coupler area	120°	122.56°

A future application and the reason for the design of coupler structures are more complex optical structures in the micrometre range, to be used as optical logic gates. For this purpose, an interferometer structure has been realised in a feasibility test. Figure 4.17 shows the SEM image of such these structures. Despite the writing direction normal to the waveguide direction, a curved and well-defined shape could be implemented. The gratings at the end of the waveguides are desgined to couple light in-and-out of the structure and the two waveguides are the two arms of the interferometer. The purpose here is to demonstrate the capability of writing complex optical structures via direct laser writing and 3DPOWs. The physical parameters such as the length of the arms and the grating must be adapted to perform an optical characterisation on the interferometers, which is beyond the scope of this work. Initial experiments were also performed to design and simulate optical ring resonator structures, as shown in figure 4.18. The design was

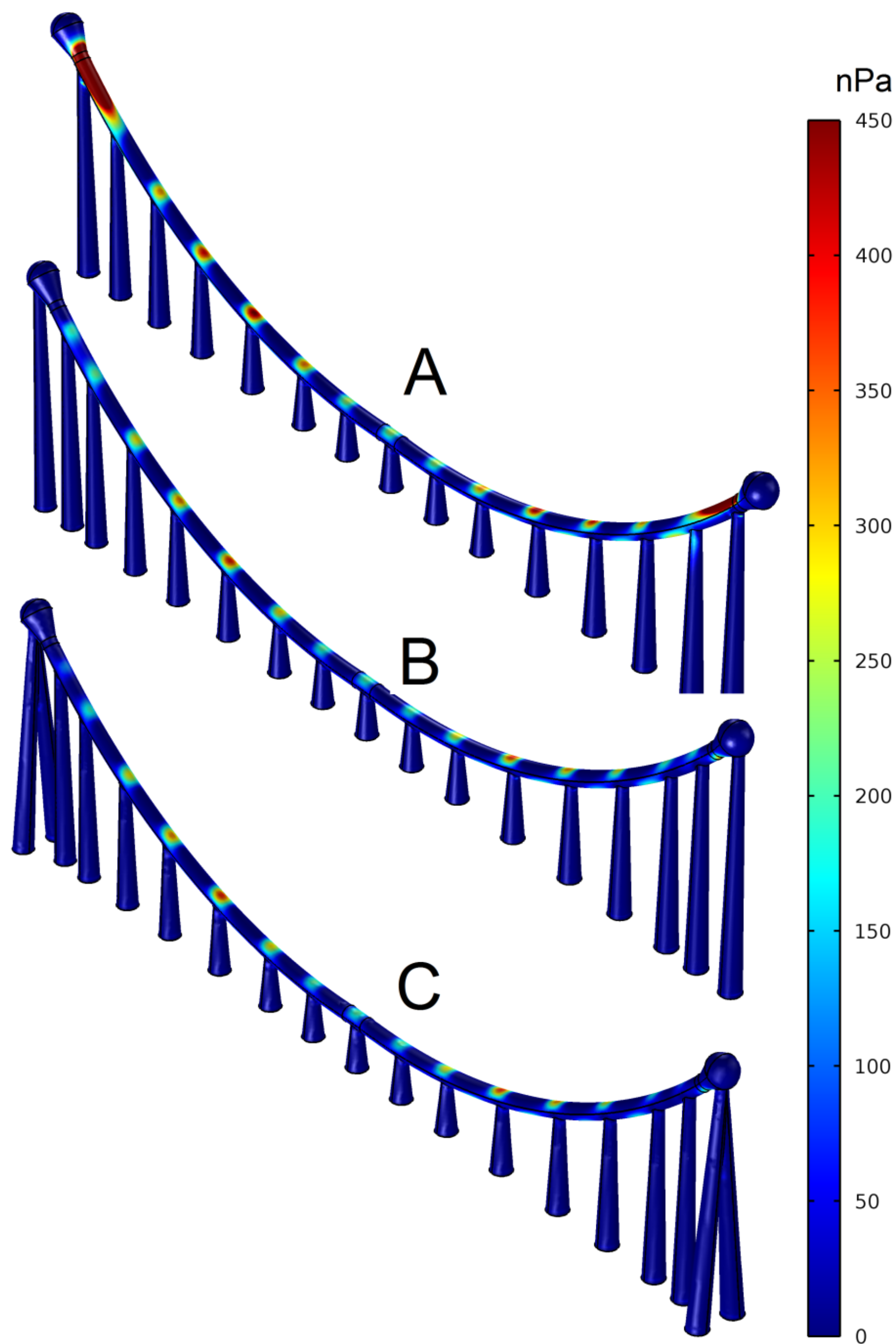

Figure 4.15: Three different designs for the supporting pillars for the waveguides were analysed for mechanical stresses in the waveguide. (A) Fewer pillars which means less optical leakage but high stress regions near the tip of the waveguides - over $500nPa$. (B) Supporting pillars under the lenses at the ends reduce the maximum stress down to $250nPa$. (C) Similar to B, the maximum stress value is less but added pillars at the ends would lead to more optical leakage.

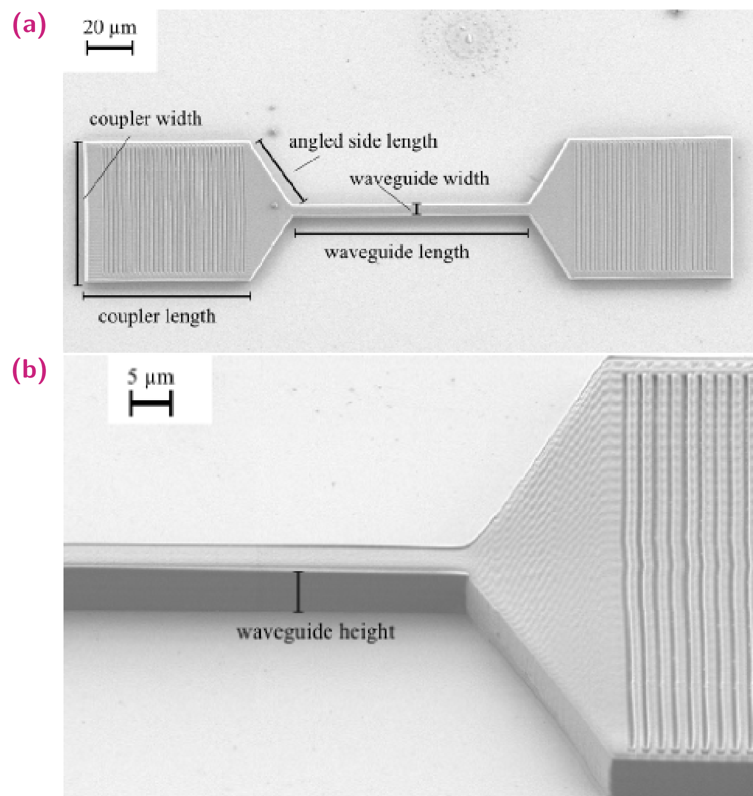

Figure 4.16: SEM images of a planar grating coupler with its dimensions. (a) Measured sizes of a planar grating coupler. (b) A close up view of the planar grating coupler with sizes measured at $45°$ SEM angle.

simulated for resonances in the 1300-1700 nm wavelength region which is often used in telecommunications. First simulation results show that the through port intensity almost close to zero, showing that most wavelengths are fully extracted by the resonator. The drop port relative intensity is at a constant $-5\,dB$, which is excellent for a first simulation test. Experimental results are not yet available for these structures and are suggested as part of the future work.

The 3DPOWs as described in the previous section was also experimentally realised. As compared to the planar structures above where a large part of the surface lies on the substrate, the 3DPOW has minimal contact with the substrate. This design feature ensures minimal leakage in the transmitted optical signal through it. Therefore, the writing strategy had to be accordingly modified. This also meant that the designing methods had to be adapted. Initially, for the 2D designs, a CAD drawing was made on the software Inventor and exported into an STL format to be written by the Photonic Professional. However, in this method there is no layer wise control. This means that the writing style and steps will be automatically determined by the writing software. This works good with the 2D structures but not with 3DPOW. Therefore, the structures were designed with Matlab where there was precise control over each layer and its order of writing. This was then converted into an GWL format and fed into writing software. The results can be seen in figure 4.19.

As the primary aim of the 3DPOW is to act as a waveguide, an array of 3DPOWs were fabricated with one end of the waveguide tilted at a $45°$ angle. This was to ensure that when they were optically studied under MONA, no direct light measurement would be made. Results are shown in figure 4.20. As seen, the mode field scan appears to be fairly symmetric and reproducible. However, the losses that these waveguides possess is significantly large. At over $12\,dB$ losses per $270\,\mu m$, they are a good proof of concept design but have a lot of room of improvement.

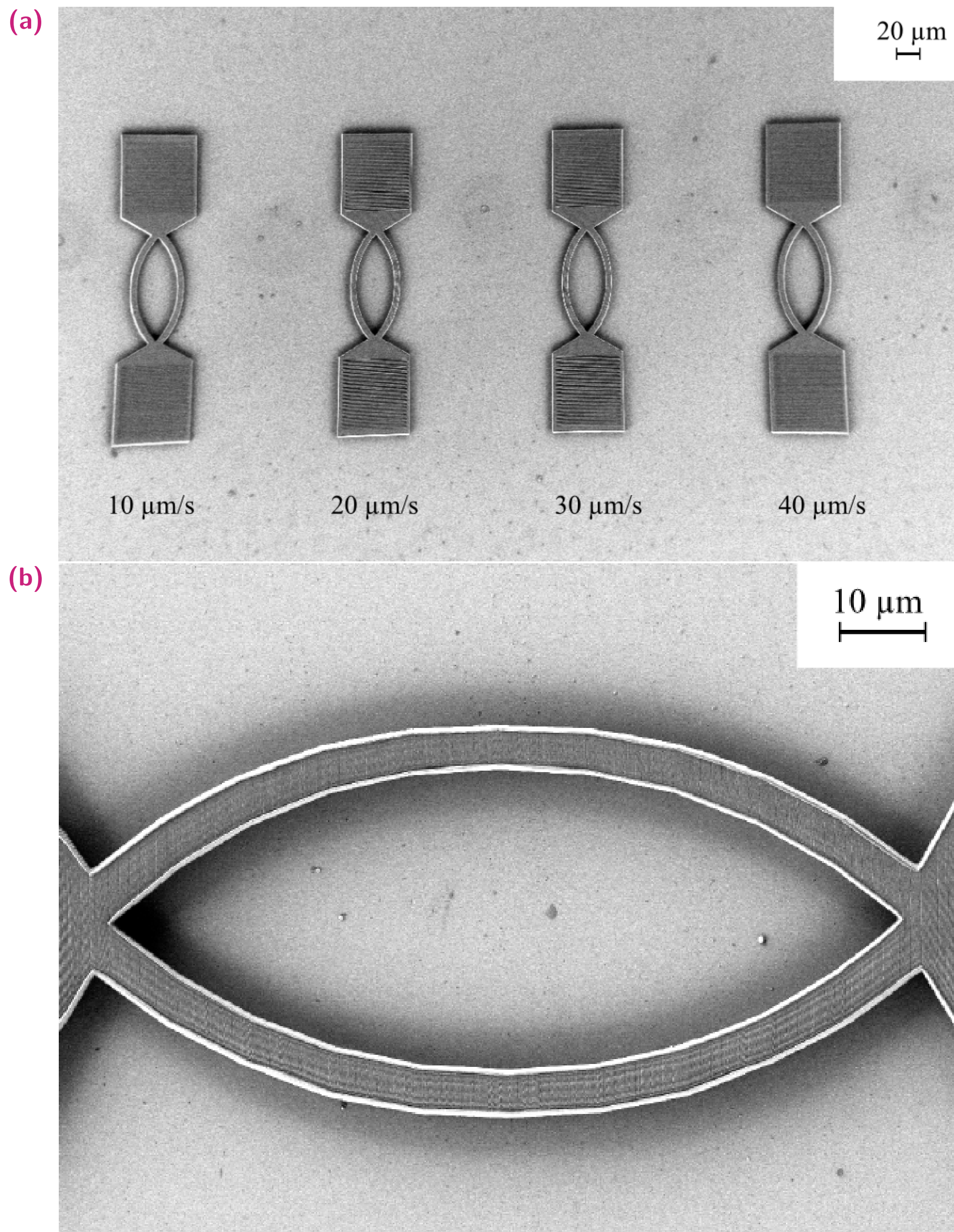

Figure 4.17: SEM images of a planar interferometer grating coupler with write speed variations. (a) Speed test of the interferometer coupler. (b) Enlarged view of the waveguides. Each waveguide represents an arm of the interferometer

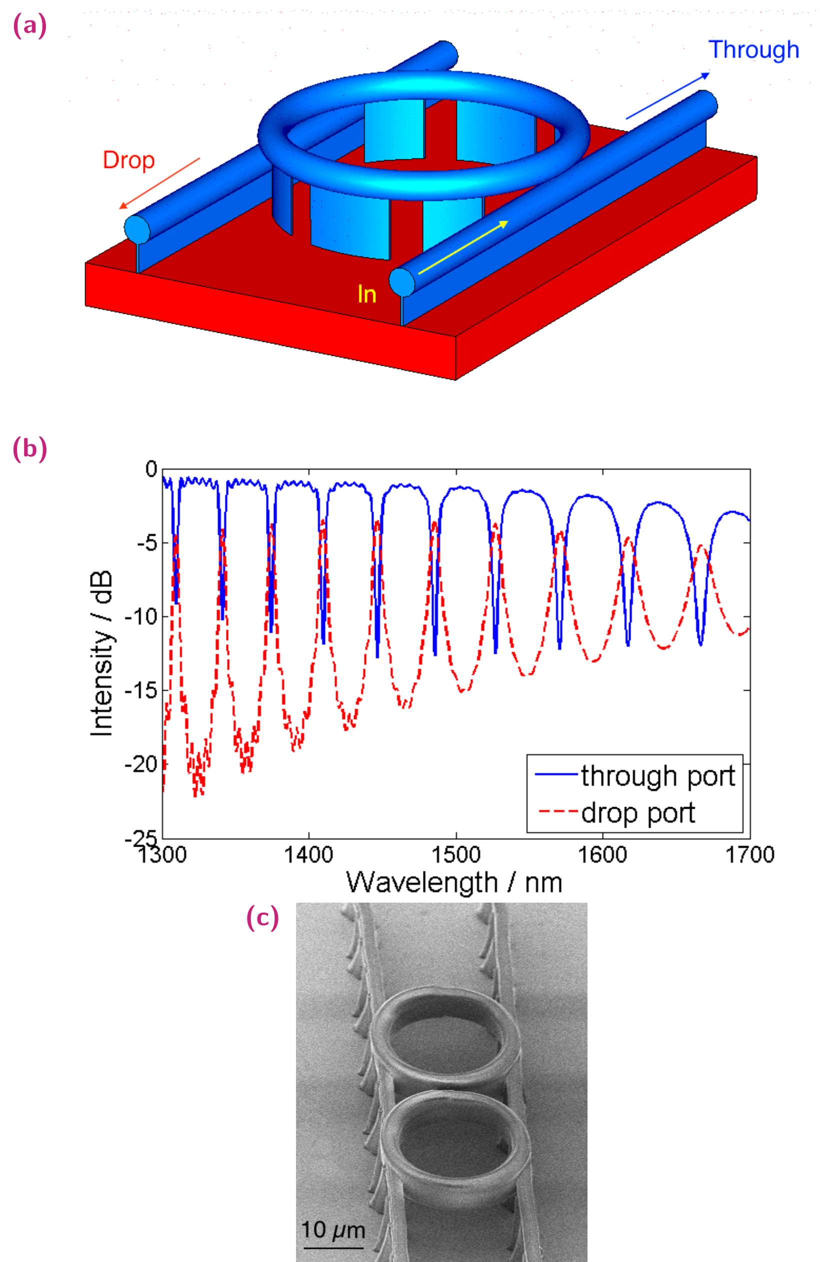

Figure 4.18: Ring resonator design and fabrication. (a) Design of a ring resonator showing the in, drop, and through ports. (b) Simulated intensity output of the resonator showing minimal losses between the through port and drop port signals. (c) A SEM image of a double ring resonator structure.

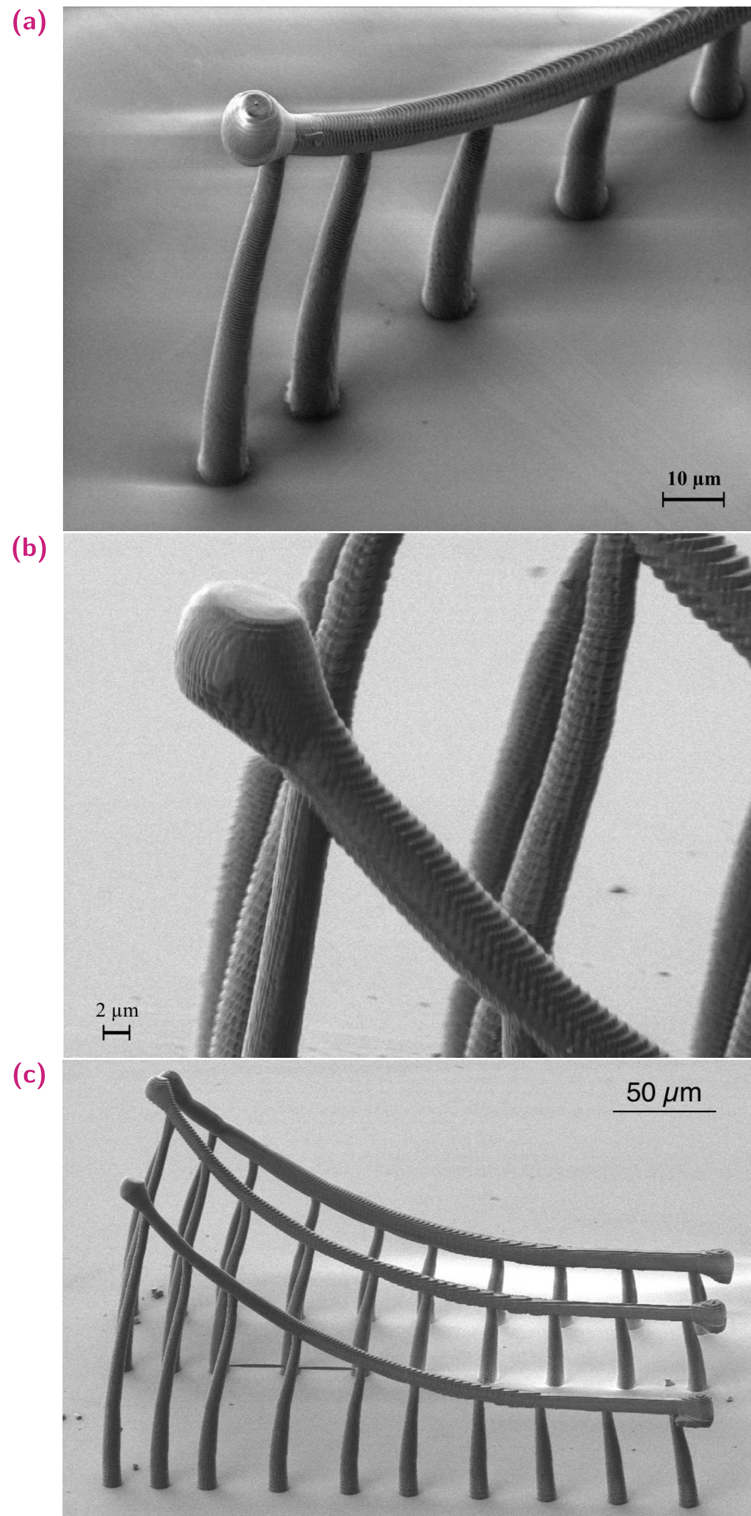

Figure 4.19: SEM images of 3D Polymer Optical Waveguides. (a) 3DPOW imaged at an angle of $45°$. (b) A close up view of the taper and lens of the waveguide. The ridges along the length arise from the algorithm used to slice and write the structures. (c) An overview image of three 3DPOWs that are $270 \mu m$ in length and realised with the design as showed in figure 4.14.

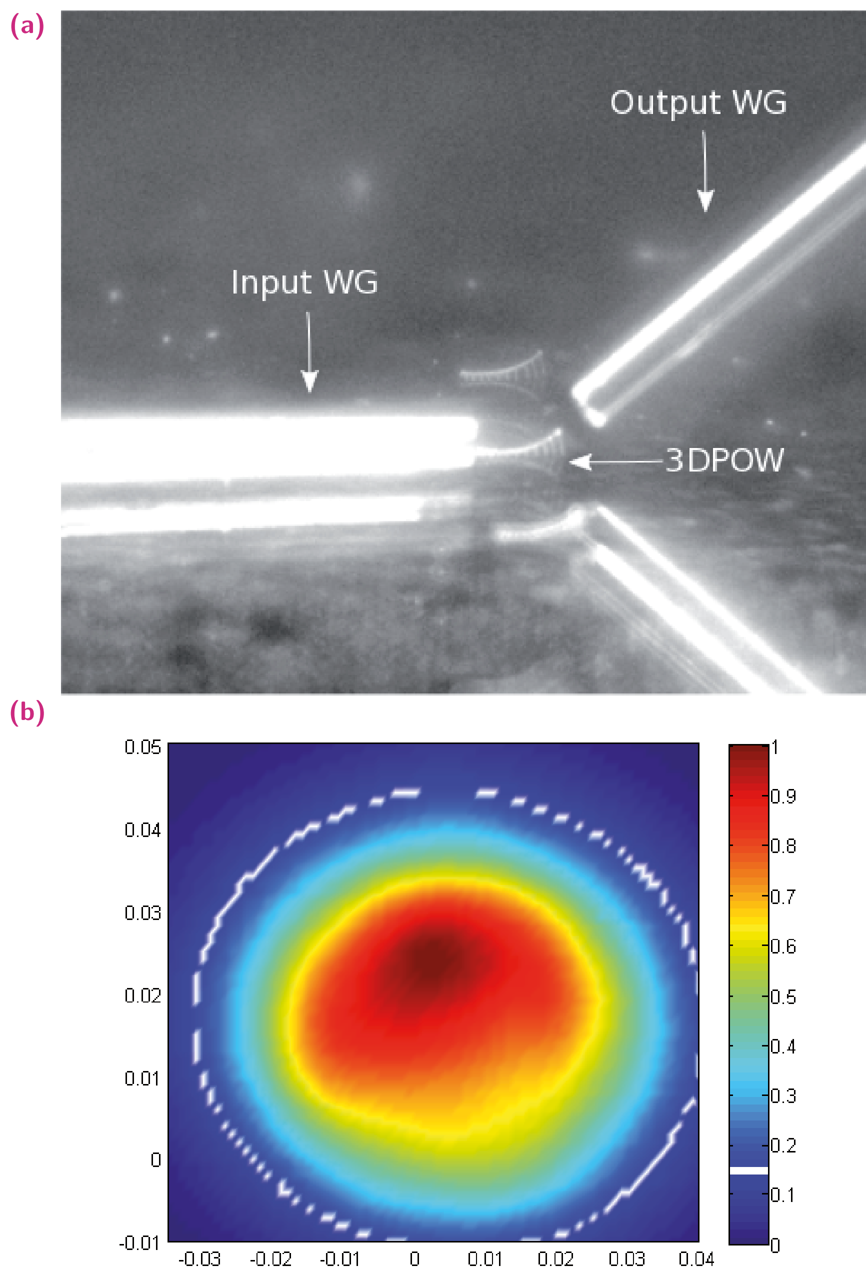

Figure 4.20: Images of 3D Polymer Optical Waveguides being studied under MONA and the corresponding mode field scan. (a) Light being coupled into a 3DPOW and read out via optical fibre at 45° angle. (b) Mode field scan of a 3DPOW showing a nearly ideal distribution. The axes represent the scan area in mm. Intensity is in normalised arbitrary units.

4.3 Summary

The formation of optically detectable buried structures in silicon is demonstrated as a new avenue to inscribe three dimensional structures for micro optical usage. This approach may enable a technological breakthrough in terms of optical on-chip monolithic integration of optical devices. Further structural and optical characterisation as well as a thorough theoretical understanding and physical modelling of multiphoton absorption (MPA), self phase modulation (SPM) and self focussing processes in silicon are necessary. The simulated waveguides show promising results for subsurface optical waveguides. Furthermore, 3DPOW are promising on-surface and on-chip micro structures with excellent robustness. Together with subsurface structures in silicon, they can pave way for a complete new system of on-chip, in-chip, and through-chip signal transmission and processing. Technologically, to fabricate, they require the similar condition. This can be advantageous in terms of unifying the fabrication process. A few examples and ideas are presented in chapter 6.

5 Applications of 3D Microstructuring

Sometimes when you innovate, you make mistakes. It is best to admit them quickly, and get on with improving your other innovations.

— **Steve Jobs**

In this chapter, a few applications of 3D in-volume microstructuring in polycarbonate and acrylic is discussed and demonstrated. A prototype of an Optical Vector Matrix Multiplier is demonstrated with emphasis on 3D milled acrylic waveguides. Then, realisation of 3D Computer Generated Volume Holograms is Foturan glass is discussed. Finally, a few results pertaining to the micro structures in acrylic for crystallographic studies.

5.1 Optical Vector Matrix Multiplier

Vector matrix multiplication is a fundamental operation in small to large scale algebraic problems. Almost any modern digital signal processing technique is reduced to solving a set of linear equations that is sometimes laborious and extremely resource intensive for a conventional *electronic* computer. Optical computation possesses an intrinsic parallelism and this many efforts have been made to develop optical devices capable of performing parallel operations [98, 99]. Solving linear equations almost exclusively involves dealing with vectors and matrices and simple algebraic operations between them, such as multiplication. For example, the equations $ax + by = c$ and $dx + ey = f$ can be solved by considering them as vectors and matrix, such as:

$$\begin{bmatrix} a & b \\ d & e \end{bmatrix} \times \begin{bmatrix} x \\ y \end{bmatrix} = \begin{bmatrix} c \\ f \end{bmatrix}$$

Optical vector matrix multipliers (OVMM) have gained importance since the early days of electronic computing since they offer a much direct solution to the problem of equation solving in all areas of science. Since vectors and matrices are interchangeable with a system of linear equations, solving them optically for higher order equations makes the

technique immensely attractive. Various methods and designs have been put forward in the last couple of decades that included both free space optics and fibre based architectures [100, 101]. As shown in equation 5.1, the basic vector matrix multiplication involves each of the elements of a vector to be algebraically multiplied with the corresponding matrix element and summed over the matrix row to produce an element in the resultant vector.

$$\begin{bmatrix} v_1 \\ v_2 \\ \vdots \\ v_p \end{bmatrix} \times \begin{bmatrix} m_{11} & m_{12} & \cdots & m_{1q} \\ m_{21} & m_{22} & \cdots & m_{2q} \\ \vdots & \vdots & \ddots & \vdots \\ m_{p1} & m_{p2} & \cdots & m_{pq} \end{bmatrix} = \begin{bmatrix} v_1 m_{11} + v_2 m_{12} + \cdots + v_p m_{1q} \\ v_1 m_{21} + v_2 m_{22} + \cdots + v_p m_{2q} \\ \vdots \\ v_p m_{p1} + v_p m_{p2} + \cdots + v_p m_{pq} \end{bmatrix} = \begin{bmatrix} r_1 \\ r_2 \\ \vdots \\ r_p \end{bmatrix} \tag{5.1}$$

This can be optically realised by taking a linear array of light sources to act as a vector; the matrix can be realised by modifying the light off a surface and spatially controlling the reflection / transmission at predefined points. Figure 5.1 shows a schematic of a vector matrix multiplier with a vector source in which each element interacts with a row of the matrix. The resultant product is imaged using a detector vector whose each element represents the corresponding element of the resultant vector, according to equation 5.1.

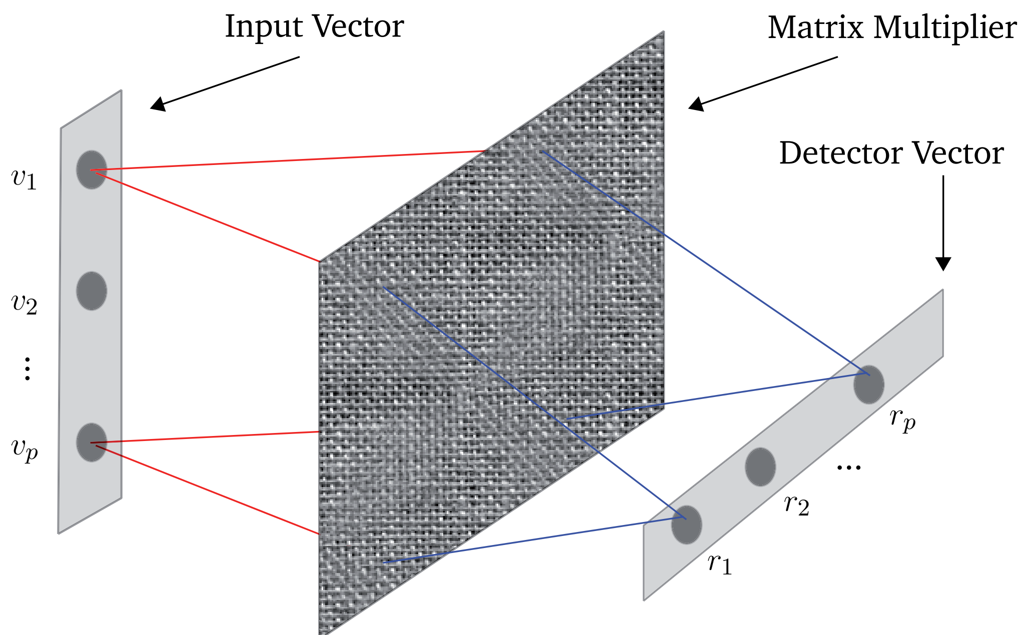

Figure 5.1: Schematic of the Optical Vector Matrix Multiplier. The information introduced by the input vector is distributed to the elements of multiplier matrix. The resulting signals of the individual matrix elements are collected in the elements of the detector vector. The notations corresponds to equation 5.1.

The Stanford multiplier [98] is one of the pioneering examples of a experimental realisation of an OVMM implementation. It consisted of a light source array, an optical lens, a spatial light modulation (SLM) to act as the matrix, and a photo detector array. This set-up

was a good proof-of-concept, however, it was extremely sensitive to vibrations. The ideal solution and approach to realising an OVMM would be to have it as robust as possible. This would involve fabricating custom silicon chips, also known as ASIC (Application-specific integrated circuit).

During the course of this thesis, a simpler prototype was realised using LEDs as source array, LCD screen as multiplier matrix, and a photo detector array, as shown in figure 5.2. This approach successfully demonstrated the proof of concept of an OVMM involving macro to micro sized optical elements. Arduino Uno, a popular microcontroller unit, was used to control the LEDs, the matrix element and read out the values from the photodiodes. A critical element of this prototype was to design efficient waveguides that would carry the light from the LEDs to the matrix, and from the matrix to the photodiodes.

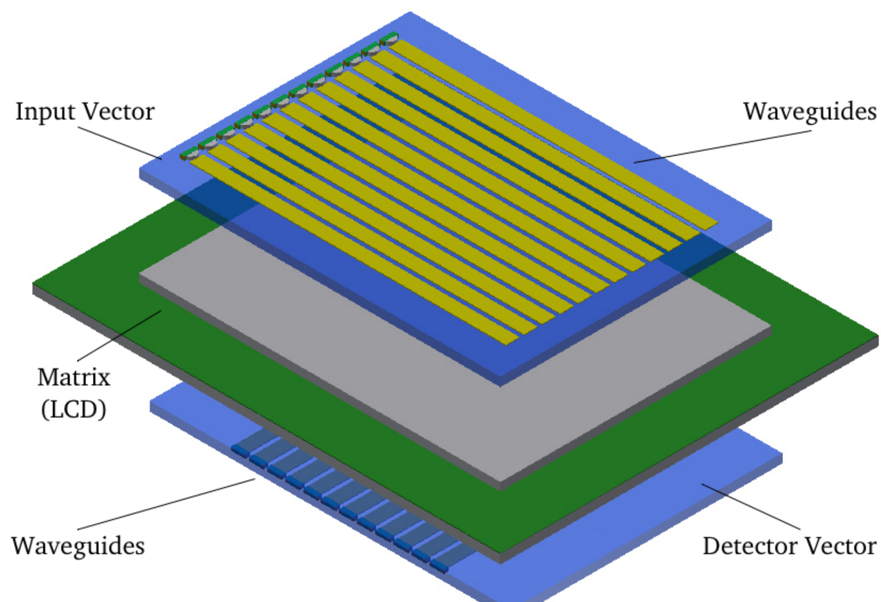

Figure 5.2: Schematic of the proposed Optical Vector Matrix Multiplier. The three-layered design has an LED input vector with waveguides to distribute the light throughout the LCD display in second layer. The LCD display is used to represent the matrix with dynamic control via a micro controller. The third layer has similar waveguides arranged at 90 degree to the input vector and coupled with photodiodes.

5.1.1 Electronic components of Optical Vector Matrix Multiplier

Since the prototype involved using a lot of commercially available electronic products, the 'simpler' variants were chosen so as to be able to hack into their individual modules. For example, the LCD module, as described in the section below, had to be simple because its

back-light had to be removed to expose the sandwiched LCD. In the following sections, the individual components are discussed along with some of their specifications.

LCD module

The ST7735R is a single-chip controller graphic type TFT-LCD. The chip is capable of connecting directly to an external microprocessor via a Serial Peripheral Interface (SPI). The display data can be stored in the on-chip display data RAM of $132 \times 162 \times 18$ bits. It can perform display data RAM read/write operations without external operational clock to minimise power consumption. With 18 bit colour, it can display 262,144 shades. But during the course of this work, it is used in a binary black and white (transparent) mode. It is also compatible with $3.3V/5V$ TTL (transistor-transistor-logic). This is useful because it is then possible to connect the LCD directly with the microcontroller without any external power supply. A few necessary specifications are mentioned in table 5.1.

Table 5.1: Specifications of ST7735 TFT-LCD Module

Specification	Value
Resolution	$128W \times 160H$ dots
Board size	$5.00 \times 3.4cm$
View area	$28.03W \times 35.04Hmm$
Dot size	$0.06W \times 3 \times 0.18Hmm$
Dot Pitch	$0.18W \times 0.18Hmm$

To expose the bare LCD, the casing was removed and the back-light module was carefully de-soldered. This allowed for controlling the pixels electronically with a custom back-light channel, which in this case, will be a vector of LED lights. The split view and the working of one such modified LCD is shown in figure 5.3.

LEDs and photodiodes

The choice of LED for this prototype is the 1101W series. It has a wavelength of $647nm$ and is of the BR series, which meant that the die material is GaAlAs. At forward current values of $20mA$, its typical values of luminosity is $12.8mcd$. With a water-clear-resin type package, its dimensions are $3 \times 1.5mm$, which made is suitable to be used alongside the waveguides. The low values of forward current also meant that it could be powered with the same microcontroller instead of an external power supply.

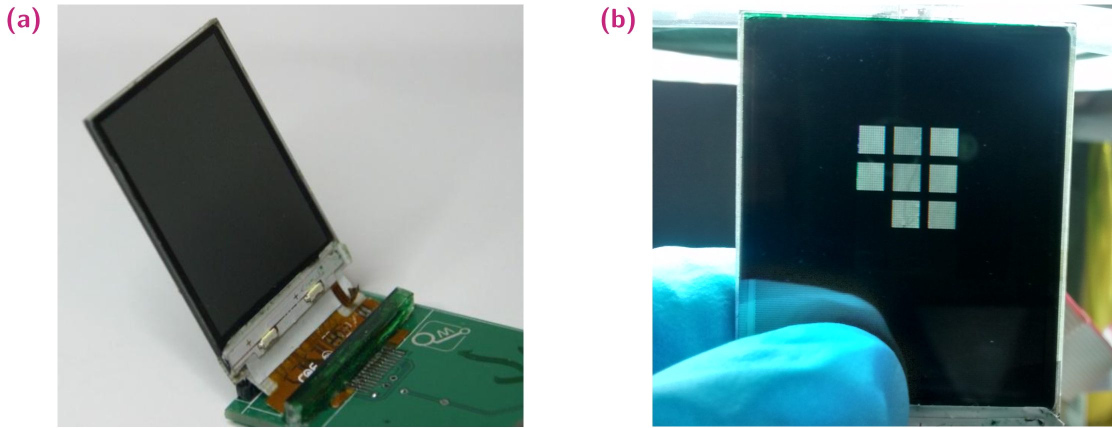

Figure 5.3: (a) Exposed LCD module showing sandwiched glass without back-light. (b) The LCD programmed to display blocks of pixels as a functional matrix elements with a table lamp as back-light.

For the photodiode, BPW34 is chosen. The BPW34 is a high speed, highly sensitive and inexpensive general-purpose PIN photodiode in clear plastic case. The device is sensitive to visible and infrared radiation. It has large active area with angle of half sensitivity of $\pm 65°C$ contributing to its high sensitivity to low intensity light. The dimensions of the photodiode are $5.4 \times 4.3mm$.

Further technical details about the LED and the photodiodes are given in appendix C.1 and appendix C.2, respectively.

Arduino microcontroller

Arduino Uno is a microcontroller board based on the ATmega328P. It has 14 digital input/output pins (of which 6 can be used as PWM outputs), 6 analog inputs, a $16\,MHz$ quartz crystal, a USB connection, a power jack, and a reset button, amongst other terminals. It operates at $5\,V$ making it suitable to directly interface the LEDs and photodiodes. The ATmega328P has a built in flash memory of $32\,KB$ which suffices the memory needs for this OVMM prototype. More details in appendix C.3.

5.1.2 Waveguide optimisation for OVMM

Acrylic glass, also known as poly (methyl) methacrylate (PMMA), a clear glass-like plastic was found to be a suitable material for the waveguides. The material is transparent, lightweight, shatter-resistant and easy to cut and polish unlike glass, which makes it

appropriate choice to make waveguide. PMMA is also well suited for many microelectronic applications used as a high-resolution positive resist for several lithographic processes.

The material is a $3 \times 3mm$ square rod with $1000mm$ length. The long strip was then sliced into $30mm$ pieces to be shaped as required waveguide. To understand the pertinence of PMMA as waveguide, it is necessary to investigate the optical properties of the material. It is clearly established that good waveguides upholds the basic principles of light like reflection, refraction and total internal reflection. The key feature in our case is the refractive index (n) of PMMA and air ($n = 1.000271206$ for $647nm$). The refractive index of PMMA is 1.4884 for red LED with wavelength $647nm$. The waveguide operates in similar but two modes, namely:

1. Transmissive
2. Receptive

In transmissive mode, the LED feeds the light from one end of waveguide and the light is transmitted and distributed along its length. In receptive mode, the waveguide collects the light absorbed along its length and directs them to an end with photodiode, according to figure 5.2. To bring this functionality into the waveguides, they have to periodically patterned on their one of their surfaces. This allows for light to escape the waveguides at regular pre-defined intervals. During the course of this work, four such patterns were tested which will be discussed. A schematic of the waveguides working in these two modes is shown in figure 5.4.

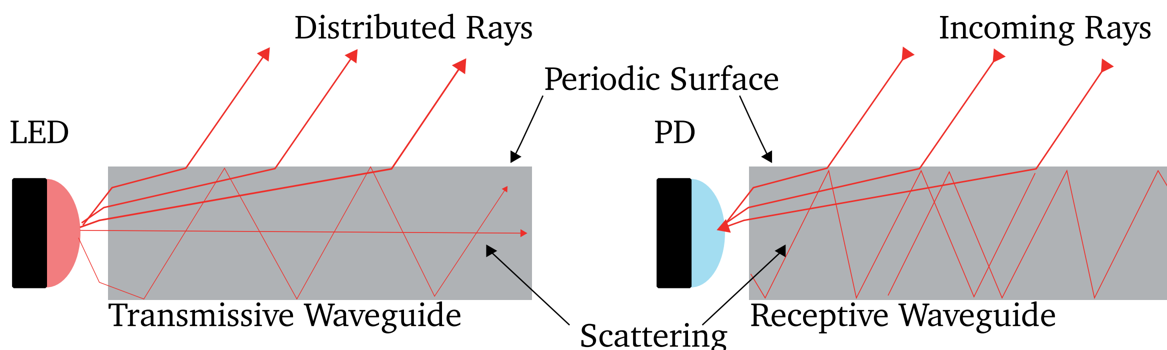

Figure 5.4: Waveguides in transmissive and receptive modes. (Left) Light emitted from LED enter the waveguide and due to its patterned surface, it exists the waveguide from the top surface. (Right) Light enters the waveguide from the patterned top surface and is coupled into a photodiode (PD) that is placed at one end. In both these modes, however, there is significant scattering in the waveguides.

They were characterised by placing a red LED (647 nm) at one end of the waveguide and measuring the emitted light along its length. The four designs that were studied are shown in figure 5.5. Figures 5.6 and 5.7 show the experimentally determined intensity

distributions along the length of different waveguides. The waveguides are all 14 mm long. In the case of the plain/blank and the sloped waveguides, one can see that the emitted light near the LED (position 0) is very low and it increases as one reaches the end of the waveguide. This arises from the fact that the polycarbonate waveguides offer very little or no scattering in the bulk but the flat ends are responsible for most of the back scattered light. On the other hand, the hand roughened (HRW) and the arbitrary sand blasted (ASB) waveguides show an inverse response with the intensity distribution to their relative positions. Most of the light is scattered at the beginning while the intensity decreases almost linearly towards the end. Although this linearity can be made use of by assuming it as a co-efficient to the intensity distribution, the response amongst the other waveguides is not consistent.

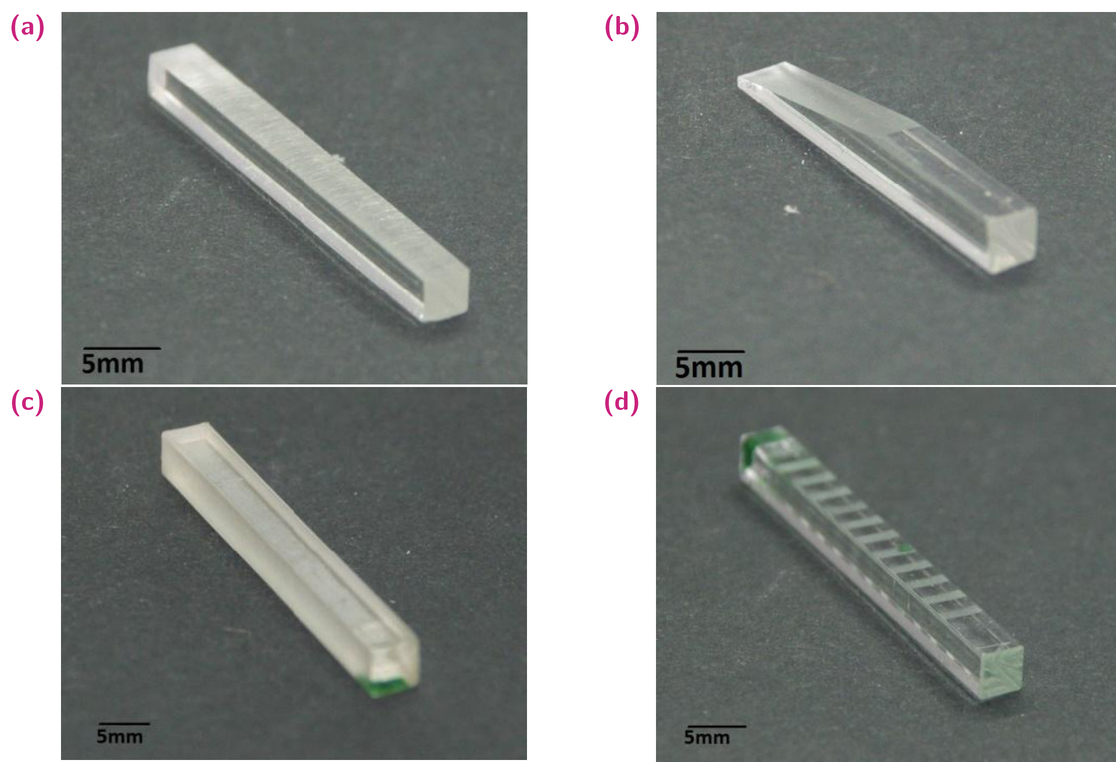

Figure 5.5: Four different designs of the waveguides that were characterized as possible candidates for the final OVMM prototype.All waveguides are $14mm$ long. (a) Hand-roughened waveguide (HRW). (b) Sloped waveguide. (c) Arbitrary sand blasted waveguide (ASB). (d) Patterned sand blasted waveguide (PSB).

Figure 5.7 shows the intensity distribution in eight different patterned sand blasted (PSB) waveguides. They were studied in a similar method as in figure 5.6. The almost flat intensity response curves of these waveguides are of significant importance to the design of the OVMM because they offer a possibility to set a cut off level to distinguish between the ON and OFF states. Therefore, PSB waveguides are chosen as the preferred kind of waveguide for prototyping the OVMM.

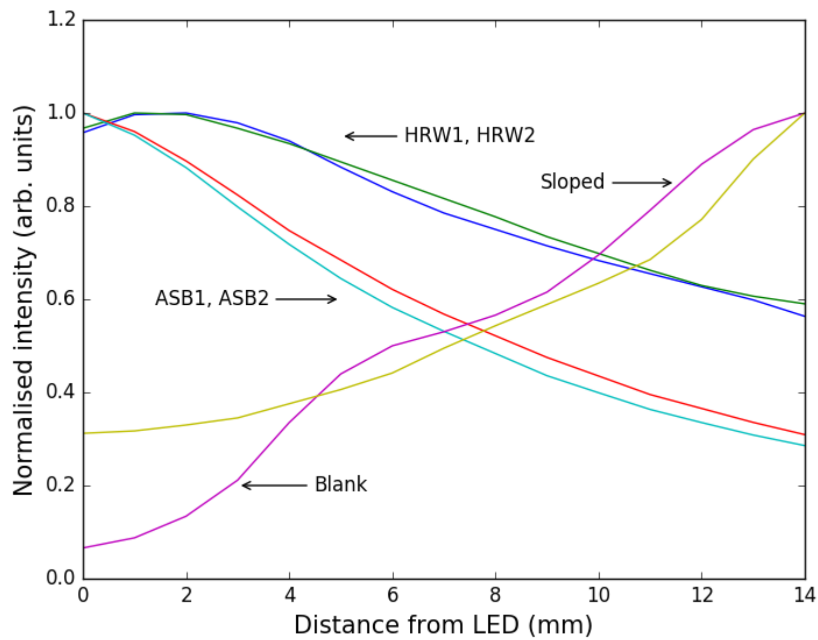

Figure 5.6: Intensity distribution over different waveguides. For the blank and sloped waveguides, emitted light near the LED (position 0) is very low and it increases as one reaches the end of the waveguide. The HRW and the ASB waveguides show an inverse response with the intensity distribution to their relative positions.

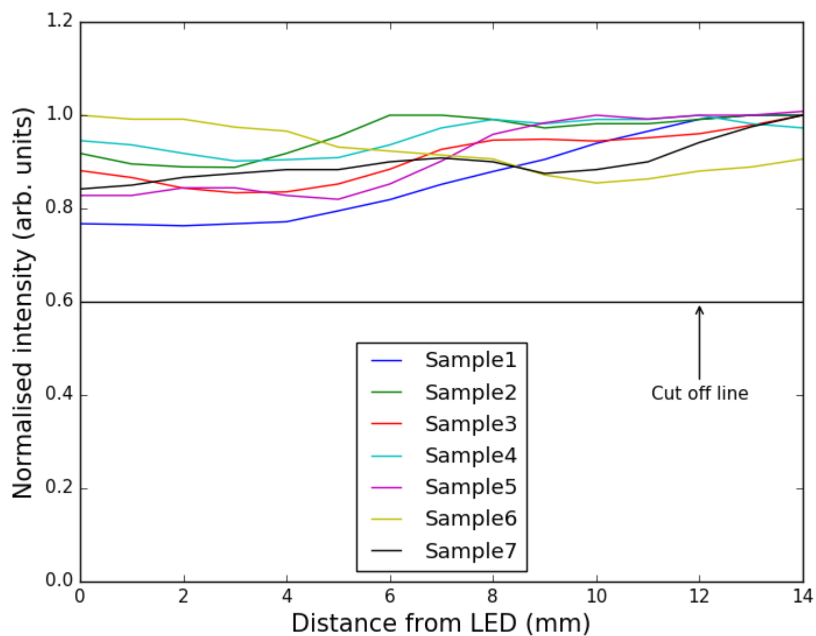

Figure 5.7: Intensity distribution over seven patterned sand blasted (PSB) waveguides. The relatively constant intensity distribution above a certain Cut-off value is essential in using the PSB waveguides in the ON and OFF states.

5.1.3 OVMM operation and prototype

The basic vector matrix multiplication involves each of the elements of a vector to be algebraically multiplied with the corresponding matrix element and summed over the matrix row to produce an element in the resultant vector. This can be optically realised by taking a linear array of light sources to act as a vector; the matrix can be realised by spatially controlling the reflection/transmission at predefined points. The macroscopic physical-prototype (figure 5.2) is composed by a sandwich of two LCD structures with orthogonal polarisation sending an image to an integrated camera. One LCD works as input vector, and the other as input matrix. The camera produces the output image. This image is automatically accumulated by the electronics to generate the output vector, i.e., the vector matrix multiplication.

To realise the design, three PSB waveguides were attached with LEDs at one end and were mounted on the top surface of the LCD. Three more of those, attached with photodiodes, were attached to the bottom surface of LCD; but perpendicular to the top three. The LEDs, LCD, and photodiodes are all controlled by the Arduino microcontroller board. The output of the photodiode is amplified using a simple Op-Amp circuit before being read out by the microcontroller. Figure 5.8 shows the final set-up of the OVMM. The set-up was enclosed in a box and tested successfully. 3×3 binary VMM are successfully performed. The limiting factors are the speed of input and the electronics. A detailed explanation can be found in the associated Master's thesis by Mr. Chauhan [102].

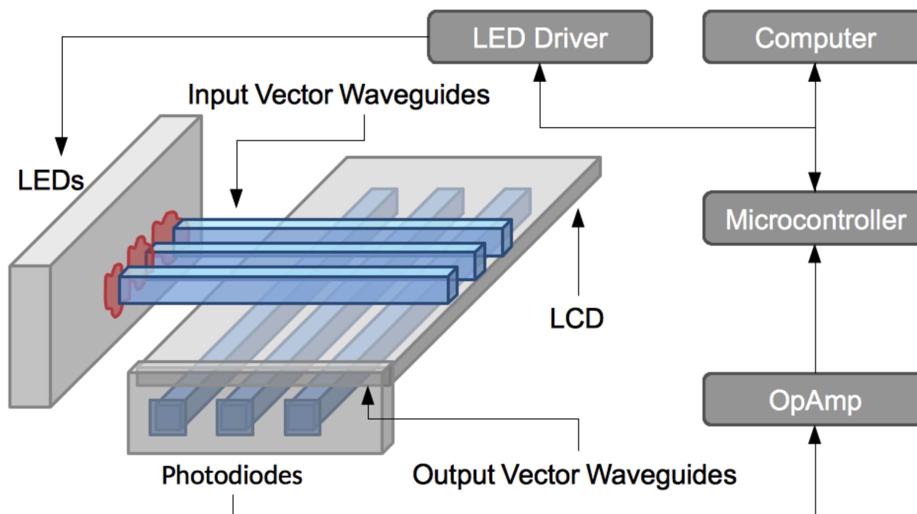

Figure 5.8: The 3×3 optical matrix multiplier is formed by the six waveguides and a LCD arranged as shown. The LEDs and photodiodes are placed as shown. The matrix elements on LCD are aligned such that they are positioned at intersection of top and bottom waveguides. The required electronics are connected to input and output of the optical multiplier, which is controlled by microcontroller.

5.2 3D Computer Generated Volume Holograms - CGVH

In the recent past, major focus has been on 3D diffractive and holographic optical elements, which offer more degrees of freedom as opposed to their 2D counterparts [103, 104]. In a CGVH several projections of given far-field intensities can be encoded in the design process and by subsequently illuminating it with the corresponding plane reference waves, single or a linear combination of these projections can be decoded. In the current state of the art, such CGVHs are fabricated by direct laser writing in the bulk of glass using a tightly focused femtosecond (fs) laser beam. This process relies on highly localised light excitation for the modification of material through laser induced breakdown. One major limitation of this approach is the achievable focal volume which directly limits the voxel size. In order to fabricate devices with advanced functionalities, e.g. for applications in wavefield synthesis [104], voxel sizes on the order of $\approx 1\,\mu m$ are necessary [105] since this leads to devices with more degrees of freedom and to reduced cross talk between single projections in multiplexed devices.

The experimental set-up described in Chapter 3, LeNA, is used to fabricate the CGVHs in commercially available photosensitive Foturan glass. This involves 3D modification

of the refractive index through a nonlinear six-photon absorption process [106]. To fabricate the designed structure, the fs laser system with a wavelength of $1550\,nm$ and a pulse length $800\,fs$ were focussed into the glass using an objective lens (40x; NA = 0.75). Since activating the photo sensitivity of Foturan glass with an IR fs laser allows for the manipulation of the refractive index in a subsequent post-bake process [106], the threshold of the fabrication energy below which an index difference $\delta n < 1 \times 10^{-3}$ could be induced was first experimentally determined. The corresponding parameters were found to be a pulse energy of $E = 5\,\mu J$ at a repetition rate of $10\,Hz$. With the glass samples mounted on a translation stage, which was synchronised to the laser pulse output, the designed structure was then inscribed voxel by voxel. Finally, the samples were post-baked at a constant temperature of $550°C$ for a period of 3 hours in order to achieve an index difference of $\delta n = 1 \times 10^{-3}$.

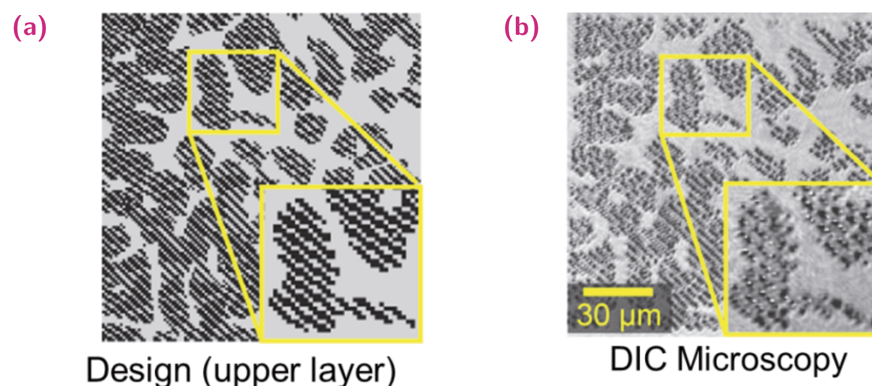

Figure 5.9: (a) Refractive index distribution $n(x)$ of the top layer of a binary CGVH with dimensions of $64 \times 64 \times 96\,\mu m$ (b) A differential interference contrast microscope (DIC) measurement of the index contrast recorded after fabrication. Source [107].

Using a DIC (Differential Interference Contrast) microscope, the distribution of the induced refractive-index change was characterised and a good agreement between designed and fabricated structures could be observed (see figure 5.9). From these results it is clear that index distributions having smooth internal contours and with voxel dimensions on the order of $1\,\mu m$ can be fabricated.

5.3 Summary

In this chapter, a working prototype of an all Optical Vector Matrix Multiplier was realised that could perform binary 3×3 matrix multiplication. The process involved optimisation of waveguides at a macro scale. To realise an OVMM at a micro-scale, for example on a chip, the bottle neck would be the integration of optoelectronic components such as LCDs or SLMs or micro-mirror arrays with existing waveguide writing technologies.

Furthermore, 3D computer generated holograms were successfully written via LeNA and optically characterised. This demonstrates the capability of LeNA beyond just subsurface modification of silicon, and into a durable 3D Direct Laser Writing set-up. The realisation of 3D crystallographic structures in acrylics further strengthens the argument for the robustness and precision of LeNA.

6 Conclusion and Future Work

An expert is a person who has made all the mistakes that can be made in a very narrow field.

— Niels Bohr

This chapter contains a summary of all the results shown in this thesis and suggestions and roadmap for future research.

6.1 Conclusion

A list of objective and goals were listed and planned, as shown in section 1.4. Despite this work being highly exploratory and pioneering in nature [108], almost all of those objectives were met with great success. In this section, all those goals will be individually listed and the degree to which they have been completed and can be improved upon will be discussed. The following five goals and objectives were chalked for the duration of this work:

6.1.1 Nonlinear absorption of laser irradiation & process parameters

In chapter 2 the physics behind nonlinear laser matter interactions was discussed. The current understanding of nonlinear absorption involves an ultrafast laser pulse being tightly focussed into a material with a significantly large dielectric response. When this process is extended to semiconductors like silicon, the intensity of radiation required to induce these reactions increases by orders of magnitude. One of the main reasons for this is the mechanical hardness and the Young's modulus of silicon which is way higher than that of glass and other softer polymer based materials. Therefore, the process parameters and the existing commercial laser systems had a very narrow bandgap of agreement. The choice of laser, depending on the process parameters, was the best choice that was available at the time of performing these experiments (ca. 2012).

6.1.2 Experimental set-up

The Raydiance MD50 laser was chosen for inducing subsurface modifications in silicon. This was used in a 3D Direct Laser Writing set-up (LeNA) that was built specifically for this purpose. The set-up included linear stages in an XYZ configuration controlled by the Fringe Processor software. The range of movement in XY plane was $150\,mm$ and in the Z direction was $4.8\,mm$. As described in chapter 3 and appendix B, a custom scripting language called Yet Another Language (yal) was developed to feed in the process parameters into the LeNA set-up. The scripts included information about the XYZ position of the sample, the velocity and acceleration of the linear stages, and the state of the laser beam. This set-up was automated to the extent that it was not just a laboratory apparatus but was also used to prepare samples for industries.

Another set-up that was used was Photonic Professional from Nanoscribe. Since this was a complete machine that was bought, there was little to no custom modifications required to operate it. The process, however, involved feeding it with script files (similar to LeNA) which was improved upon over time with complex structures being created with tools like Matlab.

A Modular Optic Nano Analyser (MONA), was a tool created to image micro and nano structures with a very high precision. The linear stages in MONA had a travel range of $15\,mm$. The nano-cubes mounted on these XYZ configuration of the linear stages had a resolution of $1\,nm$. This meant that extremely high resolution scans could be made over significantly large areas. This set-up was used to scan the mode-field from micro optical waveguides.

6.1.3 Subsurface modification in silicon and polycarbonates

With the apparatus LeNA, initial tests were performed to explore the possibility of creating subsurface modifications in silicon. Initially, the samples were observed under an infrared microscope, where traces of subsurface modifications were found. The process parameters for creating these modifications, had to be however, fine tuned. Initial results were published in 2012 [66] which was at that time, pioneering, as it was for the first time subsurface modifications were realised in silicon. There had been previous efforts (see section 1.2.2), but this was concentrated on the dicing application - where the laser beam was used to cut through the material. Further tests were performed to improve the quality of these modifications and the subsequent results were presented in 2014 [109].

With the built-in extendibility of LeNA, it was used to create volume modification in polycarbonates and special glasses, such as Foturan for research and industry applications. These are described in chapter 5. Since the pulse energy of the laser could be controlled between $5 - 50\,\mu J$, the process was optimised to create microstructures in softer materials such as those mentioned above. The automation of the instrument also meant that it could run for hours and sometimes, days to complete a certain task without human intervention. The lattice structure that was written in polycarbonate acrylic [110] and the 3D Computer Generated Volume Holograms [107] are prime examples of such processes. These structures required over 14-15 hours of write time.

6.1.4 3D polymer lithography for photonic applications

One of the aims of the project *Saphir*, which was a collaborative project at the University of Bremen, was to explore the possibility of optical on-chip communications and processing. This involved the fabrication, characterisation, and electronic adaptation of micro-optical structures either on or inside materials. For this purpose, the Photonic Professional from Nanoscribe was employed to create 3D Polymer Optical Waveguides (3DPOW) on glass substrates. These waveguides were between $250 - 270\,\mu m$ long and had a cross sectional diameter of $9\,\mu m$. The diameter was chosen to simulate similar condition as a single mode optical fibre. These waveguides were written in various configurations and geometries and were also optimised for mechanical and optical reproducibility, as described in chapter 4. They were optically characterised using the MONA set-up. Although, their the transmission losses in these waveguides were significant to be directly adapted into any set-up, they definitely demonstrated the capability of fabricating ultra-precise micro-scale optical waveguides that can be integrated with macro-scale fibre optics [96].

6.1.5 Optical Vector Matrix Multiplier

Another aim of the project *Saphir*, was to explore and demonstrate the possibility of basic building blocks for optical on-chip computation. For this purpose, a Vector Matrix Multiplier was proposed that accomplishes the basic algebraic matrix multiplication operation. The novelty of this idea was that it could be built and fabricated with very simple optoelectronic components, such as LEDs and LCDs; and yet demonstrate a method that could very well be the future of optical computing. As described in chapter 5, an all Optical Vector Matrix Multiplier (OVMM) was demonstrated which could perform a 3×3 multiplication of a binary vector and a binary matrix [111]. Improvements could be made here by using a custom ASIC and by fabricating the waveguides via lithographic techniques.

6.2 Future work - Optical Circuit Board

To combine the know-hows gained via all the above mentioned processes, results, and techniques, an Optical Circuit Board (OCB) is conceptualised. It proposes to turn to an alternative solution using the potential of three-dimensional design to fabricate optical interconnects that are closely integrated and fit well to optical and optoelectronic on-chip devices. The aim is to realise three-dimensional interconnect technologies for optoelectronic devices in the form of an OCB. Similar to an electronic printed board, a System on Chip (SoC) design demands an OCB. Unlike the conventional optical interconnects based on planar silicon waveguides, the design is based on glass which allows multiple optoelectronic device architectures to be integrated at one OCB that would have earlier been incompatible to each other. Alternate methods of realising three-dimensional optical interconnects in and on glass substrates is proposed, thereby offering better freedom of design compared to conventional planar waveguide technology. This technology enables the design of not just interconnects but also optical structures such as filters and gratings.

Designs of such components for the conceptualised OCB is proposed that will include a number of on-chip and subsurface structures and electronics, see figures 6.1 and 6.2. Many of the components, especially the on-chip microstructures are still a subject of research and therefore, the schematic along with the results presented in this work, serve the purpose of a guide for the further work in the field of on-chip optical computation. Figure 6.3 is an example of the envisaged opto-electronic circuit board where a Polymer Optical Waveguide in a Y-coupler configuration is fabricated with the methods mentioned in chapter 4 on an electronic printed circuit board.

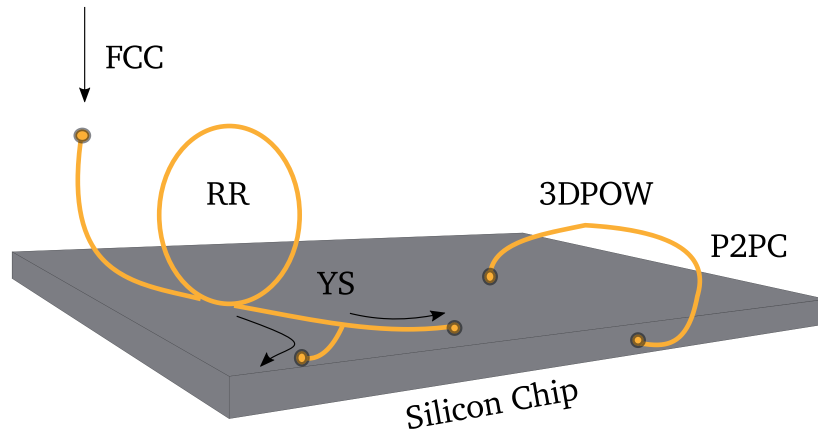

Figure 6.1: Schematic of a 3D Optical Circuit Board (OCB) realised via 3D Polymer Optical Waveguides (3DPOW) and subsurface optical waveguides. A ring resonator (RR) is realised by coupling in light via fibre chip coupling (FCC) and coupled out via a Y-splitter (YS). Similarly, a point to point connection (P2PC) is also made possible via 3DPOW to establish intra-chip and inter-chips optical interconnects.

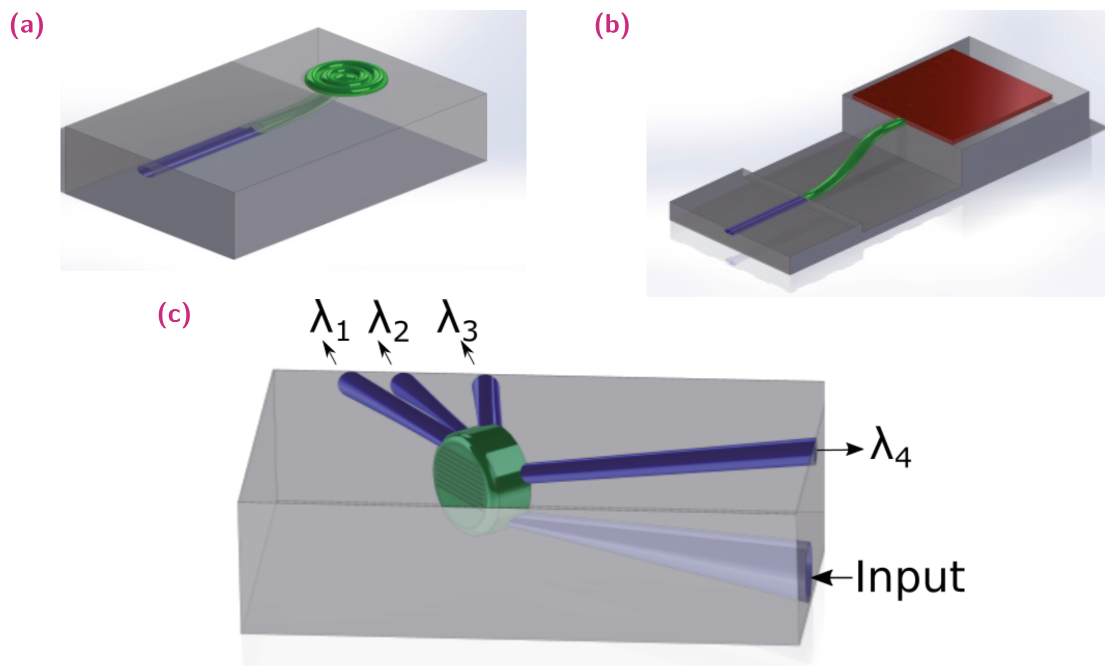

Figure 6.2: Schematics of the proposed prototypes as building blocks for optical on-chip computation. (a) 3DPOW (green) in combination with a subsurface waveguide (blue), designed to function as a free space vertical coupling structure via the 3DPOW grating. (b) Chip to Chip coupling. An edge emitting laser diode (red) is coupled with a subsurface waveguide (blue) via a 3DPOW (green). (c) 4-channel demultiplexer with 3D arrayed waveguide grating (green). An input signal is fed in via a buried waveguide that is integrated with an Arrayed Waveguide Grating (AWG) for wavelength division multiplexing. The individual output signals are then read coupled out via buried waveguides (blue).

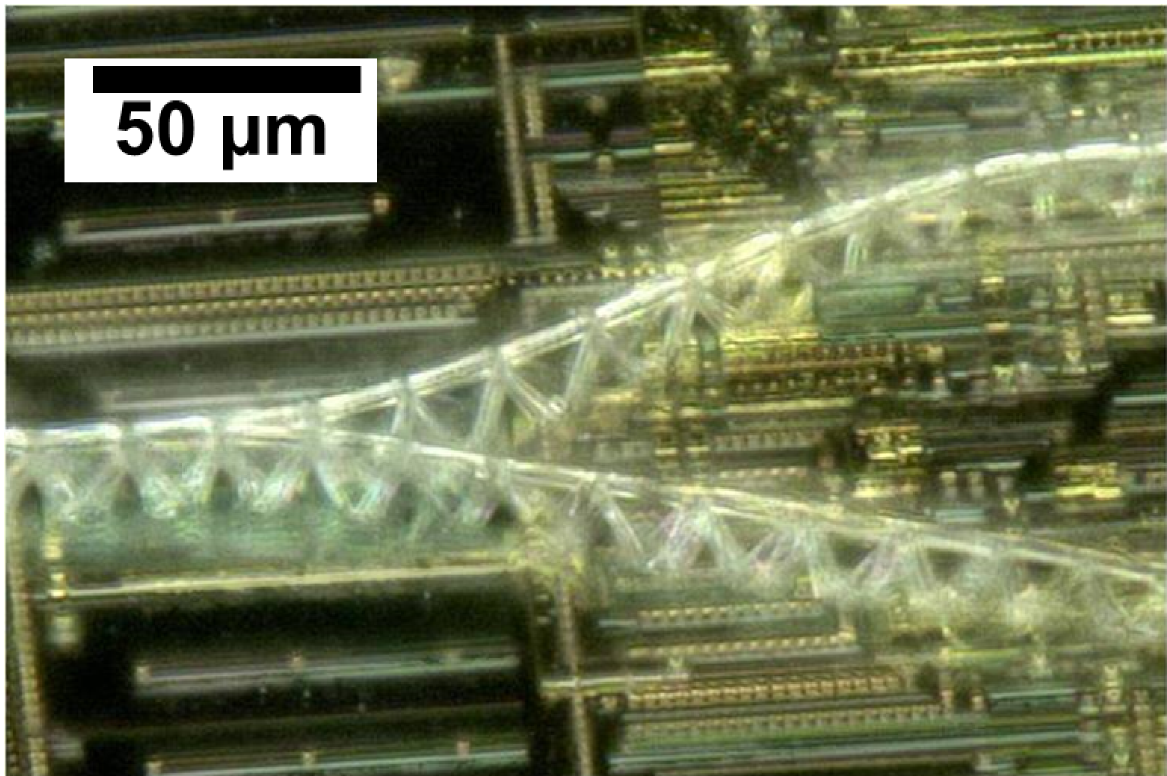

Figure 6.3: 3D Polymer Optical Waveguides in a Y-Coupler configuration fabricated on an electronic circuit board to demonstrate the tight integration capabilities of 3D lithography with the existing CMOS techniques.

Appendices

Technical specifications of LeNA

A

A.1 Laser system

The laser system uses is the commercially available Raydiance M50. The Raydiance Discovery USP Laser System is made up of the following major components:

1. Seed Box (see figure A.1)
2. Amplifier Box (see figure A.2)
3. Water chiller
4. Power Conditioning Unit

The seed box consists of a mode-locked, narrow bandwidth laser module; a first stage amplifier; a stretcher to increase the pulse width in the time domain; and a pulse picker to establish the base frequency. The low-power optical output from the seed box is connected to the amplifier using an optical fibre. The seed box and the laptop use a standard Ethernet connection to communicate between themselves.

The amplifier sub-assembly consists of three amplification stages, the compressor optics, and a pulse picker that defines the output frequency and duty cycle.

There is a single LED laser beam emission indicator on the front of the amplifier box. When the emission indicator is blinking the laser is ready for Class IV emission and all safety procedures must be applied. When the emission indicator is steady on the laser is emitting Class IV laser light. Note that the Class IIIa aim beam can be turned on during either of these states, in which case the indicator LED will assume the same status. When the aim beam is on but the laser is neither on or in the ready state, the LED emission indicator will be steady on.

The seed box and amplifier box are cooled using chilled water from the water chiller unit. The chiller hoses are connected to the rear panel of each box. The cooling water runs from the chiller to the seed box, then to the amplifier box, and finally back to the chiller. An RS-232 cable connects the chiller to the seed box and provides communication to the laser system on the status of the chiller relative to the start-up sequence. Chilled water

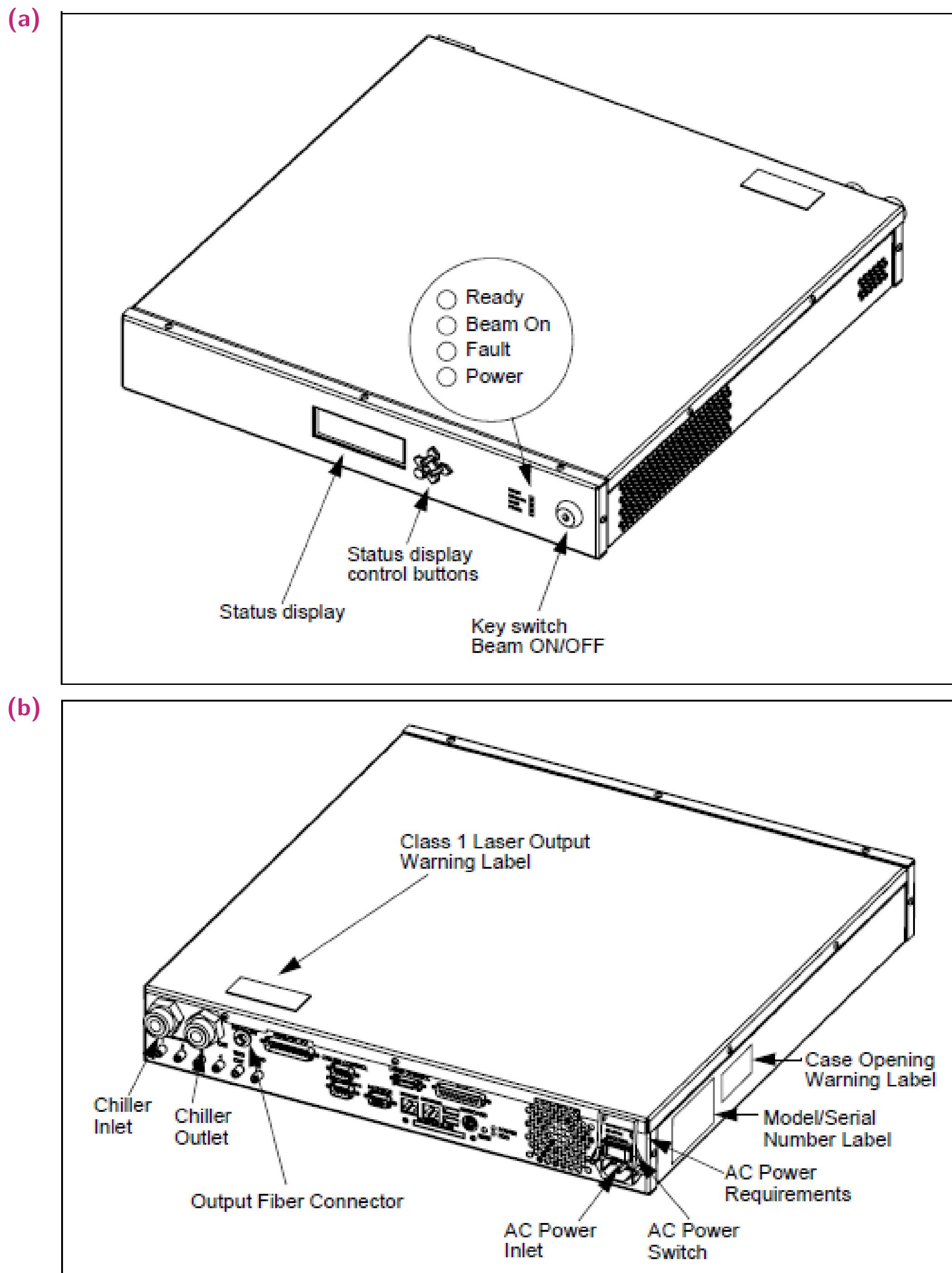

Figure A.1: Front and back side of the seed box. The seed box consists of a mode-locked seed laser and a stretcher to increase the pulse width of the beam, which is then sent to the amplifier box.

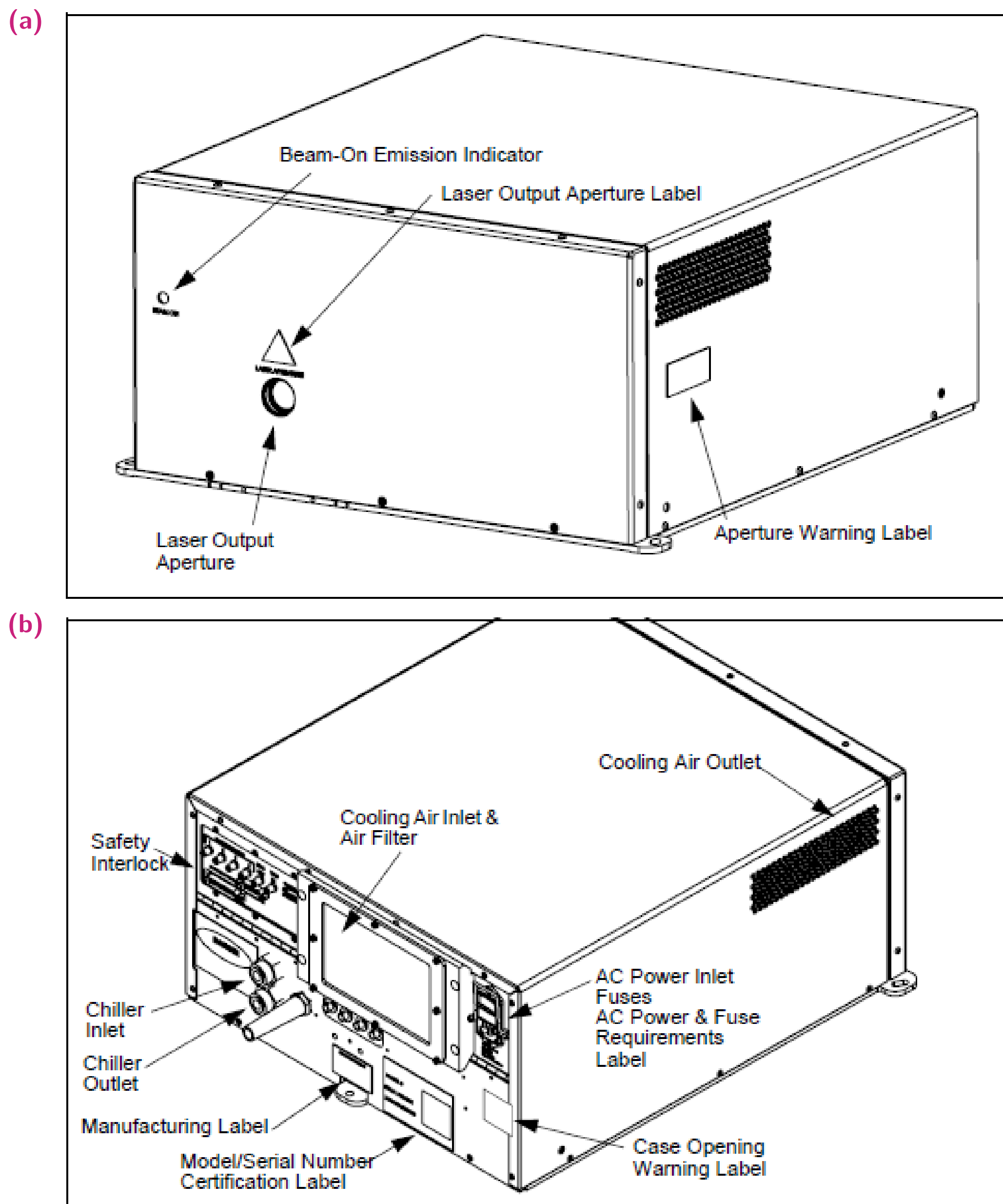

Figure A.2: The amplifier box, as the name suggests, amplifiers the signal coming from the seed box. The compressor and the other optics are electronically controlled. The output from the amplifier box is a class IV laser light.

is required to run the laser. Notifications and alarms will be provided through the user interface to guide corrective action, which will range from a start-up hold to a shut-down failure.

Two trigger input connectors provide for three separate trigger methods. The Main Trigger SMA connector accepts main trigger input. The Multi-purpose DB-25 connector has separate inputs for a de-bounced foot switch control and for general trigger inputs These triggers are tied together via logical "AND" and "OR" operational statements in the user interface and have a delay control through a numeric dialog. The foot switch is always "OR'd" with the other trigger inputs. The external triggers affect all laser operating modes and will take precedence over packet mode configurations; for example, terminating a packet when the external trigger is set false. The specification of the laser system is given in table A.1.

Table A.1: Specification Table for Raydiance M 50

Properties	Values
Wavelength	$1552\,nm$
Pulse duration	$< 800\,fs$
Pulse energy	$5 - 50\,\mu J$ (variable)
Repetition rate	$1\,Hz - 100\,kHz$ (variable)
M^2	1.2

A.2 User controls

The Joystick Bricklet from Tinkerforge can be used to extend the features of Bricks by joystick functionality. The Joystick is two directional and equipped with a push-button. It is mapped to have a dual velocity range for the stages. When it is pushed to upto 50% of its total travel range, the corresponding XY stage moves at a velocity of $5\,mm/s$. When pushed beyond that, the stage moves at $10\,mm/s$. A radius of 'no-travel' is mapped around it resting position so that tiny movements and disturbances do not jitter the motion stages.

The Dual Button Bricklet is equipped with two buttons and can extend Bricks. Both buttons have a built-in blue LED. You can read the current state of the button (pressed/released) and of the LED (on/off). You can turn the LED on/off yourself or enable auto-toggle. In auto-toggle mode the LEDs are toggled between on/off with each button press.

The Piezo Speaker Bricklet can be used to extend Bricks by the possibility to generate beeps with different frequencies. The available frequency range is 585Hz to 7100Hz. A beep has a configurable length and it is also possible to transmit a Morse Code string.

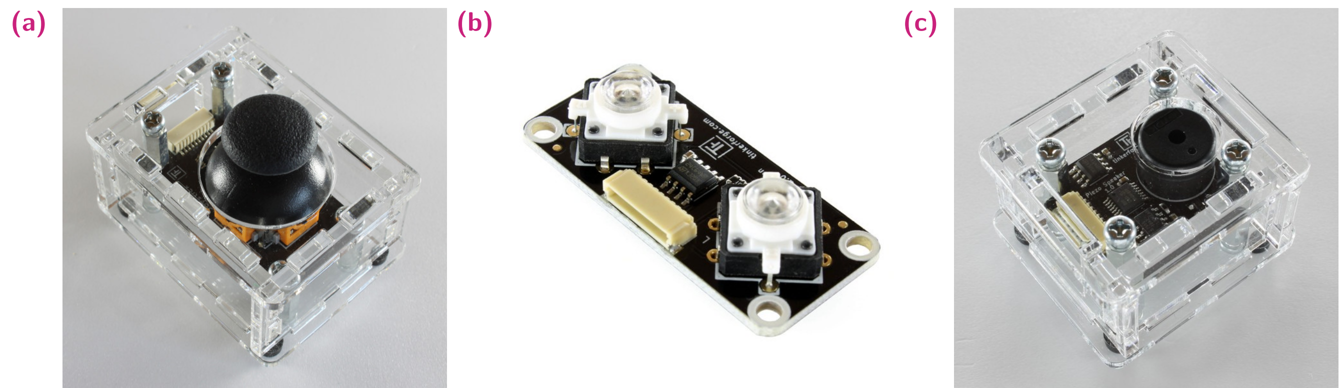

Figure A.3: (a) Joystick, (b) Dual Button, and (c) Piezo Speaker bricklets from Tinkerforge. These bricklets are connected to a Master Brick which is then connected to a computer via USB. The Master Brick can handle upto four bricklets simultaneously.

A.3 User interface: Raydiance M50

All controls for starting and stopping the laser, adjusting pulse characteristics, and monitoring system performance can be controlled via the Laser User Interface as shown in Figure A.4.

A.3.1 Status panel

Indicates the basic system state. After the system is powered up and the user interface is connected, the system attempts to achieve the standby state automatically. The status panel indicates the progress of the system. If an error occurs, the appropriate error code and message are displayed.

A.3.2 Control and measurement panel

Establishes the operating parameters for the laser based on repetition rate and pulse energy and also where the Aim Beam is controlled.

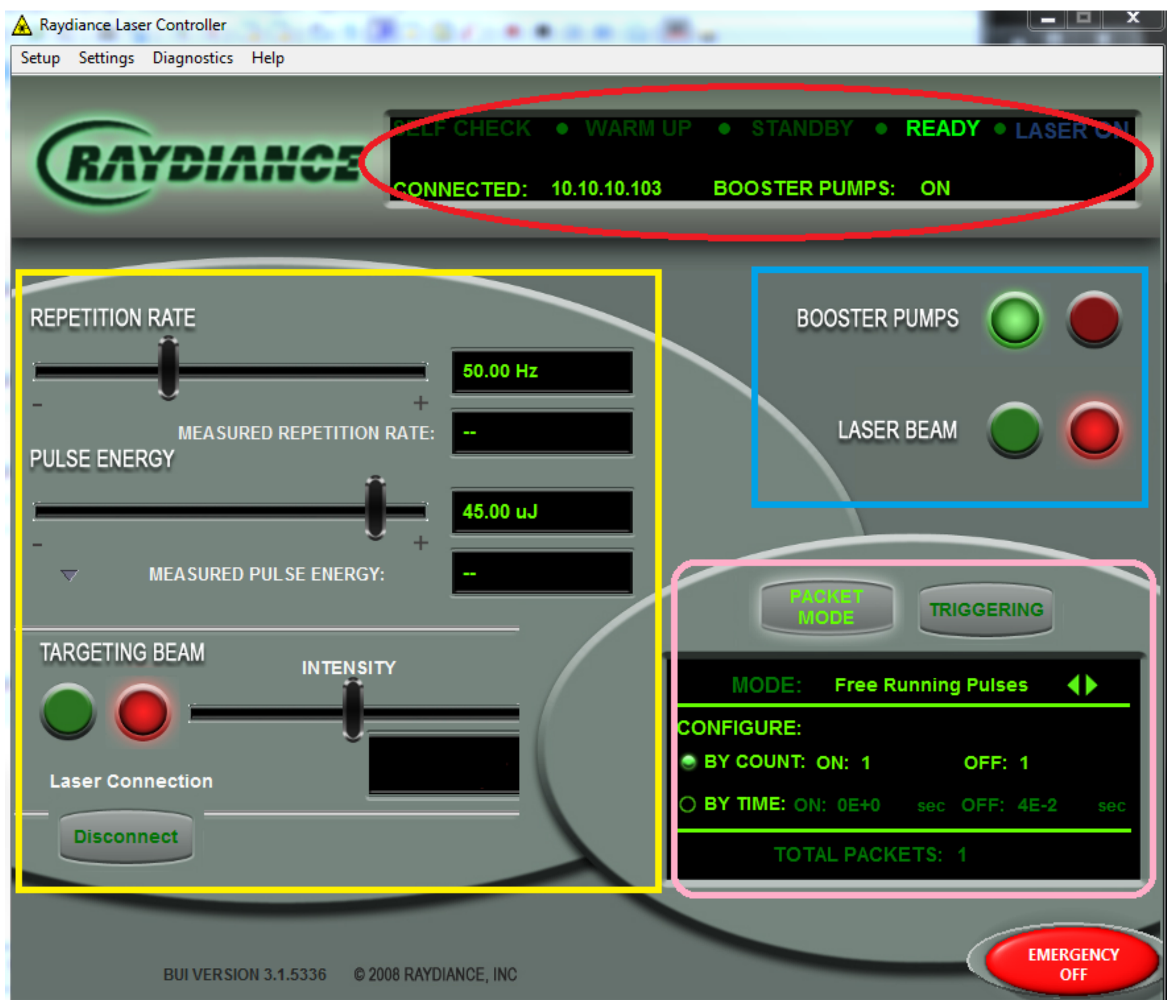

Figure A.4: User Interface for Laser control. Red: Status Panel. Yellow: Control and Measurement Panel. Blue: Pump and Beam Control. Pink: Packet Mode and Trigger

A.3.3 Pump and beam control

They are indicated by the colour-coded push button icons. The red buttons deactivates and the green button activates the Booster Pumps and the Laser Shutter.

A.3.4 Packet mode and trigger

The Packet Modes display allows the user to set various packet mode configurations. The Mode selector allows for 3 different modes: Free Running Pulses (normal operation), Free Running Packets, and Counted Packets. A packet is defined as a set of ON pulses and a set of OFF pulses. ON and OFF pulses are differentiated by gating through the AOM, which effectively acts a shutter. External triggering is enabled through the Enable Triggering check box. Multiple inputs and combinations for triggers are available by selecting different options in the Triggers window (figure A.5). All triggering occurs when the appropriate input signal is set low.

Figure A.5: Trigger Options on the Laser UI. LeNA is triggered via an auxiliary port. Therefore, the third option must be chosen. By default the trigger is in active low mode.

A.4 Fringe Processor

LeNA is centrally controlled via a plugin in Fringe Processor (FP). LeNA plugin can be started by choosing it from the *Plugin* drop down menu from the main FP window (see figure A.6). A brief overview of the plugin and this user manual can be accessed via the LeNA drop down menu once the plugin is loaded. Run time messages and errors are

displayed at the bottom of the UI. The CameraImage panel can be used to monitor or take images from a camera that is connected to the computer. LeNA is mainly controlled via the Tool Controls panel which is shown in greater detail in figure A.7.

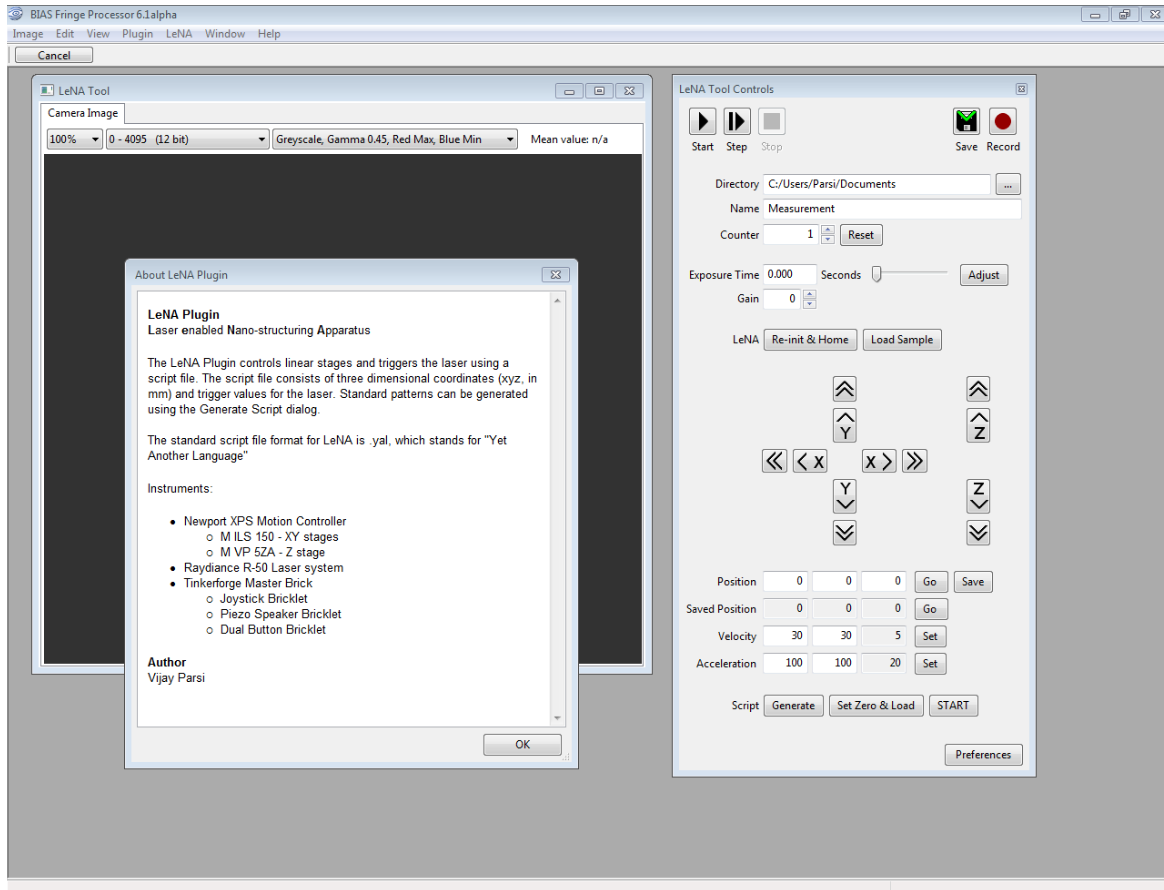

Figure A.6: LeNA plugin loaded in Fringe Processor

The following sections are each dedicated to a functionality in LeNA's user interface. The descriptions given here also serve as a user manual to someone who would like to use it in the future. The user interface is also programmed along with tool-tips where ever possible. This means that hovering over a button or an input field will display a message containing the description of the action that will be taken.

A.4.1 Re-init & Home

This button re-initialises the linear stages via the XPS motion controller and returns the stages to their home positions (0, 0, 0). All previously saved settings are cleared and set to default when this button is pressed. From the home position, the XY stages can move $75mm$ both in the negative and positive directions and the Z stage can move $2.4mm$ up and down.

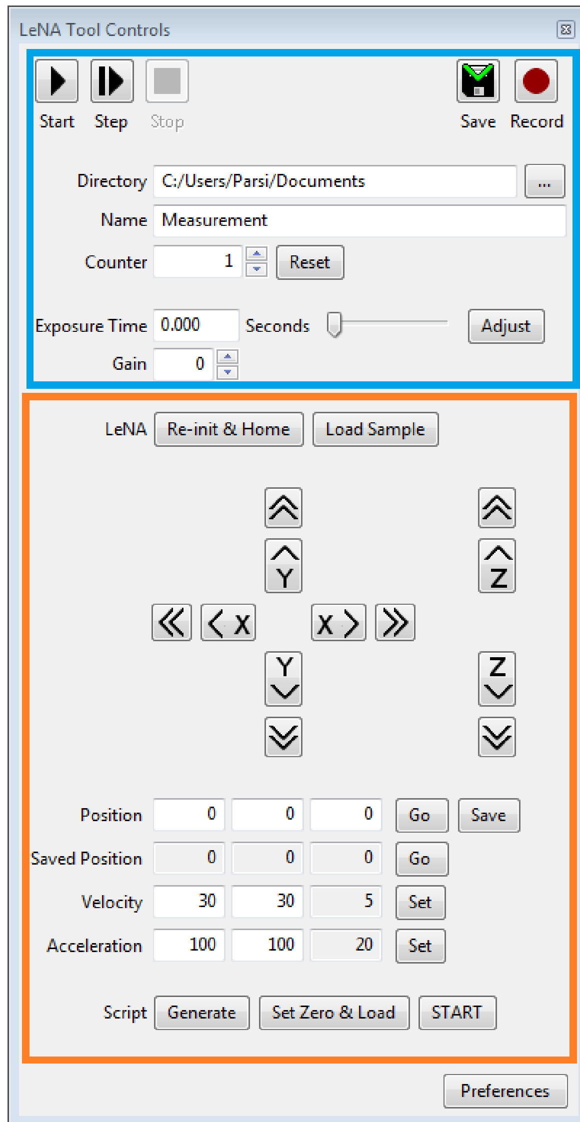

Figure A.7: LeNA Control Panel. Blue: Camera controls. Orange: LeNA controls. Hovering over any element on the user interface shows a tool-tip with corresponding information.

A.4.2 Load sample

This button moves the stages to the (-75, -75, 0) position to be able to load the sample. Before clicking this button, care should be taken to ensure that there are no obstacles for the stages to move.

A.4.3 On screen joystick

The XYZ stage combination can be controlled via on screen joystick. For the XY stages, buttons with a single arrow moves the corresponding stage at 5 mm/s velocity. Buttons with double arrows moves the stages with $20mm/s$ velocity. However, single arrowed Z axis buttons move the Z stage by a step of 10μm and the double arrowed buttons by a 100μm step.

A.4.4 Position

This field can be used to move the stage to a particular XYZ coordinate (mm), with the Go button. Save button is used to save the current position of the stages.

A.4.5 Saved position

This field displays the saved coordinates of the stage via the Save button. The fields cannot be manually altered and can only be edited via the Save button. The Go Button moves the stage to the saved position.

A.4.6 Velocity

This field can be used to set the stage velocities in mm/s. The Z stage velocity is fixed and cannot be altered. Default values are 30, 30, and 5.

A.4.7 Acceleration

This field can be used to set the stage accelerations in mm/s^2. The Z stage acceleration is fixed and cannot be altered. Default values are 100, 100, and 20.

A.4.8 Generate

This button opens up a dialog to generate yal scripts in meander, gratings and spiral forms. A yal script can generated and saved by filling up appropriate values in the dialog as shown in figure A.8. To create custom structures and design, the yal scripting language can be used. A complete manual is given in appendix B.

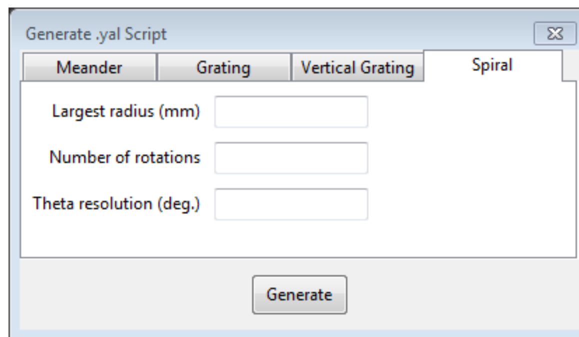

Figure A.8: The Script Generation dialog for LeNA UI enables the user to generate four different kinds of structures with custom parameters. Eg: a Spiral can be generated by inputting a few parameters.

A.4.9 Set zero & load

This button sets the current positions of the stages to a *virtual zero* and prompts the user to load a yal script to be written. The script should be selected and loaded only after moving the stages to an appropriate position. Changing the position after loading the script might produce errors.

A.4.10 Start

This button starts the writing process. The laser should be set to external trigger mode, if needed, as shown in figure A.5. All laser safety precautions must be fulfilled before pressing this button.

.yal File Format

B

Yet Another Language (yal) is the script file format for LeNA.
The script file must have *.yal* as the file extension, else it will not be recognised.

B.1 Syntax

The following is a list of commands and allowed syntax for the script file.

CR + LF

A .yal file can be created and edited with any standard text editor (suggested: Notepad++), with MS-Windows style newline character.

XYZ position

To move the XYZ stage configuration to a particular point in 3D coordinate space, the XYZ coordinates are simply written down in mm units.

```
% XYZ entries
4          3          1.2
```

Decimal mark

Decimal places are denoted via a *dot* character. Using a *comma* will cause errors. This must be taken into consideration, especially while creating .yal scripts from a non-English system.

Since the values are input in mm, the need for digit grouping does not arise. In any case, the values should be written as-is without digit groupings.

```
% Correct decimal marks
23.4        44.01        1.34
```

```
% Incorrect decimal marks
23,4        44,01        1,34
```

Delimiter

The position entries in the file are *always* separated by a tab character which cannot be replaced by white space or double-tab, etc.

```
% Tab spaced entries
0        0        0
```

```
% Non-tab spaced entries
0 0 0
```

Empty lines

Empty lines are allowed in the script file for better readability but are not necessary. However, they should not contain white-space characters.

Comments

If a line begins with a % character, it is ignored.

You can also include comments in the middle of a line but it is highly discouraged and may produce errors.

```
% This is a good comment line
0        0        0
```

```
0          0          0 % This is a bad comment line
```

Z - direction

When writing a 3D structure, it is recommended that the Z values decrease with each step from the beginning to the end of the file. This ensures that the structures is being written from bottom to top and hence avoids interference of the focussed laser beam with the already written structure.

An example of this can be found in Section B.2.

Laser control

The laser can be switched ON and OFF from the script, by using the following commands.

NOTE: The words are single space separated and NOT tab spaced, in this case.

```
# laser on
```

and

```
# laser off
```

Stage velocities and accelerations

The XY linear stages velocities and accelerations can be controlled via .yal script using the following commands. The velocity and acceleration for the Z axis is set automatically and *cannot* be set manually. If the values for X and Y are not specified, then the default values will be loaded, as shown in Table B.1.

NOTE: The words are single space separated and NOT tab spaced, in this case.

```
% Setting x = 50 mm/s and y = 70 mm/s
# set v 50 70
```

and

```
% Setting x = 100 mm/s^2 and y = 130 mm/s^2
# set a 100 130
```

Table B.1: Default Values for Stage Velocities and Accelerations

Stages →	X & Y	Z
Velocity	30 mm/s	5 mm/s
Acceleration	100 mm/s^2	20 mm/s^2

Including .yal scripts in a .yal script

Scripts can be loaded within a main script by using the include command. This is useful when writing a matrix of the same structure with or without varying parameters. However, the include command can *only* be used from the main file and not from the included files. In other words, the inclusion can only be one-level deep.

IMP: The included file *cannot* have spaces in its file name.

NOTE: The words are single space separated and NOT tab spaced, in this case.

```
# include subYALfile.yal
```

B.2 Minimum Working Examples

B.2.1 A simple .yal Script

Filename: simple.yal

```
% Writing three parallel lines 10 mm long in X direction
% with spacing of 5 mm in Y direction and
% a separation of 200 µm in the Z direction.

# laser off
0         0         0
# laser on
10         0         0
# laser off
```

```
0         5         -0.2
# laser on
10         5         -0.2
# laser off
0         10         -0.4
# laser on
10         10         -0.4
# laser off
```

B.2.2 A .yal script calling other .yal scripts

From Section B.2.1, include the file `simple.yal` twice with different stage parameters.

```
% When this file is loaded, the positions in simple.yal are
% calculated relative to the coordinates given in this file.
% This file sets 0 and global coordinates for the process.

# set a 100 100
# set v 50 50
0         0         0
# include simple.yal
# set a 120 120
# set v 70 70
20         0         0
# include simple.yal
```

C

Technical Specifications of OVMM Components

C.1 LED

The single colour 1101W series LEDs have a 3216 Type water-clear-resin packaging. It has GaAlAs as the die material and a peak wavelength of $647nm$. A few more specifications, including its electric and optical properties are given in figure C.1, taken from its datasheet.

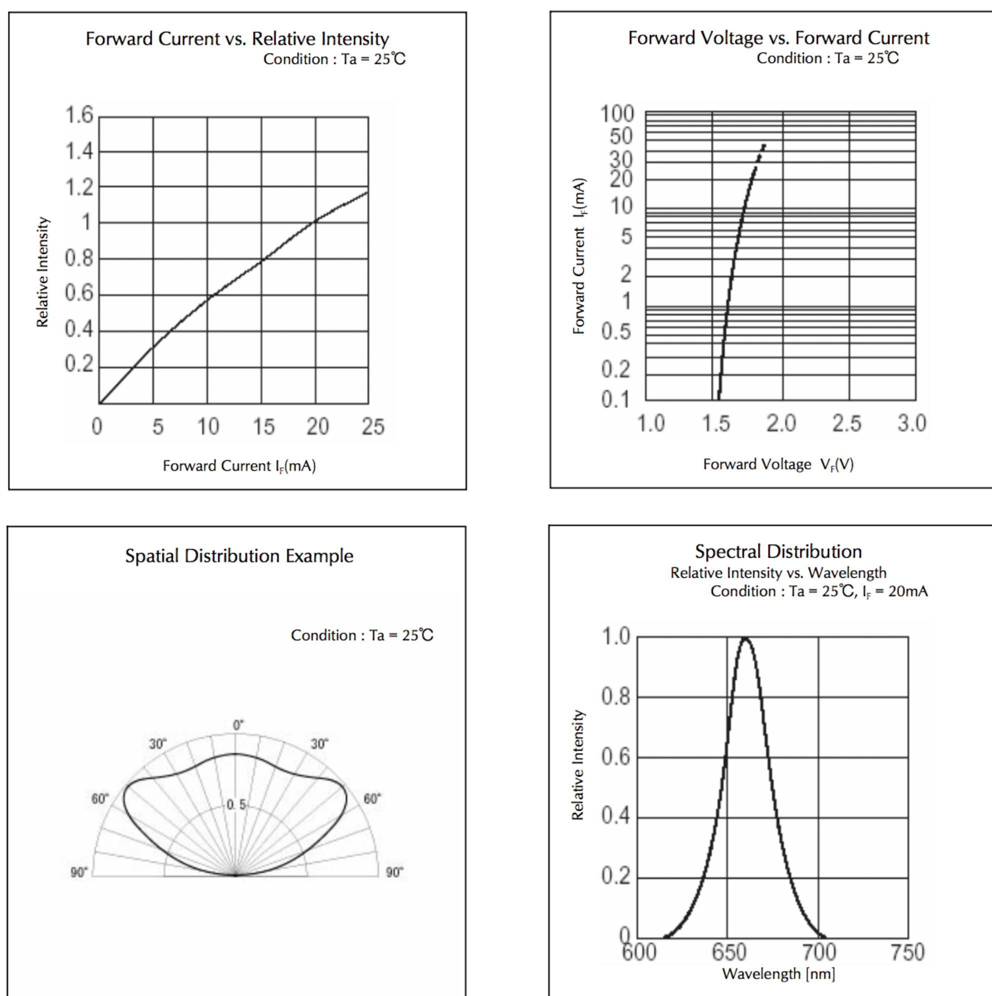

Figure C.1: Electric and optical specifications of the 1101W series GaAlAs LED with a peak wavelength of $647nm$

C.2 Photodiode

BPW34 is a PIN photodiode with high speed and high radiant sensitivity in miniature, flat, top view, clear plastic package. It is sensitive to visible and near infrared radiation. Its electric and optical properties are given in figure C.2, taken from its datasheet.

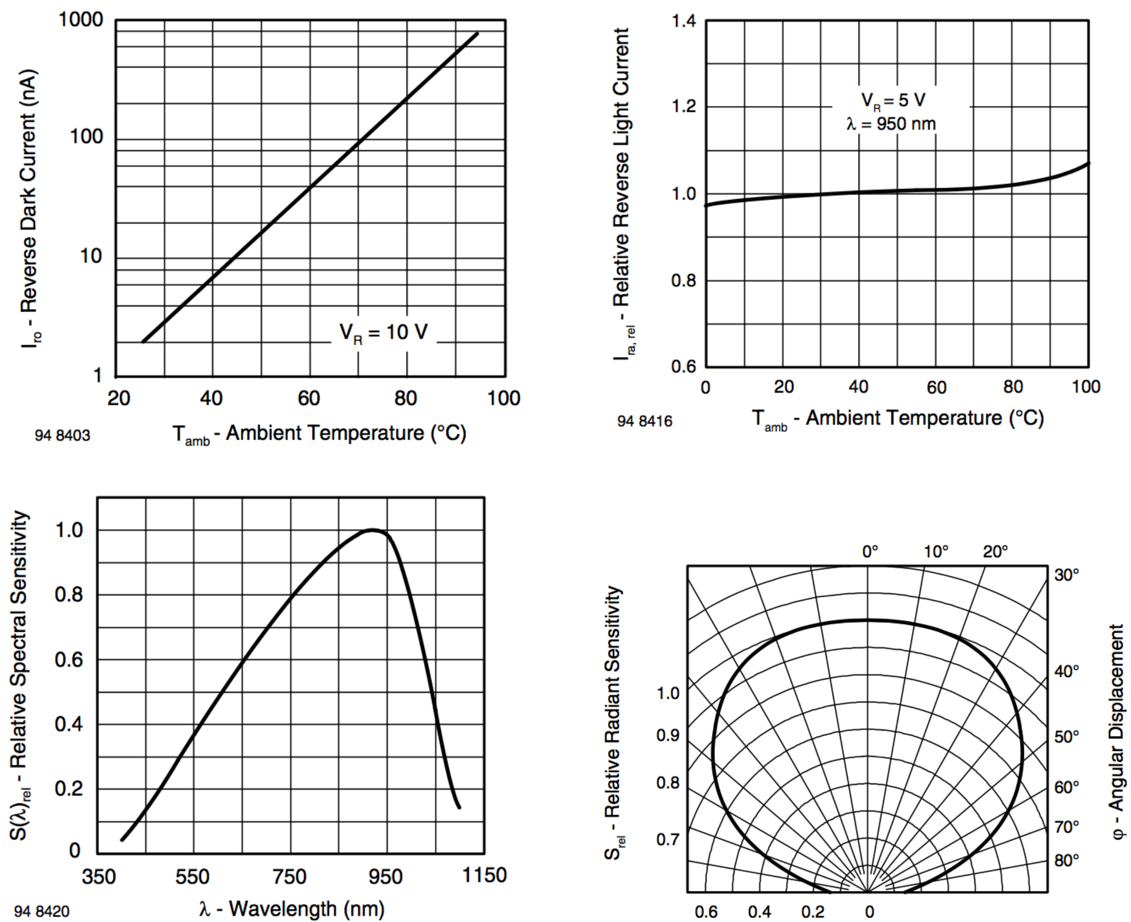

Figure C.2: Electric and optical specifications of the BPW34 photodiode.

C.3 Arduino microcontroller

An Arduino Uno board consists of an Atmel 8 bit AVR microcontroller (ATmega328P) with complementary components that facilitate programming and incorporation into other circuits (Figure C.3). The board exposes most of the microcontroller's I/O pins for use by other circuits. The microcontroller is programmed with C/C++. It is, however, usually programmed with its own IDE (Integrated Development Environment) that uses the *Wiring* library to simplify the code. Some of its specifications are given in table C.1.

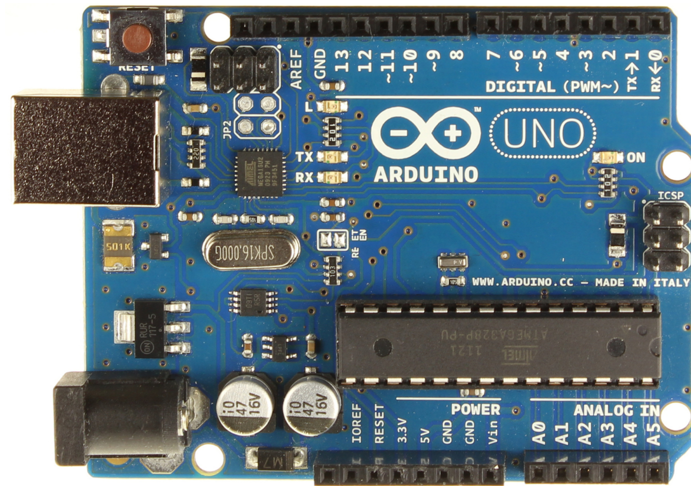

Figure C.3: An Arduino Uno Board - an open source microcontroller platform used for rapid prototyping with an ATMEGA328P microcontroller.

Table C.1: Specifications table of the Arduino Uno

Specification	Value
Operating Voltage	$5V$
Digital I/O Pins	14 (of which 6 provide PWM output)
PWM Digital I/O Pins	6
Analog Input Pins	6
DC Current per I/O Pin	$20mA$
DC Current for 3.3V Pin	$50mA$
Flash Memory	$32KB$ of which $0.5KB$ used by bootloader
Clock Speed	$16MHz$

Bibliography

[1] A. Einstein. 'Zur Quantentheorie der Strahlung'. *Physikalische Zeitschrift* 18 (1917) (cit. on p. 1).

[2] T. H. Maiman. 'Stimulated Optical Radiation in Ruby'. *Nature* 187 (1960) (cit. on p. 1).

[3] Y.-Y. Liu, J. Stehlik, C. Eichler, M. J. Gullans, J. M. Taylor, and J. R. Petta. 'Semiconductor double quantum dot micromaser'. *Science* 347 (2015) (cit. on p. 1).

[4] Lawrence Livermore National Laboratory. *https://www.llnl.gov/news/petawatt-laser-system-passes-key-milestone*. 2016 (cit. on p. 1).

[5] A. E. Siegman. 'Defining, measuring, and optimizing laser beam quality'. Ed. by A. Bhowmik. International Society for Optics and Photonics, 1993 (cit. on p. 5).

[6] A. Javan, W. R. Bennett, and D. R. Herriott. 'Population Inversion and Continuous Optical Maser Oscillation in a Gas Discharge Containing a He-Ne Mixture'. *Physical Review Letters* 6 (1961) (cit. on p. 6).

[7] R. Paschotta. *RP Photonics*. 2016 (cit. on p. 8).

[8] M. G. A. Bernard and G. Duraffourg. 'Laser Conditions in Semiconductors'. *physica status solidi (b)* 1 (1961) (cit. on p. 8).

[9] J. Shah. *Ultrafast spectroscopy of semiconductors and semiconductor nanostructures*. 2nd ed. Springer, 1999 (cit. on p. 10).

[10] J.-C. Diels and W. Rudolph. *Ultrashort laser pulse phenomena : fundamentals, techniques, and applications on a femtosecond time scale*. Elsevier/Academic Press, 2006 (cit. on p. 10).

[11] M. D. Fayer. *Ultrafast infrared vibrational spectroscopy*. CRC Press, 2013 (cit. on p. 10).

[12] J. H. Chu, O. Voskoboynikov, and C. Lee. 'Slow light in photonic crystals'. *Microelectronics Journal* 36 (2005) (cit. on p. 10).

[13] T. Baba. 'Slow light in photonic crystals'. *Nature Photonics* 2 (2008) (cit. on p. 10).

[14] H. Yu, B. Li, and X. Zhang. ‘Flexible fabrication of three-dimensional multi-layered microstructures using a scanning laser system’. *Sensors and Actuators, A: Physical* 125 (2006) (cit. on p. 10).

[15] M. Malinauskas. ‘Fabrication of 3D micro-structured scaffolds by direct laser writing in pre-polymers for in vitro and in vivo studies’. *Proc. SPIE SPIE* (2017) (cit. on p. 10).

[16] J. Leuthold, C. Koos, and W. Freude. ‘Nonlinear silicon photonics’. *Nature Photonics* 4 (2010) (cit. on p. 10).

[17] H.-H. Gatzen, V. Saile, and J. Leuthold. *Micro and nano fabrication : tools and processes*. 2015 (cit. on p. 10).

[18] M. Göppert-Mayer. ‘Über Elementarakte mit zwei Quantensprüngen’. *Annalen der Physik* 401 (1931) (cit. on p. 10).

[19] D. Boggett and R. Loudon. ‘Theory of Two-Photon Absorption by Polaritons’. *Physical Review Letters* (1972) (cit. on p. 10).

[20] M. D. Burrows and W. R. Salzman. ‘Semiclassical theory of two-photon absoprtion: Absorption and level shifts in a model system’. *Physical Review A* 15 (1977) (cit. on p. 10).

[21] Y. B. Band. *Light and matter : electromagnetism, optics, spectroscopy and lasers*. John Wiley, 2006 (cit. on p. 11).

[22] W. Kaiser and C. G. B. Garrett. ‘Two-Photon Excitation in CaF2:Eu2+’. *Physical Review Letters* 7 (1961) (cit. on p. 11).

[23] W. Denk, J. H. Strickler, and W. W. Webb. ‘Two-Photon Laser Scanning Fluorescence Microscopy’. *Science, New Series* 248 (1990) (cit. on p. 11).

[24] D. A. Parthenopoulos and P. M. Rentzepis. ‘Three-dimensional optical storage memory.’ *Science (New York, N.Y.)* 245 (1989) (cit. on p. 11).

[25] M. Drobizhev and M. ‘Applications of Two-Photon Absorption in Medicine and Biology Enabled by Specially Designed Biological Molecules’. *American Physical Society, 10th Annual Meeting of the Northwest Section of APS* (2008) (cit. on p. 12).

[26] H.-C. Kim, S. Kreiling, S. Haertner, L. Hesse, A. Greiner, and N. A. Hampp. ‘Two-photon absorption-induced drug delivery from polymers for medical applications’. *Proc. SPIE 5323, Multiphoton Microscopy in the Biomedical Sciences IV, 327*. Vol. 5323. 2004 (cit. on p. 12).

[27] K. Yamasaki, S. Juodkazis, M. Watanabe, H.-B. Sun, S. Matsuo, and H. Misawa. ‘Recording by microexplosion and two-photon reading of three-dimensional optical memory in polymethylmethacrylate films’. *Applied Physics Letters* 76 (2000) (cit. on p. 12).

[28] M. Fischer, T. Ye, G. Yurtsever, and A. Miller. ‘Two-photon absorption and self-phase modulation measurements with shaped femtosecond laser pulses’. *Optics letters* 30 (2005) (cit. on pp. 12, 37).

[29] D. L. Andrews. *Lasers in Chemistry*. Berlin, Heidelberg: Springer Berlin Heidelberg, 1990 (cit. on p. 12).

[30]M. Schade, O. Varlamova, J. Reif, H. Blumtritt, W. Erfurth, and H. S. Leipner. 'High-resolution investigations of ripple structures formed by femtosecond laser irradiation of silicon'. *Analytical and Bioanalytical Chemistry* 396 (2010) (cit. on p. 13).

[31]K. Furuya and T. Saito. 'In situ microlithography of Si and GaAs by a focused ion beam in a 200 keV TEM'. *Journal of electron microscopy* 45 (1996) (cit. on p. 13).

[32]P. C. Verburg, G. R. B. E. Römer, and a. J. Huis In 't Veld. 'Two-photon-induced internal modification of silicon by erbium-doped fiber laser.' *Optics express* 22 (2014) (cit. on p. 13).

[33]D. J. Hwang, C. P. Grigoropoulos, and T. Y. Choi. 'Efficiency of silicon micromachining by femtosecond laser pulses in ambient air'. *Journal of Applied Physics* 99 (2006) (cit. on p. 13).

[34]Y. P. Deng, X. H. Xie, H. Xiong, Y. X. Leng, C. F. Cheng, H. H. Lu, R. X. Li, and Z. Z. Xu. 'Optical breakdown for silica and silicon with double femtosecond laser pulses.' *Optics express* 13 (2005) (cit. on p. 13).

[35]S. Ameer-Beg, W. Perrie, S. Rathbone, J. Wright, W. Weaver, and H. Champoux. 'Femtosecond laser microstructuring of materials'. *Applied Surface Science* 127-129 (1998) (cit. on p. 13).

[36]J. Koch. 'Direct-write subwavelength structuring with femtosecond laser pulses'. *Optical Engineering* 44 (2005) (cit. on p. 13).

[37]M. Amer, M. El-Ashry, L. Dosser, K. Hix, J. Maguire, and B. Irwin. 'Femtosecond versus nanosecond laser machining: comparison of induced stresses and structural changes in silicon wafers'. *Applied Surface Science* 242 (2005) (cit. on p. 13).

[38]A. Joglekar, H. Liu, G. Spooner, E. Meyhöfer, G. Mourou, and A. Hunt. 'A study of the deterministic character of optical damage by femtosecond laser pulses and applications to nanomachining'. *Applied Physics B: Lasers and Optics* 77 (2003) (cit. on p. 13).

[39]C. B. Schaffer, A. O. Jamison, and E. Mazur. 'Morphology of femtosecond laser-induced structural changes in bulk transparent materials'. *Applied Physics Letters* 84 (2004) (cit. on p. 13).

[40]C. B. Schaffer, A. Brodeur, and E. Mazur. 'Laser-induced breakdown and damage in bulk transparent materials induced by tightly focused femtosecond laser pulses'. *Measurement Science and Technology* 12 (2001) (cit. on p. 13).

[41]S.-H. Cho. 'Laser Micromachining of Active and Passive Photonic Integrated Circuits'. PhD thesis. MIT, 2003 (cit. on p. 13).

[42]R. Ahmad, M. Rochette, and C. Baker. 'Fabrication of Bragg gratings in subwavelength diameter As2Se3 chalcogenide wires.' *Optics letters* 36 (2011) (cit. on p. 13).

[43]R. Mehra, S. Jaiswal, and H. K. Dixit. 'Optical computing with semiconductor optical amplifiers'. *Optical Engineering* 51 (2012) (cit. on p. 13).

[44] W. S. Zaoui, A. Kunze, W. Vogel, M. Berroth, J. Butschke, F. Letzkus, and J. Burghartz. 'Bridging the gap between optical fibers and silicon photonic integrated circuits.' *Optics express* 22 (2014) (cit. on p. 13).

[45] L. Brusberg, H. Schröder, R. Erxleben, I. Ndip, M. Töpper, N. F. Nissen, and H. Reichl. 'Glass Carrier Based Packaging Approach Demonstrated on a Parallel Optoelectronic Transceiver Module for PCB Assembling'. *Electronic Components and Technology Conference (ECTC), 2010 Proceedings 60th* (2010) (cit. on pp. 13, 17).

[46] A. Krishnamoorthy, H. Schwetman, P. Koka, I. Shubin, and J. Cunningham. 'Computer Systems Based on Silicon Photonic Interconnects'. *Proceedings of the IEEE* 97 (2009) (cit. on p. 13).

[47] D. a. B. Miller. 'Optical interconnects to electronic chips.' *Applied optics* 49 (2010) (cit. on p. 13).

[48] O. Bass, A. Meiri, Z. Zalevsky, and A. Fish. 'Photonic XOR with inherent loss compensation mechanism for memory cell implementation in a standard nanoscale very large-scale integrated fabrication process.' *Optics letters* 38 (2013) (cit. on p. 14).

[49] W. Watanabe, T. Tamaki, and K. Itoh. 'Femtosecond laser micromachining and biological therapy'. *Laser Physics* 18 (2011) (cit. on p. 14).

[50] Y. Bellouard, A. Said, M. Dugan, and P. Bado. 'Fabrication of high-aspect ratio, micro-fluidic channels and tunnels using femtosecond laser pulses and chemical etching.' *Optics express* 12 (2004) (cit. on p. 14).

[51] G. Cheng, Y. Wang, J. D. White, Q. Liu, W. Zhao, and G. Chen. 'Demonstration of high-density three-dimensional storage in fused silica by femtosecond laser pulses'. *Journal of Applied Physics* 94 (2003) (cit. on p. 14).

[52] M. Malinauskas, M. Farsari, A. Piskarskas, and S. Juodkazis. 'Ultrafast laser nanostructuring of photopolymers : A decade of advances'. *Physics Reports* 533 (2013) (cit. on p. 14).

[53] F. Fukuyo, K. Fukumitsu, and N. Uchiyama. 'Stealth dicing technology and applications'. *Proceedings of 6th International Symposium on Laser Precision Microfabrication* (2005) (cit. on p. 14).

[54] K. Venkatakrishnan and B. Tan. 'Thin silicon wafer dicing with a dual-focused laser beam'. *Journal of Micromechanics and Microengineering* 17 (2007) (cit. on p. 14).

[55] K. Venkatakrishnan, N. Sudani, and B. Tan. 'A high-repetition-rate femtosecond laser for thin silicon wafer dicing'. *Journal of Micromechanics and Microengineering* 18 (2008) (cit. on p. 14).

[56] P. C. Verburg, G. R. B. E. Römer, and A. J. Huis In 'T Veld. 'Two-temperature model for pulsed-laser-induced subsurface modifications in Si'. *Applied Physics A: Materials Science and Processing* (2014) (cit. on p. 14).

[57] N. Bärsch and K. Körber. 'Ablation and cutting of planar silicon devices using femtosecond laser pulses'. *Applied Physics A: Materials Science and Processing* 242 (2003) (cit. on p. 14).

[58] Hamamatsu. *Stealth Dicing Technical Information for MEMS*. 2014 (cit. on p. 15).

[59] E. Ohmura, F. Fukuyo, K. Fukumitsu, and H. Morita. ‘Internal modified-layer formation mechanism into silicon with nanosecond laser’. *Journal of Achievements in Materials and Manufacturing Engineering* 17 (2006) (cit. on p. 15).

[60] P. Romero, N. Otero, I. Coto, C. Leira, and A. González. ‘Experimental Study of Diode Laser Cutting of Silicon by Means of Water Assisted Thermally Driven Separation Mechanism’. *Physics Procedia* 41 (2013) (cit. on p. 16).

[61] H. Schroder, L. Brusberg, R. Erxleben, I. Ndip, M. Topper, N. F. Nissen, and H. Reichl. ‘glassPack — A 3D glass based interposer concept for SiP with integrated optical interconnects’. *2010 Proceedings 60th Electronic Components and Technology Conference (ECTC)*. IEEE, 2010 (cit. on p. 17).

[62] H. Schroder, L. Brusberg, R. Erxleben, I. Ndip, M. Topper, N. F. Nissen, and H. Reichl. ‘glassPack — A 3D glass based interposer concept for SiP with integrated optical interconnects’. *2010 Proceedings 60th Electronic Components and Technology Conference (ECTC)*. IEEE, 2010 (cit. on p. 17).

[63] S. Thompson and S. Parthasarathy. ‘Moore’s law: the future of Si microelectronics’. *Materials Today* 9 (2006) (cit. on p. 18).

[64] K. Ramani, N. Muralimanohar, and R. Balasubramonian. ‘Microarchitectural techniques to reduce interconnect power in clustered processors’. *Proc. of the Workshop on Complexity Effective Design*. 2004 (cit. on p. 18).

[65] D. A. B. Miller. ‘Optical interconnects to electronic chips’. *Applied Optics* 49 (2010) (cit. on p. 18).

[66] V. V. Parsi Sreenivas, M. Bülters, and R. B. Bergmann. ‘Microsized subsurface modification of mono-crystalline silicon via non-linear absorption’. *Journal of the European Optical Society* 12035 (2012) (cit. on pp. 18, 58, 59, 100).

[67] A. Di Falco, S. C. Kehr, and U. Leonhardt. ‘Luneburg lens in silicon photonics’. *Optics Express* 19 (2011) (cit. on p. 18).

[68] S. Assefa, S. Shank, W. Green, M. Khater, E. Kiewra, C. Reinholm, S. Kamlapurkar, A. Rylyakov, C. Schow, F. Horst, H. Pan, T. Topuria, P. Rice, D. M. Gill, J. Rosenberg, T. Barwicz, M. Yang, J. Proesel, J. Hofrichter, B. Offrein, X. Gu, W. Haensch, J. Ellis-Monaghan, and Y. Vlasov. ‘A 90nm CMOS integrated Nano-Photonics technology for 25Gbps WDM optical communications applications’. *2012 International Electron Devices Meeting*. IEEE, 2012 (cit. on p. 18).

[69] HELIOS. *State of the art on Photonics on CMOS, 3rd update*. Tech. rep. 2012 (cit. on p. 18).

[70] IBM. *http://www-03.ibm.com/press/us/en/pressrelease/39641.wss*. 2012 (cit. on p. 18).

[71] I. Fraunhofer. *http://www.ipms.fraunhofer.de/en/press-media/press/2014/2014-06-16.html*. 2014 (cit. on p. 18).

[72] C. Kittel. *Introduction to solid state physics*. Wiley, 2005 (cit. on pp. 23, 26).

[73]Y. Okada and Y. Tokumaru. ‘Precise determination of lattice parameter and thermal expansion coefficient of silicon between 300 and 1500 K’. *Journal of Applied Physics* 56 (1984) (cit. on p. 24).

[74]L. Vegard. ‘Die Konstitution der Mischkristalle und die Raumfuellung der Atome’. *Zeitschrift fuer Physik* 5 (1921) (cit. on p. 24).

[75]D. Windisch and P. Becker. ‘Silicon lattice parameters as an absolute scale of length for high precision measurements of fundamental constants’. *physica status solidi (a)* 118 (1990) (cit. on p. 24).

[76]R. D. Deslattes, A. Henins, H. A. Bowman, R. M. Schoonover, C. L. Carroll, I. L. Barnes, L. A. Machlan, L. J. Moore, and W. R. Shields. ‘Determination of the Avogadro Constant’. *Physical Review Letters* 33 (1974) (cit. on p. 24).

[77]R. D. Deslattes, A. Henins, R. M. Schoonover, C. L. Carroll, and H. A. Bowman. ‘Avogadro Constant—Corrections to an Earlier Report’. *Physical Review Letters* 36 (1976) (cit. on p. 24).

[78]R. D. Deslattes. ‘The Avogadro Constant’. *Annual Review of Physical Chemistry* 31 (1980) (cit. on p. 24).

[79]G. Cavagnero, H. Fujimoto, G. Mana, E. Massa, K. Nakayama, and G. Zosi. ‘Measurement repetitions of the Si(220) lattice spacing’. *Metrologia* 41 (2004) (cit. on p. 24).

[80]P. Becker, H. Friedrich, K. Fujii, W. Giardini, G. Mana, A. Picard, H.-J. Pohl, H. Riemann, and S. Valkiers. ‘The Avogadro constant determination via enriched silicon-28’. *Measurement Science and Technology* 20 (2009) (cit. on p. 24).

[81]E. Massa, G. Mana, U. Kuetgens, and L. Ferroglio. ‘Measurement of the lattice parameter of a silicon crystal’. *New Journal of Physics* 11 (2009) (cit. on p. 24).

[82]Y. Azuma, P. Barat, G. Bartl, H. Bettin, M. Borys, I. Busch, L. Cibik, G. D’Agostino, K. Fujii, H. Fujimoto, A. Hioki, M. Krumrey, U. Kuetgens, N. Kuramoto, G. Mana, E. Massa, R. Meeß, S. Mizushima, T. Narukawa, A. Nicolaus, A. Pramann, S. A. Rabb, O. Rienitz, C. Sasso, M. Stock, R. D. Vocke, A. Waseda, S. Wundrack, and S. Zakel. ‘Improved measurement results for the Avogadro constant using a 28 Si-enriched crystal’. *Metrologia* 52 (2015) (cit. on p. 24).

[83]P. Lautenschlager, P. B. Allen, and M. Cardona. ‘Temperature dependence of band gaps in Si and Ge’. *Physical Review B* 31 (1985) (cit. on p. 25).

[84]Y. Varshni. ‘Temperature dependence of the energy gap in semiconductors’. *Physica* 34 (1967) (cit. on p. 25).

[85]J. D. Gelorme, R. J. Cox, and S. A. R. Gutierrez. *Photoresist composition and printed circuit boards and packages made therewith*. 1989 (cit. on p. 28).

[86]J. Ou, T. Glawdel, C. L. Ren, and J. Pawliszyn. ‘Fabrication of a hybrid PDMS/SU-8/quartz microfluidic chip for enhancing UV absorption whole-channel imaging detection sensitivity and application for isoelectric focusing of proteins’. *Lab Chip* 9 (2009) (cit. on p. 28).

[87]Microchem. *http://www.microchem.com/Prod-SU8.htm*. 2017 (cit. on p. 29).

[88] S. K. Sundaram and E. Mazur. 'Inducing and probing non-thermal transitions in semiconductors using femtosecond laser pulses'. *Nature Materials* 1 (2002) (cit. on p. 36).

[89] Q. Lin, O. J. Painter, and G. P. Agrawal. 'Nonlinear optical phenomena in silicon waveguides: modeling and applications.' *Optics express* 15 (2007) (cit. on p. 37).

[90] A. D. Bristow, N. Rotenberg, and H. M. van Driel. 'Two-photon absorption and Kerr coefficients of silicon for 850–2200 nm'. *Applied Physics Letters* 90 (2007) (cit. on p. 38).

[91] H. K. Tsang, C. S. Wong, T. K. Liang, I. E. Day, S. W. Roberts, A. Harpin, J. Drake, and M. Asghari. 'Optical dispersion, two-photon absorption and self-phase modulation in silicon waveguides at 1.5 μm wavelength'. *Applied Physics Letters* 80 (2002) (cit. on pp. 38, 39).

[92] E. G. Gamaly, S. Juodkazis, H. Misawa, B. Luther-Davies, A. V. Rode, L. Hallo, P. Nicolai, and V. T. Tikhonchuk. 'Formation of nano-voids in transparent dielectrics by femtosecond lasers'. *Current Applied Physics* 8 (2008) (cit. on p. 38).

[93] Y. Shimotsuma, K. Hirao, J. Qiu, and K. Miura. 'Nanofabrication in transparent materials with a femtosecond pulse laser'. *Journal of Non-Crystalline Solids* 352 (2006) (cit. on p. 39).

[94] H. K. Tsang and Y. Liu. 'Nonlinear optical properties of silicon waveguides'. *Semiconductor Science and Technology* 23 (2008) (cit. on p. 39).

[95] M. Dinu, F. Quochi, and H. Garcia. 'Third-order nonlinearities in silicon at telecom wavelengths'. *Applied Physics Letters* 82 (2003) (cit. on p. 40).

[96] V. Parsi Sreenivas, M. Bülters, M. Schröder, and R. Bergmann. 'Three dimensional fabrication of optical waveguiding elements for on-chip integration'. *Proceedings of SPIE - The International Society for Optical Engineering*. Vol. 9130. 2014 (cit. on pp. 49, 101).

[97] A. Belea. 'The optical transfer matrix for plane diffraction gratings in Littrow mounting'. *Journal of Optics* 23 (1992) (cit. on p. 63).

[98] J. W. Goodman, A. R. Dias, and L. M. Woody. 'Fully parallel, high-speed incoherent optical method for performing discrete Fourier transforms'. *Optics Letters* 2 (1978) (cit. on pp. 87, 88).

[99] D. E. Tamir, N. T. Shaked, P. J. Wilson, and S. Dolev. 'High-speed and low-power electro-optical DSP coprocessor'. *Journal of the Optical Society of America A* 26 (2009) (cit. on p. 87).

[100] H. Levy and T. McGill. 'A feedforward artificial neural network based on quantum effect vector-matrix multipliers'. *IEEE Transactions on Neural Networks* 4 (1993) (cit. on p. 88).

[101] L. Wu, Y. Huang, Y. Zhang, H. Yang, C. Yang, and G. Cui. 'Performance of an embedded optical vector matrix multiplication processor architecture'. *IET Optoelectronics* 4 (2010) (cit. on p. 88).

[102] A. Chauhan. *Optical Vector Matrix Multiplier for Large Scale Parallel On-chip Computing*. 2014 (cit. on p. 95).

[103] J. W. Goodman. *Introduction to Fourier Optics*. The McGraw-Hill, 2004 (cit. on p. 96).

[104] E. N. Kamau, C. Falldorf, and R. B. Bergmann. 'A new approach to dynamic wave field synthesis using computer generated volume holograms'. *12th Workshop on Information Optics (WIO)*. IEEE, 2013 (cit. on p. 96).

[105] T. D. Gerke and R. Piestun. 'Aperiodic volume optics'. *Nature Photonics* 4 (2010) (cit. on p. 96).

[106] T. Hongo, K. Sugioka, H. Niino, Y. Cheng, M. Masuda, I. Miyamoto, H. Takai, and K. Midorikawa. 'Investigation of photoreaction mechanism of photosensitive glass by femtosecond laser'. *Journal of Applied Physics* 97 (2005) (cit. on p. 97).

[107] E. Kamau, V. Parsi Sreenivas, M. Bülters, C. Falldorf, and R. Bergmann. 'Fabrication of multiplexed computer generated volume holograms in photosensitive glass'. *Frontiers in Optics, FiO 2014*. 2014 (cit. on pp. 97, 101).

[108] R. Bergmann, M. Bülters, and V. V. Parsi Sreenivas. *Process and device for producing at least one photonic component*. 2015 (cit. on p. 99).

[109] M. Bülters, V. V. Parsi Sreenivas, A. Braun, U. Teubner, and R. B. Bergmann. 'Subsurface modification of crystalline silicon via ultra-short laser pulses for three dimensional separation'. *Proceedings of the 4th International Conference on Nanomanufacturing (nanoMan2014)*. 2014 (cit. on p. 100).

[110] J. Birkenstock, V. V. Parsi Sreenivas, R. B. Bergmann, and R. X. Fischer. 'Light diffraction experiments with micron-sized models of 3D-crystals'. *23rd Annual DKG Meeting* (2015) (cit. on p. 101).

[111] V. V. Parsi Sreenivas, M. Bülters, G. Dumstorff, A. Chauhan, A. Garcia-Ortiz, and R. B. Bergmann. 'Optical Vector Matrix Multiplier for On-Chip Computation'. *European Optical Society Annual Meeting, Berlin*. 2014 (cit. on p. 101).

List of Figures

1.1 Schematic of a laser oscillator . . . 2
1.2 Absorption, Spontaneous and Stimulated Emission . . . 3
1.3 Energy level structure of the trivalent erbium ion. . . . 8
1.4 Single and Two Photon Absorption Mechanism . . . 12
1.5 Stealth dicing concept . . . 15
1.6 GlassPack - An integrated photonic package . . . 17
1.7 IBM optoelectronic chip . . . 18

2.1 Silicon unit cell . . . 23
2.2 Silicon band diagram . . . 26
2.3 Chemical Structure of Polycarbonate . . . 27
2.4 SU-8 Monomer . . . 28
2.5 Work flow of SU-8 process . . . 29
2.6 Comparison between positive and negative photoresists . . . 31
2.7 Timescale of physical processes in ultrafast interactions . . . 36

3.1 Working principle of LeNA system . . . 43
3.2 Focussing objectives for LeNA. . . . 44
3.3 Photonic Professional from Nanoscribe . . . 47
3.4 Schematic of two photon polymerisation . . . 48
3.5 MONA: Modular Optical Nano Analyser . . . 49
3.6 MONA: Modular Optical Nano Analyser Setup . . . 52
3.7 FIB and SEM arrangement . . . 53
3.8 Müller Optronic Microscope . . . 55

4.1 Experimental set-up . . . 58
4.2 Visible and infrared images . . . 59
4.3 Diffraction tests with infrared laser . . . 60
4.4 Plot of the diffraction peak intensity . . . 61
4.5 Variation of pulse energy on subsurface modification . . . 63
4.6 SEM images of subsurface modifications . . . 65
4.7 A SEM image of a cross section of silicon wafer . . . 66
4.8 A FIB milled SEM image of a top surface of 100 silicon . . . 66
4.9 SEM images of etched silicon surfaces . . . 68
4.10 Waveguide in the bulk of silicon . . . 70
4.11 Simulation results of a-Si waveguide . . . 72
4.12 Simulation results of a photonic crystal waveguide . . . 73
4.13 Simulation results of a c-Si waveguide cladded by voids . . . 74
4.14 3D POW with taper and lens . . . 76
4.15 Stress distribution in 3DPOW . . . 78

4.16 Planar Grating Coupler . . . 79
4.17 Interferometer Grating Coupler . . . 81
4.18 Ring Resonator . . . 82
4.19 3D Polymer Optical Waveguides . . . 83
4.20 3D Polymer Optical Waveguides under MONA . . . 84

5.1 Schematic of the Optical Vector Matrix Multiplier . . . 88
5.2 Schematic of the proposed Optical Vector Matrix Multiplier . . . 89
5.3 Split view and the working of modified LCD . . . 91
5.4 Waveguides in transmissive and receptive modes . . . 92
5.5 Different designs of the waveguides . . . 93
5.6 Intensity distribution over different waveguides . . . 94
5.7 Intensity distribution over PSB waveguides . . . 94
5.8 Complete OVMM schematic . . . 96
5.9 CGVH in Foturan Glass . . . 97

6.1 3D Optical Circuit Board . . . 103
6.2 Schematic examples of optical building blocks . . . 103
6.3 Optical waveguides on electronic chips . . . 104

A.1 Seed box for the laser system in LeNA . . . 108
A.2 Amplifier box for the laser system in LeNA . . . 109
A.3 Joystick, Dual Button, and Piezo Speaker Bricklets from Tinkerforge . . . 111
A.4 User Interface for Laser control . . . 112
A.5 Trigger Options on the Laser UI . . . 113
A.6 LeNA plugin loaded in Fringe Processor . . . 114
A.7 LeNA Control Panel . . . 115
A.8 Script generation dialog - LeNA UI . . . 117

C.1 Electric and optical specifications of the 1101W series LED . . . 125
C.2 Electric and optical specifications of the BPW34 photodiode . . . 126
C.3 An Arduino Uno Board . . . 127

List of Tables

1.1 Comparison of different laser types 9

2.1 Material parameters of silicon 22
2.2 Material parameters of polycarbonate 28
2.3 Material parameters of SU-8 29
2.4 Dielectric properties of a medium 33
2.5 Comparison of physical parameters between polymers and silicon 39

3.1 Comparison of Laser Systems 42
3.2 Specifications of the focussing objectives in the LeNA system 44
3.3 Specification Table for XY Stages - LeNA 45
3.4 Specification Table for Z Stage - LeNA 45

4.1 Analysis of diffraction peaks from subsurface modifications 62
4.2 Dimensions of grating coupler 77

5.1 Specifications of ST7735 TFT-LCD Module 90

A.1 Specification Table for Raydiance M 50 110

B.1 Default Values for Stage Velocities and Accelerations 122

C.1 Specifications of Arduino Uno 127

Glossary of Terms

2PA	Two Photon Absorption.
2PP	Two Photon Polymerisation.
AOM	Acousto Opto Modulator.
ASB	Arbitrary Sand Blasted Waveguide.
AWG	Arrayed Waveguide Gratings.
BCC	Body Centred Cubic.
BIAS	Bremer Institut für angewandte Strahltechnik GmbH.
BSE	Back Scattered Electrons.
CCD	Charged Coupled Device.
CGVH	Computer Generated Volume Holograms.
CMOS	Complementary Metal-Oxide Semiconductor.
CW	Continuous Wave (Laser).
DFT	Discrete Fourier transforms.
DIC	Differential Interference Contrast.
DLW	Direct Laser Writing.
EsB	Energy selective Backscattered.
FCC	Face Centred Cubic.
FIB	Focussed Ion Beam.
FPS	Frames per Second.
fs	femtosecond.
GIS	Gas Injection System.
GWL	General Writing Language.
HRW	Hand Roughed Waveguide.
IR	Infrared.
KOH	Potassium Hydroxide.
LCD	Liquid Crystal Display.
LED	Light Emitting Diode.
LeNA	Laser enabled Nano-structuring Apparatus.
LMIS	Liquid Metal Ion Source.
MFD	Mode Field Diameter.
MONA	Modular Optic Nano Analyser.
MUX/DEMUX	Multiplexing/ Demultiplexing.
NA	Numerical Aperture.

OCB	Optical Circuit Board.
OpAmp	Operational Amplifier.
OVMM	Optical Vector Matrix Multiplier.
PD	Photo detector.
PI	Physik Instrumente.
PMMA	Poly (methyl) Methacrylate.
POW	Polymer Optical Waveguide(s).
PSB	Patterned Waveguide.
RAM	Random Access Memory.
RGB	Red-Green-Blue.
SE	Secondary Electrons.
SEM	Scanning Electron Microscope.
SLM	Spatial Light Modulator.
SPI	Serial Peripheral Interface.
STEM	Scanning Transmission Electron Microscopy.
STL	STereoLithography.
TEC	Thermo-Electric Cooler.
TFT	Thin Film Transistor.
TIA	Trans Impedance Amplifier.
TTL	Transistor-Transistor Logic.
UI	User Interface.
USB	Universal Serial Bus.
VCSEL	Vertical Cavity Side Emitting Laser.
yal	Yet Another Language.

Curriculum Vitae

Education and Work Experience

2013 - 2015	Researcher - PhD Student, University of Bremen, Germany
2009 - 2013	Researcher, BIAS GmbH, Bremen, Germany
2007 - 2009	Master of Science in Physics, University of Stuttgart, Germany
2004 - 2007	Bachelor of Science in Physics, Mathematics, and Computer Science, St. Joseph's College, Bangalore University, India.

Publications

Publications with peer-review

[1] Vijay V. Parsi Sreenivas, Mike Bülters, and Ralf B. Bergmann. Microsized subsurface modification of mono-crystalline silicon via non-linear absorption J. Europ. Opt. Soc. Rap. Public 7, 12035-1-5, 2012.

Conferences with peer-reviewed publications

[1] Edwin N. Kamau, Vijay V. Parsi Sreenivas, Mike Bülters, Claas Falldorf, and Ralf B. Bergmann. Fabrication of Multiplexed Computer Generated Volume Holograms in Photosensitive Glass. In Proceedings of OSA, Frontiers in Optics, Paper No. FTh4G2, Tucson, Arizona, Oct. 2014.

Patents

[1] Ralf B. Bergmann, Mike Bülters, and Vijay V. Parsi Sreenivas. Verfahren und Vorrichtung zum Herstellen von mindestens einem photonischen Bauelement. DE 10 2011 113 824 A1, Issued Dec. 2014.

[2] Ralf B. Bergmann, Mike Bülters, and Vijay V. Parsi Sreenivas. Process and device for producing at least one photonic component. US 8,937,024B2, Issued Jan. 2015.

Posters

[1] Johannes Birkenstock, Vijay V. Parsi Sreenivas, Ralf B. Bergmann and Reinhard X. Fischer. Light diffraction experiments with micron-sized models of 3D-crystals. Poster, 23rd Annual Conference of the German Crystallographic Society, Göttingen, 16.03.2015.

[2] Wolfgang Büter, Alberto García-Ortiz, Adnan Ali, S. Mahmood, S. Arefin, Vijay V. Parsi Sreenivas and Ralf B. Bergmann. A Framework for the Emulation and Prototyping of Nano-Photonic Optical Accelerators. Poster, Design, Automation und Test in Europe - DATE Conference, Grenoble, France, 9-13.03.2015.

Conferences

[1] Wolfgang Büter, Alberto García-Ortiz, Adnan Ali, S. Mahmood, S. Arefin, Vijay V. Parsi Sreenivas and Ralf B. Bergmann. A rapid prototyping framework for nano-photonic accelerators. Proceedings of the 25th International Conference on Field Programmable Logic and Applications (FPL 2015) doi:10.1109/FPL.2015.7294004

[2] Mike Bülters, Edwin N. Kamau, Carmen Sanchez Alvarez, Vijay V. Parsi Sreenivas, Claas Falldorf, and Ralf B. Bergmann. Three dimensional modification of the refractive index in photosensitive Foturan glass. In Proceedings of DGaO - 115. Jahrestagung der DGaO, Karlsruhe on 11.06.2014, 2014.

[3] Vijay V. Parsi Sreenivas, Mike Bülters, Gerrit Dumstorff, Aditya Chauhan, A. Garcia-Ortiz, and Ralf B. Bergmann. Optical Vector Matrix Multiplier for ON-Chip Computation. European Optical Society Annual Meeting (EOSAM 2014) Berlin (CD-ROM).

[4] Vijay V. Parsi Sreenivas, Mike Bülters, Katharina Morosov, and Ralf B. Bergmann. Optical waveguides via laser micro machining. In Proceedings of the 4th nanoMan in Bremen on 08.07.2014, volume A3-4, 2014.

[5] Mike Bülters, Vijay V. Parsi Sreenivas, Andreas Braun, U. Teubner, and Ralf B. Bergmann. Subsurface modification of crystalline silicon via ultra-short laser pulses for three dimensional separation. In Proceedings of the 4th nanoMan in Bremen on 10.07.2014, 2014.

[6] Vijay V. Parsi Sreenivas, Martin Schröder, Mike Bülters, and Ralf B. Bergmann. Three dimensional fabrication of optical waveguiding elements for on-chip integration. In Proc. SPIE Micro-Optics 2014, Brussels, volume 9130, editors, H Thienpont, J Mohr, H Zappe, and H Nakajima, 2014.

[7] Vijay V. Parsi Sreenivas, Mike Bülters, and Ralf B. Bergmann. Subsurface modification in mono- crystalline silicon by multiphoton processes - analytical model and first results. In EOS Annual Meeting, Aberdeen, ISBN 978-3-9815022-4-4, 2012.

[8] Vijay V. Parsi Sreenivas, Mike Bülters, Christoph von Kopylow, and Ralf B. Bergmann. Nanosized subsurface modification of mono-crystalline silicon via non-linear absorption. In Proceedings 1st EOS Topical Meeting on Micro- and Nano-Optoelectronic systems, Bremen, ISBN 978-3-00-033711-6, 2011.

[9] Martin Schröder, Vijay V. Parsi Sreenivas, Christoph von Kopylow, and Ralf B. Bergmann. Novel concept for three-dimensional polymer waveguides. In Proceedings 1st EOS Topical Meeting on Micro- and Nano-Optoelectronic systems, Bremen, ISBN 978-3-00-033711-6, 2011.

Talks

[1] Ralf B. Bergmann, Vijay V. Parsi Sreenivas, Mike Bülters, Alberto Garcia Ortiz, J. Gutowski, and W Lang. Nanophotonics in Three Dimensions: Heading from Micro-electronics towards Optical Computing. In 2nd Internat. Conf. on System-Integrated Intelligence SysInt2014, Bremen, 2014.

[2] Edwin N. Kamau, Mike Bülters, Carmen Sanchez Alvarez, Vijay V. Parsi Sreenivas, Claas Falldorf, and Ralf B.Bergmann. Fabrication of 3d DOEs in photosensitive Foturan Glass. 4th nanoMan in Bremen, 2014.

[3] Edwin N. Kamau, Claas Falldorf, Vijay V. Parsi Sreenivas, Mike Bülters, and Ralf B.Bergmann. Fabrication of Multiplexed Computer Generated Volume Holograms in Photosensitive Glass, Frontiers in Optics/Laser Science, Tucson AZ, 2014.

[4] Mike Bülters, Edwin N. Kamau, Vijay V. Parsi Sreenivas, Claas Falldorf, and Ralf B.Bergmann. 3D DOEs in photosensitivem Foturan Glas. 115. Jahrestagung der DGaO, Karlsruhe, 2014.